# Interphase Formation at the Interface between Solid Electrolytes and Lithium Metal Anodes in Solid-State Batteries

Dem Fachbereich Biologie und Chemie
der Justus-Liebig-Universität Gießen
vorgelegte Dissertation zur Erlangung
des akademischen Grades
Doktor der Naturwissenschaften
− Dr. rer. nat. −

**Luise Mathilda Riegger**

November 2023

| | |
|---|---|
| Dekan / Dean | Prof. Dr. Thomas Wilke |
| 1. Gutachter / 1st Reviewer | Prof. Dr. Jürgen Janek<br>(Justus-Liebig-Universität Gießen) |
| 2. Gutachter / 2nd Reviewer | Privatdozent Dr. Matthias Elm<br>(Justus-Liebig-Universität Gießen) |
| Eingereicht / Submitted | 11.2023 |
| Disputation / Disputation | 21.12.2023 |

## Eidesstattliche Erklärung

Die vorliegende Arbeit wurde im Zeitraum vom 01.02.2019 bis 10.11.2023 am Physikalisch-Chemischen Institut der Justus-Liebig-Universität Gießen unter Betreuung von Prof. Dr. Jürgen Janek angefertigt.

Ich erkläre: Ich habe die vorgelegte Dissertation selbstständig und ohne unerlaubte fremde Hilfe und nur mit den Hilfen angefertigt, die ich in der Dissertation angegeben habe. Alle Textstellen, die wörtlich oder sinngemäß aus veröffentlichten Schriften entnommen sind, und alle Angaben, die auf mündlichen Auskünften beruhen, sind als solche kenntlich gemacht. Ich stimme einer evtl. Überprüfung meiner Dissertation durch eine Antiplagiat-Software zu. Bei den von mir durchgeführten und in der Dissertation erwähnten Untersuchungen habe ich die Grundsätze guter wissenschaftlicher Praxis, wie sie in der „Satzung der Justus-Liebig-Universität Gießen zur Sicherung guter wissenschaftlicher Praxis“ niedergelegt sind, eingehalten.

Gießen, 10.11.2023

Luise Mathilda Riegger

## Abstract

The growing demand for energy storage systems, driven by the need for the “energy transition”, highlights the importance of efficient energy storage. Conventional lithium-ion batteries with liquid electrolytes are approaching their theoretical physicochemical limits and are subject to safety concerns due to risk of leakage and high flammability. To overcome these limitations, solid-state batteries with solid electrolytes are explored as an alternative that offer greater safety and a wider operation temperature range. When combined with a lithium metal anode, solid-state batteries can achieve the required energy and power densities.

However, the reactivity of lithium metal presents safety challenges such as side reactions and dendrite formation. Most solid electrolytes decompose upon contact with lithium, forming different interphases depending on the electrolyte composition. Understanding the interphase formation at the lithium|solid electrolyte interface is crucial for developing protective measures. In addition, studying the kinetic growth of interphase formation helps in estimating the lifetime of the battery.

This dissertation focuses on the characterization of interphase formation between solid electrolytes and lithium metal. The interphase formation of recently developed solid electrolytes with high ionic conductivities, which are required for industrial applications, is investigated. No prior information on the reduction stability has been available for these electrolytes. Techniques such as *in situ* X-ray photoelectron spectroscopy and impedance spectroscopy are used to investigate the chemical stability towards lithium, the interphase evolution, and the cell resistance.

In Publication 1, the reduction stability of halide solid electrolytes $Li_3MCl_6$ (M = In, Y) is investigated. They are found to be unstable toward lithium and form the corresponding metal upon contact. When electronically conducting decomposition products are formed during reduction, the interphase grows continuously, which is detrimental for cell performance. In order to use both the halide solid electrolytes and lithium metal, the use of $Li_6PS_5Cl$ as a protective layer between both is proposed. The interfacial resistance of $Li_3InCl_6|Li_6PS_5Cl$ is negligible and does not affect the performance of the cell, making it suitable for industrial applications.

The thiophosphate solid electrolyte $Li_7SiPS_8$ studied in Publication 2 also decomposes by reduction. Although no elemental silicon or an Li-Si alloy is formed, the interphase grows continuously, showing that electronically conducting pathways are nevertheless formed during decomposition. Unfortunately, the component causing the electronic conductivity could not be determined. However, the continuously forming, highly resistive interphase shows that the solid electrolyte is unsuitable for application with direct contact to a lithium metal anode.

The influence of the lithium metal surface on the growth kinetics of the $Li|Li_6PS_5Cl$ interphase evolution is investigated in Publication 3 using impedance spectroscopy. It is found that the passivation layer present on commercial lithium foils negatively impacts the overall resistance of the cell and the growth kinetics of the interphase. Cells utilizing passivated lithium exhibit non-self-limited interphase growth, in contrast to cells built with freshly prepared lithium for which interphase formation ceases rapidly within 9 hours after contact. Based on this result, reservoir-free cells are proposed to avoid the drawbacks caused by the passivation layer of commercial lithium foils.

Overall, this dissertation extends the knowledge of interfacial stability in different solid electrolyte classes. The findings are relevant for the use of lithium metal as anode material and the development of protective strategies for solid electrolytes unstable against lithium. In addition, insights into the influence of the processing history of cell components on cell performance are obtained, facilitating the commercialization of SSBs.

## Zusammenfassung

Die durch die Energiewende wachsende Nachfrage nach Energiespeichersystemen verdeutlicht die Bedeutung effizienter Energiespeicherung. Herkömmliche Lithium-Ionen-Batterien mit flüssigen Elektrolyten stoßen an ihren theoretischen physikochemischen Grenzen und sind aufgrund des Leckagerisikos und der hohen Entflammbarkeit mit Sicherheitsbedenken behaftet. Um diese Einschränkungen zu überwinden, werden Alternativen wie Festkörperbatterien mit festen Elektrolyten erforscht, die mehr Sicherheit und zusätzlich einen größeren Betriebstemperaturbereich bieten. In Kombination mit einer Lithiummetallanode können Festkörperbatterien die erforderlichen Energie- und Leistungsdichten erreichen.

Die Reaktivität des Lithiummetalls bringt jedoch Sicherheitsprobleme wie Nebenreaktionen und Dendritenbildung mit sich. Die meisten Festelektrolyte zersetzen sich bei Kontakt mit Lithium, wobei sich je nach Elektrolytzusammensetzung verschiedene Zwischenphasen bilden. Das Verständnis der Interphasenbildung an der Lithium|Festelektrolyt Grenzfläche ist entscheidend für die Entwicklung von Schutzkonzepten. Darüber hinaus hilft die Untersuchung des kinetischen Wachstums der Zwischenphasenbildung bei der Abschätzung der Lebensdauer der Batterie.

Diese Dissertation befasst sich mit der Charakterisierung der Zwischenphasenbildung zwischen Festelektrolyten und Lithiummetall. Zunächst wird die Zwischenphasenbildung von kürzlich entwickelten Festelektrolyten mit hohen Ionenleitfähigkeiten untersucht. Für diese Elektrolyte waren bisher keine Informationen über die Reduktionsstabilität verfügbar. Durch den Einsatz von Methoden wie *in situ* Röntgen-Photoelektronen Spektroskopie und Impedanzspektroskopie werden die chemische Stabilität gegenüber Lithium, die Zwischenphasenbildung und der Zellwiderstand untersucht.

In Publikation 1 wird die Reduktionsstabilität von Halogenid-Festelektrolyten $Li_3MCl_6$ (M = In, Y) untersucht. Sie erweisen sich als instabil gegenüber Lithium und bilden bei Kontakt das entsprechende Metall. Um die Zersetzung zu verhindern, wird die Verwendung von $Li_6PS_5Cl$ als Schutzschicht vorgeschlagen. Der Grenzflächenwiderstand von $Li_3InCl_6$|$Li_6PS_5Cl$ ist vernachlässigbar und beeinträchtigt die Leistung der Zelle nicht, was sie für industrielle Anwendungen geeignet macht.

Der in Publikation 2 untersuchte Thiophosphat-Festelektrolyt $Li_7SiPS_8$ zersetzt sich ebenfalls durch Reduktion. Obwohl sich kein $Si^0$ oder eine Li-Si-Legierung bildet, wächst die Zwischenphase kontinuierlich, was zeigt, dass sich bei der Zersetzung elektronisch leitende Pfade bilden. Leider konnte die Komponente, die die elektronische Leitfähigkeit hervorruft, nicht bestimmt werden. Dennoch ist der Festelektrolyt für eine Anwendung mit direktem Kontakt zu einer Lithiummetallanode ungeeignet.

Der Einfluss der Lithium-Metalloberfläche auf die Wachstumskinetik der Li|$Li_6PS_5Cl$ Zwischenphasenentwicklung wird in Publikation 3 mittels Impedanzspektroskopie untersucht. Die Passivierungsschicht auf handelsüblichen Lithiumfolien beeinflusst den Gesamtwiderstand der Zelle und die Wachstumskinetik der Interphase negativ. Zellen, die passiviertes Lithium verwenden, zeigen ein nicht selbstbegrenztes Zwischenphasenwachstum. Im Gegensatz dazu, stoppt die Zwischenphasenbildung innerhalb von 9 Stunden nach Kontakt zwischen Festelektrolyt und frisch hergestelltem Lithium. Um die Nachteile zu vermeiden, werden Reservoir-freie Zellen empfohlen, bei denen Lithiummetall an der Anode abgeschieden wird und nicht passiviert ist.

Insgesamt erweitert diese Dissertation das Wissen über die Grenzflächenstabilität verschiedener Festelektrolytklassen. Die Erkenntnisse sind für den Einsatz von Lithiummetall als Anodenmaterial und die Entwicklung von Schutzstrategien für mit Lithium instabile Festelektrolyte von großer Bedeutung. Darüber hinaus werden Erkenntnisse über den Einfluss der Verarbeitungsgeschichte von Zellkomponenten auf die Zellleistung gewonnen, was die Kommerzialisierung von Feststoffbatterien erleichtert.

## List of Abbreviations

| | |
|---|---|
| AES | Auger electron spectroscopy |
| AFM | Atomic force microscopy |
| BE | Binding energy |
| CCD | Critical current density |
| CE | Counter electrode |
| CPE | Constant phase element |
| CT | X-ray computed tomography |
| DFT | Density function theory |
| EDX | Energy dispersive X-ray analysis |
| ESW | Electrochemical stability window |
| FIB | Focused ion beam |
| HAXPES | Hard X-ray photoelectron spectroscopy |
| HOMO | Highest occupied molecular orbital |
| KE | Kinetic energy |
| LATP | $Li_{1.5}Al_{0.5}Ti_{1.5}(PO_4)_3$ |
| LE | Liquid electrolyte |
| LGPS | $Li_{10}GeP_2S_{12}$ |
| Li\|LE | Lithium metal \| liquid electrolyte |
| Li\|SE | Lithium metal \| solid electrolyte |
| LIB | Lithium-ion battery |
| LIC | $Li_3InCl_6$ |
| LiPON | $Li_{3.6}PO_{3.4}N_{0.6}$, lithium phosphorus oxynitride |
| LiSiPS | $Li_7SiPS_8$ |
| LLZO | $Li_{6.25}Al_{0.25}La_3Zr_2O_{12}$ |
| LMA | Lithium metal anode |
| LMB | Lithium metal battery |
| LMC | $Li_3MCl_6$ (M = In, Y) |
| LPSCl | $Li_6PS_5Cl$, chloride-argyrodite |
| LPSX | $Li_6PS_5X$ (X = Cl, Br, I), argyrodite |

| | |
|---|---|
| LUMO | Lowest unoccupied molecular orbital |
| LYC | $Li_3YCl_6$ |
| MAS | Magnetic angle spinning |
| MCI | Mixed ionic-electronic conducting interphase |
| NMR | Nuclear magnetic resonance |
| RE | Reference electrode |
| SE | Solid electrolyte |
| SEI | Solid electrolyte interphase |
| SEM | Scanning electron microscopy |
| SOXPES | Soft X-ray photoelectron spectroscopy |
| SSB | Solid-state battery |
| TEM | Transmission electron microscopy |
| ToF-SIMS | Time-of-flight secondary ion mass spectrometry |
| UHV | Ultra-high vacuum |
| UV | ultraviolet |
| VE | Virtual electrode |
| WE | Working electrode |
| XP | X-ray photoelectron |
| XPS | X-ray photoelectron spectroscopy |
| XRD | X-ray diffraction analysis |

## Table of Contents

# 1 Introduction

Lithium-ion batteries (LIBs) have revolutionized energy storage and are widely used in various applications.[1,2] In a typical LIB design, the anode and cathode electrodes are separated by an electronically insulating separator, through which a liquid electrolyte (LE) permeates to allow migration of $Li^+$ ions. One significant area of research in LIBs is the utilization of lithium metal as the anode material due to its high theoretical energy density.[3] In the 1970s and 80s, lithium metal batteries (LMB) capable of recharging were commercially available, demonstrating the potential of lithium metal anodes (LMAs). However, their use has been limited due to challenges associated with their morphological instability and high reduction potential, which pose a significant safety risk due to thermal runaway and explosion. [3,4]

When the LE typically used in LIB comes into contact with the lithium metal surface, it decomposes and forms a thin decomposition layer.[2,5,6] Peled proposed calling this layer the "solid electrolyte interphase" (SEI) as it conducts lithium ions but is electronically insulating, thus, resembling a solid electrolyte.[6] Because the SEI is electronically insulating, the growth is self-limited, resulting in a low initial SEI thickness. It acts as a protective layer on the lithium metal, preventing further decomposition and ensuring battery stability and safety.[2,6,7]

As the SEI composition and structure depend on the solvents and additives used, its properties can be tailored.[8] Usually, the SEI consists of inorganic products such as LiF, $Li_2O$ or $Li_2CO_3$, and various organic compounds. The inorganic products are stable against further reduction und thus stabilize the SEI|LE interface.[5,7] Despite decades of intensive research, the analysis of the SEI remains challenging due to its low thickness and complex composition. As a result, the SEI structure is still not fully understood, but several models have been developed to describe possible structures. The mosaic model assumes that the components are heterogeneously distributed, the multitype model assumes an outer $Li_2O$ layer and an inner amorphous layer, while the monolithic model assumes a homogenous amorphous layer.[5,7]

While the exact SEI microstructure is unknown, its spatial distribution has a strong influence on the mechanical properties, the morphology of the plated lithium and the amount of lithium that becomes inactive due to contact loss. A more homogeneous SEI generally leads to a better cycling performance.[7] However, as lithium is plated and stripped, the electrode volume changes, leading to cracks in the SEI and exposure of blank lithium to the electrolyte, which in turn increases electrochemical SEI formation.[2,8] This process increases the loss of lithium and liquid electrolyte and risks electrolyte depletion.[2,7–9] Another major concern is the formation of dendrites and detached lithium filaments, which reduce Coulomb efficiency and increase the risk of short circuits which would compromise cell safety as fires can occur.[3,4,8]

To mitigate these challenges and improve battery performance beyond the physico-chemical limits of LIBs, alternative battery concepts are being explored.[2] One promising concept are solid-state batteries (SSBs).[10] SSBs, which employ inorganic solid electrolytes (SEs) as the separator, offer better safety because their flammability is lower compared to LIBs and they cannot leak in case of a damaged cell casing.[11] In addition, their improved mechanical stability should simplify cell assembly and allow bipolar stacking, which would increase energy densities.[10,11] Furthermore, the mechanical stability of solid electrolytes was initially thought to increase the stability of an LMA during cycling.[12,13] However, intensive research during the last years has shown that SEs can yet not suppress the morphological changes of cycled lithium, so contact loss, dendrite formation, and short circuits in SSBs are still challenging.[14–17]

Like LEs, most SEs decompose upon contact with lithium metal to form an interphase consisting of reduced decomposition products.[10,18–22] Nevertheless, the use of LMAs in inorganic SSBs becomes feasible as the degree of electrolyte reduction is reduced and the insolubility of the interphase in an all-solid system should prevent continuous side reactions during cycling. Unfortunately, not all interphases are solely ion conductors, but some SEs form mixed conducting interphases (MCIs) upon reduction that continuously grow until depletion of one of the materials.[23,24] Therefore, MCI formation is detrimental to cell performance and it is imperative to determine what type of interphase forms for the electrolyte class in general and for the Li|SE interface of the most promising SEs in particular.[19,21,22]

At the beginning of this doctoral work, there were few studies on the temporal interphase evolution of solid electrolytes in contact with lithium metal. This is due to the difficulty in studying the dynamic nature of these buried interfaces, which necessitates *in situ* or *operando* approaches to better correlate the electrochemistry with the particular composition or structure morphology.[12] Hartmann et al. invented an *in situ* deposition method to study the chemical degradation of SEs.[18] This was then further developed by Wenzel et al. to study the chemical stability of different SEs, and three different types of interface and interphases were classified.[23]

The interphase evolution in SSBs represents a critical aspect of research to enable the development of stable and high-performance solid-state batteries.[12] Therefore, this thesis focuses on further understanding the interactions between lithium metal and solid electrolytes to enable the development of stable interfaces and interphases as well as artificial protective layers. Both the MCI formation of newly developed SEs, and the SEI formation kinetics of LPSCl are studied in detail to elucidate the decomposition reactions.[21,22,25] The overall aim is to understand the processes involved in interphase formation to enable future rational development of protective anode concepts.

In the first publication of this thesis, entitled: "*Lithium-Metal Anode Instability of the Superionic Halide Solid Electrolytes and the Implications for Solid-State Batteries*", first experimental insights into the anodic stability of the then recently emerged halide SEs are provided (see chapter 3.1).[22] For this, the SEs $Li_3MCl_6$ (LMC, M= In, Y) are studied using *in situ* deposition of lithium and subsequent XPS measurements, as well as impedance spectroscopy of symmetric Li|LMC|Li cells. The XPS measurements reveal that the respective metal ($In^0$ or $Y^0$) is formed upon lithium deposition. Thus, a mixed conducting interphase (MCI) is formed because the metals provide a conduction pathway for the electrons. This is confirmed by the temporal impedance growth, revealing that both SEs are continuously decomposed, and no self-limited interphase is formed. Therefore, protective concepts such as interlayers are needed. An interlayer consisting of chloride argyrodite LPSCl is proposed and tested using impedance spectroscopy. This revealed that the interfacial resistance is negligible. As all halide SEs contain an $M^{3+}$ metal or semimetal, it is concluded that this electrolyte class is generally unstable against lithium. However, since these SEs are stable to oxidation and cathode active materials, they are well suited for applications in SSBs when an interlayer that protects against reduction is used.

In the second publication, entitled: "*Instability of the $Li_7SiPS_8$ Solid Electrolyte at the Lithium Metal Anode and Interphase Formation*", the MCI formation between the SE $Li_7SiPS_8$ and lithium metal is studied (see chapter 3.2).[21] The temporal impedance evolution of symmetric Li|$Li_7SiPS_8$|Li cells shows that the interphase resistance rapidly increases after contact of the materials, indicating the formation of an MCI. This was confirmed by additional cycling experiments. From similar experiments on $Li_{10}GeP_2S_{12}$ (LGPS) it is known that the metal(loid) becomes metallic when reduced by lithium.[19,24] However, chemical analysis revealed that the expected formation of elemental silicon

or Li-Si alloy does not occur. Therefore, the cause for the MCI formation remains unclear. Nonetheless, through this work it was revealed that an MCI can be formed even if no metal, metalloid or alloy is formed during decomposition.

In the third publication, entitled: "*Evolution of the Interphase between Argyrodite-based Solid Electrolytes and the Lithium Metal Anode – The Kinetics of Solid Electrolyte Interphase Growth*", the focus of this thesis shifts from investigating MCI formations of recently emerged SEs to the quantitative study of the SEI growth in Li|LPSCl|Li cells (see chapter 3.3).[25] While the Li|LPSCl interphase formation had been previously studied, discrepancies were found in the nature of growth kinetics.[20,26] To elucidate the reason for this, the influence of the LMA surface chemistry on the growth kinetics is explored in this publication using passivated and freshly prepared lithium foils. By varying the lithium surface, it is shown that this has a large influence on the growth mechanism: When commercial passivated lithium is used, an interphase forms which, unlike the interphase formation with freshly prepared lithium, does not stop growing throughout the duration of the experiment. Furthermore, depending on how much SE can penetrate the passivation layer, more direct contacts with lithium metal are created, which in turn increases the reaction rate. The results of this publication suggest that reservoir-free cells could be more suited for commercial applications as pure lithium is plated in these cells. Thus, no passivation layer would affect the internal resistances and cell performance.

Overall, the presented results expand the understanding of degradation processes at the interface between the lithium metal anode and SEs as well as the subsequent interphase formation. The studies on the metal or metalloid containing SEs provide more insights into the formation of mixed conductive interphases. Additionally, the study of the SEI formation reveals that the growth kinetics are influenced by the passivation layer of the lithium foil, concluding that the processing history of cell components needs to be considered when evaluating the overall cell performance.

# 2 Fundamentals

This chapter provides a brief overview of the current literature on the topics covered in this thesis. Particular attention is paid to the material characterization of interphases, especially *in situ* lithium deposition methods in combination with X-ray photoelectron spectroscopy.

## 2.1 Inorganic Solid Electrolytes for Solid-State batteries

As LIB performance approaches its physio-chemical limit, the demand for next-generation batteries becomes imperative.[10] In 2011, Kamaya et al. reported $Li_{10}GeP_2S_{12}$ (LGPS) as a solid electrolyte with an ionic conductivity of 12 $mS \cdot cm^{-1}$.[27] This discovery brought solid-state batteries into the spotlight, leading to intensified research on SEs in the past decade.[28] Various classes of SEs have been identified, including polymers, oxides, halides as well as thiophosphates.[10,29]

One notable advantage of inorganic SEs is their high lithium-transference number, enabling fast charging without polarization. Moreover, SEs facilitate bipolar stacking electrodes and effectively prevent electrode crosstalk, mitigating a common cause of long-term instability in LIB. However, high-capacity anodes, such as silicon anodes or lithium metal, are needed to obtain specific energies that can compete with LIBs. Unfortunately, most SEs are inherently unstable against the low electrochemical potentials of these materials and decompose by a reduction reaction upon contact.[10] Thus, safety measures are required to enable long-term stability. A brief overview over the SEs used in this thesis is given in the following segment.

### 2.1.1 Halide Solid Electrolytes

While halide SEs have been known since the 1930s, they only received worldwide attention through seminal work by Asano et al. in 2018.[30,31] Halide SEs with the composition $Li_3MX_6$ ($M^{3+}$, X = Cl, Br, I) generally exhibit high ionic conductivities,[30] especially after ball-milling synthesis.[32] Also, their electrochemical stability against oxidation is high,[33] reducing side reactions with cathode active materials.[30]

However, poor reduction stability has been predicted by theoretical work.[34] In Publication 1 of this thesis, experimental data on the reduction instability of halide SEs toward lithium metal is shown for the first time.[22] To avoid decomposition of the electrolyte, a bilayer structure with the argyrodite $Li_6PS_5Cl$ (LPSCl) is proposed. Here, initial experiments on the $Li_3InCl_6$|LPSCl interface show only a small interfacial resistance.[22] However, a more recent study on this interface reveals side reactions in the form of indium sulfide-like species between $Li_3InCl_6$ and LPSCl.[35] Another possibility to improve reduction stability is to partially substitute fluorine for the chlorine anions.[36]

### 2.1.2 $Li_7SiPS_8$

The $Li_7SiP_8$ (LiSiPS) electrolyte studied in Publication 2 of this thesis, was first synthesized by Harm et al. in 2019.[37] It is part of the LGPS-family, with germanium substituted by silicon as it is earth-abundant and cheaper. Its tetragonal phase has an ionic conductivity of 2 $mS \cdot cm^{-1}$, which is fast in absolute terms but low for this type of SE. The reason for this, is an amorphous side phase that hinders ion transport.[37] To minimize the influence of the side phase, Calaminus et al. synthesized a LiSiPS/argyrodite (LPSX, X=Cl, Br, I) hybrid.[38] The argyrodite formed *in situ* directs the growth of the tetragonal LiSiPS particles which increases their grain size. This reduces the influence

of the grain boundary resistance and the lithium transport is more bulk-dominated, leading to ionic conductivities of 7 $mS \cdot cm^{-1}$.[38]

LGPS is unstable against lithium metal.[19,24] It has also been suggested that this is true for LiSiPS,[39,40] but no experimental data on the stability vs lithium was available. Therefore, the stability of tetragonal LiSiPS toward lithium metal is investigated in Publication 2 of this thesis.[21] While both electrolytes are unstable against lithium metal and form a mixed conducting interphase, the decomposition mechanism differs from that of LGPS. In the case of LiSiPS, no elemental Si or Li-Si alloy is formed. [21] The exact decomposition mechanism could, however, not be clarified, so further work is needed.

### 2.1.3 Argyrodite

Another type of SE that exhibits high ionic conductivities above 1 $mS \cdot cm^{-1}$ are lithium argyrodites $Li_6PS_5X$, composed of Li, S, P and usually a halide ion $X^-$ ( X = Br, Cl, I).[10] In this materials class, the ionic conductivity is strongly influenced by the $S^{2-}/X^-$ site disorder.[41,42] It can be further increased by aliovalent substitution of the $P^{5+}$,[43,44] or by introducing additional halide anions.[45,46] With this optimization, ionic conductivities above 10 $mS \cdot cm^{-1}$ are possible.[10,28] In addition to the high conductivity, the good malleability at room temperature and the scalability of fabrication make argyrodites a suitable candidate for large-scale applications.[29,47]

Like other SEs, argyrodite is not electrochemically stable against lithium metal.[12,20] However, if the argyrodite does not contain a metal(-loid), a metastable solid electrolyte interphase forms.[20] While the growth kinetics have already been described by Wenzel et al.,[20] the influence of the used lithium metal on cell performance had not been investigated prior to this dissertation. Therefore, a systematic study is conducted to investigate the influence of the lithium metal anode surface on SEI growth kinetics. The results of this study are described in Publication 3.[25] Furthermore, Narayanan et al. found that the reaction kinetics depend on the current density and that different products are formed depending on the amount of lithium available. At higher current densities, the formed SEI consists of the $Li^+$ ion conducting $Li_3P$, among others, and is more homogeneous.[12]

## 2.2 Lithium Metal Anode for Solid-State batteries

To achieve specific energies that can compete with those of LIB, anodes with low potentials and high capacities are required.[10] Possible options include lithium metal anodes, lithium alloys, or reservoir-free anodes.[14,48–53] However, since this thesis focuses on the Li|SE interface, only lithium metal anodes are discussed below.

Lithium is a soft and malleable silvery alkali metal that crystallizes in a body-centered cubic structure with a lattice parameter of $a = 0.35$ nm.[54] It has a density of $\rho = 0.534\ \mathrm{g{\cdot}cm^{-3}}$, a molar volume of $V_m = 13.02{\cdot}10^{-6}\ \mathrm{m^3{\cdot}mol^{-1}}$, and the lowest redox potential at $E_H = -3.04$ V relative to the standard hydrogen electrode. These properties make lithium metal a favorable anode material, offering high (theoretical) volumetric and gravimetric energy density of $W_{vol} = 2061\ \mathrm{mAh{\cdot}cm^{-3}}$ and $W_{grav} = 3860\ \mathrm{mAh{\cdot}g^{-1}}$, respectively.[14] Unfortunately, lithium metal is highly reactive due to its low redox potential and high electropositivity.[54] As a result, lithium readily reacts with almost any material with which it comes into contact, whether in ambient air or SEs.

Generally, lithium metal is obtained by concentrating brines and converting them to LiCl. Pure lithium is then manufactured via electrolysis of the pure molten anhydrous LiCl. Since sodium can greatly affect the reactivity of lithium, sodium and other impurities are removed by distillation.[55,56] However, up to 200 ppm of sodium remains in battery grade lithium.[56] Due to its reactive nature protective measures are required, and the material is usually passivated immediately after production.[14,55,57]

Unfortunately, lithium metal anodes are inherently morphologically unstable at current densities required for commercial applications.[10] Under anodic load, pores form at the interface, leading to a gradual loss of contact.[15,16,58,59] Therefore, the discharge capacity and cycle life are limited by the morphological instability of the lithium metal. However, since lithium stripping is not influenced by interphase formation, the morphological changes during anodic load and possible strategies to mitigate them are not discussed in depth here. Interested readers are referred to the literature.[14,58–67]

Lithium plating can be significantly affected by inhomogeneities at the interface.[68] The presence of a passivation layer on the LMA or the formation of an interphase can lead to uneven current distribution, especially if there are thickness or compositional variations. This uneven distribution affects the local ionic conductivities, resulting in inhomogeneous current distribution.[68–70] Other factors contributing to current focusing include differences between bulk and grain boundary ion conductivity and inadequate contact.[14,71] When the applied current is heterogeneously distributed at the interface, areas of higher current become preferential sites for lithium deposition. If this freshly deposited lithium cannot be rapidly redistributed, it accumulates and dendrites form.[14,68] This accumulation leads to stresses that induce crack formation, which in turn are filled with lithium and exacerbate cracking.[14]

In summary, lithium has a high energy density and low redox potential, which would make it an ideal anode material. Unfortunately, it is also morphologically unstable during cycling and very reactive. This greatly affects cell life and performance, which is why lithium metal anodes have not been used widely in rechargeable batteries. For a more thorough overview of lithium metal anodes, the reader is referred to the literature.[14,67,72,73]

### 2.2.1 Surface Passivation Layers on Lithium Metal

Due to their high reactivity, commercially available lithium metal foils are usually purposely passivated directly after manufacturing to reduce corrosion and to increase safety.[55,57,74–77] This allows the controlled formation of a passivation layer with defined properties and is usually done with gases such as $CO_2$, wax coatings, or polymers.[55,74] Treatments with phosphorous, nitriding or fluorinating agents are also used.[55,76,77] Most passivation layers consist of $Li_2CO_3$ and LiOH after production as these compounds form covering surface films that reduce progressing side reactions.[57,75]

However, over time, the native passivation layer grows and $Li_2O$ is formed in addition to the $Li_2CO_3$ and LiOH already present. This growth depends on the storage conditions. If the foil is stored separately in a clean, inert atmosphere, growth is slower than in a frequently used glove box or in a dry room. Further passivation is driven by reaction with residual water as it alters the reactivity of lithium to gases, such as $N_2$, $O_2$, or $CO_2$.[75]

ToF-SIMS measurements by Otto et al. visualized the structure of the native passivation layer: the top layer consists of $Li_2CO_3$ and LiOH, with a $Li_2O$ layer below, which is in contact with the lithium metal.[57,75] The composition changes with storage time. The LiOH concentration at the uppermost surface decreases with time, while the carbonate concentration increases accordingly. Below the surface, however, the LiOH layer grows significantly. The oxide layer also grows, but at a slower rate.[75]

The native passivation layer, while necessary for safe handling of lithium metal foils, is detrimental to cell performance.[25,75] The low ionic conductivity of its compounds increases the internal cell resistance and is suspected to alter the growth kinetics of the SEI formed at the Li|SE interface. This effect is investigated in more detail at Li|LPSCl interfaces in Publication 3 of this dissertation.[25] Additionally, inhomogeneities in the surface chemistry of the passivation layer can lead to preferential lithium plating causing dendrite formation.[69,70]

However, passivation layers can also be beneficial if the passivation is designed to ensure that the resulting layer has a positive effect on the cell performance. This interphase should prevent decomposition of the SE and should have sufficiently high ionic conductivity as well as a negligible electronic conductivity. Furthermore, the addition of a suitable interphase at the Li|SE interface should improve the interfacial contact and ideally prevent the formation of dendrites.[52] Unfortunately, single-component interlayers such as LiCl, LiF or $Li_3N$ are not suitable as artificial SEIs as they cannot meet all requirements.[52,78,79] Still, there are few studies reporting artificial SEIs in SSBs that meet the most important ones.

Artificial interlayers suitable for industrial applications usually consist of several components, all of which help to achieve the desired properties. Recently, artificial SEI layers consisting of thin amorphous lithium phosphorus oxynitride (LiPON), or a $Li_3N$-LiF composite have been proposed.[78,79] After the activation process, both interlayers reduce interfacial resistance and improve the mechanical contact between SEs and lithium, which overall increase the cycling stability and the critical current density.[78,79]

Since lithium metal should be handled with caution due to its reactivity and general safety concerns, reservoir-free cells can also be an alternative. In these cells, no excess lithium is incorporated during cell assembly, but lithium metal is plated *in situ* during charging. This circumvents undesired side effects due to the passivation layer on the lithium metal, and the Li|SE interface and interphase are formed during an initial formation step. However, the morphology of the deposited lithium is difficult to control and thus, reservoir-free cells are not commonly used.

## 2.3 Lithium Metal | Solid Electrolyte Interfaces and Interphases

### 2.3.1 Types of Lithium Metal | Solid Electrolyte Interphases

According to IUPAC, interphases are defined as "the inhomogeneous space region intermediate between two bulk phases in contact, and where properties are significantly different from, but related to, the properties of the bulk phases. (…)".[80] While an interface is "the plane ideally marking the boundary between two phases.".[80] In other words, an interface can only exist at a thermodynamically stable Li|SE contact, while thermodynamically unstable SEs decompose and form interphases at the contact between lithium and solid electrolyte.

Most electrolytes have narrow electrochemical stability windows in which the electrolyte is stable towards the electrode active materials. At potentials outside this stability window, the electrolyte decomposes and forms products that depend on the potential and chemical composition of the electrode material. The reduction potential depends on the lower oxidation states of the cation framework of the electrolyte, e.g., the reduction of the $PS_4^{3-}$ unit in LPSCl or LPS from $P^{5+}$ to $P^0$ to $P^{3-}$.[40,81–83] The binary products with fully reduced anions, e.g., LiCl, LiF, $Li_2S$ or $Li_3P$, are stable toward lithium metal.[7,40,81–83] Thus, they form an interphase that mitigates the chemical potential gradient of the Li|SE interface and prevents further decomposition.[82] Unfortunately, the molar volume of the interphases is often different from the volume of the electrolyte, thus, additional chemo-mechanical problems may arise during the interphase formation.

The theoretical thermodynamic stability window can be calculated by determining which phases are thermodynamically more stable, the SE and electrode, or decomposition products of both.[40,81–83] Predictions about interface stability can also be made by comparing the molecular orbital energies of the SE with the Fermi energy of the electrode. If the lowest unoccupied molecular orbital (LUMO) of the SE is below the Fermi energy of the electrode material (i.e., lithium metal), the electrolyte is reduced. If the highest occupied molecular orbital (HOMO) is above the Fermi level of the electrode material (i.e., cathode active material), the SE is oxidized.[7] However, these predictions neglect the kinetic influence of the decomposition reaction. Therefore, discrepancies between calculated and measured electrochemical stability windows are to be expected.[84,85]

Since the ionic conductivities of most decomposition products are low compared to that of the SE, the forming interphase increases the cell resistance, charge transfer and cell polarization. This limits the Coulomb efficiency and lifetime of the cell. However, an interphase with beneficial properties could mitigate continuous lithium dissolution and parasitic side reactions.[7] In principle, there are three different types of Li | SE interfaces and interphases,[23] see Figure 1, which are described in more detail below.

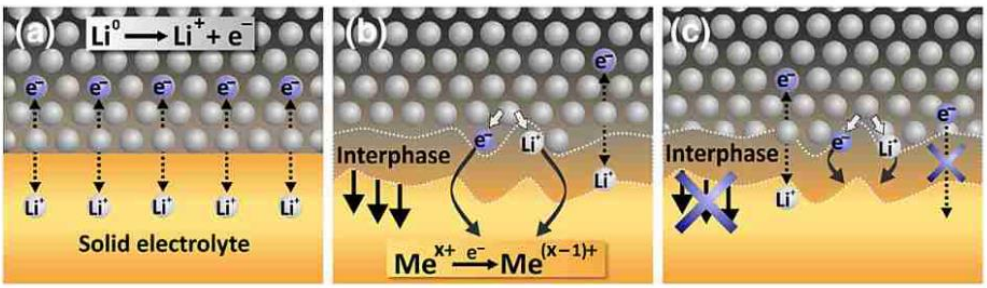


**Figure 1.** There are three types of interfaces between lithium metal and a solid electrolyte: a) The thermodynamically stable interface. And the thermodynamically unstable interfaces b) with both sufficient electronic and ionic conductivity forming a "mixed conductive interphase" and c) with negligible electronic conductivity forming a "solid electrolyte interphase".[23] Reprinted with permission. Copyright © 2015 Elsevier.

#### 2.3.1.1 Thermodynamically Stable Interfaces

Thermodynamically stable interfaces are, as the name suggests, interfaces in which the contacted materials are thermodynamically stable. Thus, no reaction takes place between the two materials. Most materials that are stable against lithium metal are lithium binary compounds, such as $Li_2S$, $Li_3P$ or LiCl. Unfortunately, these materials have low $Li^+$ ion conductivities,[86,87] and are thus not suitable as electrolytes. In addition, most interphases consist of these decomposition products, so a thermodynamically stable interface would be the most suitable to keep the cell resistance low. However, few SEs can be sorted into this category. One notable exception are garnet type SEs such as $Li_{6.25}Al_{0.25}La_3Zr_2O_{12}$ (LLZO), as the Li | LLZO interface is macroscopically stable and does not decompose.[15,88,89] Nevertheless, a phase transition from the cubic to the tetragonal LLZO phase occurs, forming a stable interphase layer with a thickness of approx. 6 nm, which may prevent decomposition.[89]

#### 2.3.1.2 Mixed Conducting Interphase

If the SE is thermodynamically unstable against lithium metal, two different interphases can form, one of which is the so-called mixed conducting interphase (MCI).[23,90] An MCI forms when the decomposition products have sufficient electronic and ionic conductivity.[19,23] This allows electrons and lithium ions to diffuse through the MCI and recombine at the interface between MCI and SE, forming lithium metal, which reacts with the electrolyte and causes continuous interphase growth. In particular, SEs that contain metal(loid) ions tend to form an MCI when in contact with lithium metal because the reduced cations form electronically conducting compounds.[19,21–23]

One of the first thiophosphate SEs for which the MCI formation was studied in detail is $Li_{10}GeP_2S_{12}$ (LGPS).[19,24,91] *In situ* X-ray photoelectron spectroscopy (XPS) measurements show that LGPS decomposes and forms elemental germanium or a Li-Ge alloy. Thus, electronically conductive compounds are formed during decomposition. However, their amount is not high enough for the formation of electronic percolation pathways. Thus, the germanium presumably accumulates at interfaces of the nanostructure or grain boundaries and locally increases the electronic conductivity.[19,91] Similar results are found in Publication 1 and 2 of this thesis for the Li|LMC (M = In, Y) and Li|LiSiPS interfaces, respectively.[21,22]

#### 2.3.1.3 Solid Electrolyte Interphase

The other interphase that can be formed between an SE and lithium metal at a thermodynamically unstable interface, is the solid electrolyte interphase.[23,90] This phase is metastable as the interphase is ionically conducting but with a negligible electronic conductivity. Therefore, this interphase can also be regarded as an additional, amorphous SE consisting of the reduction products of the electrolyte used. Due to the minor electronic conductivity, not enough lithium metal can be formed to drive the interphase formation, thus, it should stop once a certain layer thickness is reached.

In Publication 3 of this thesis, the SEI growth kinetics of Li|LPSCl with differently treated lithium was investigated.[25] Interestingly, the kinetics depends on the surface treatment of the lithium metal. When the surface is freshly prepared, the interphase formation is self-limiting. However, if commercial lithium metal foils with a passivation layer are used, the interphase formation continues throughout the experiment.[25] Unfortunately, reliable information is currently unavailable on the partial conductivities of the decomposition products and possible interactions, such as the formation of space charge layers at the interfaces of the decomposition products. Therefore, the reason for the observed differences remains unclear. In addition, further studies are required to investigate the formed SEI morphologies as this may be a factor causing continued reaction.

### 2.3.2 Material Characterization of Lithium Metal | Solid Electrolyte Interphases

Characterizing the interface between two materials by analytical methods is often difficult as a forming interphase may be very thin and is buried in the sample.[92–94] Usually, the interphase is too deep within the sample for surface sensitive characterization methods, e.g., XPS or Raman spectroscopy.[92,94] Additionally, the forming interphase cannot be investigated with analytical methods that have a higher detection depth as the interphase signal is superimposed by the signals of the contacted materials.[92,94] Thus, the interface characterization is often a compromise between experimental necessities and recreating representative conditions.[94]

Few studies on the Li|SE interface using transmission electron spectroscopy (TEM) have been conducted so far due to a limited range of preparation methods and the high beam sensitivity of the SEs.[89,95] Ma et al. brought lithium and LLZO into contact *in situ* and observed the transition from the cubic to the tetragonal phase for the first few unit cells.[89] The interphase between $Li_{1+x}Al_xGe_{2-x}(PO_4)_3$ and lithium on the other hand, was found to be amorphous with increases in volume.[96] Using this method, Dixit et al. observed that iodine diffuses into the lithium at the interface with LiI-doped LPS with and without electrochemical bias.[97]

X-ray computed tomography (CT) is another imaging technique that is used to study the Li|SE interface and the chemo-mechanical failure mechanisms in cells. While it is mainly used to study the formation of dendrites and voids at the Li|SE interface, as well as the crack formation of the SE,[97–101] it can also visualize the interphase formation upon contact or during cycling.[98,99] CT measurements during cycling experiments in both symmetric $Li|Li_{10}SnP_2S_{12}|Li$ and $Li|Li_{1+x}Al_xGe_{2-x}(PO_4)_3|Li$ cells revealed that plated lithium is mostly consumed during interphase formation and that the volume expansion of the interphase induces cracks in the respective cells.[98,99] Using CT and TEM together helps to understand the relationship between stress evolution in the cell and interphase instabilities as both methods complement each other on different length scales.[97,98]

Otto et al. recently showed that ToF-SIMS measurements can be used to differentiate if a SE is stable or forms an SEI or MCI.[26] For this, lithium is deposited on the sample and a depth profile of the Li|SE bilayers is measured. Each interface type has a characteristic depth profile, see Figure 2. Thermodynamically stable interfaces as shown in Figure 2a and b) have only signals from the lithium metal in the beginning. Once the inert substrate is reached, the corresponding signals increase rapidly. SEI-forming electrolytes show SE-related signals already at the beginning of the profile that increase until a maximum is reached at the interphase, see Figure 2c. Once the SE region is reached, these signals decrease slightly, and additional SE-related signals appear. If an MCI is formed at the Li|SE interface, strong SE-related signals are measured from the start without any additional SE-related signals emerging during the depth profile (Figure 2d).[26]

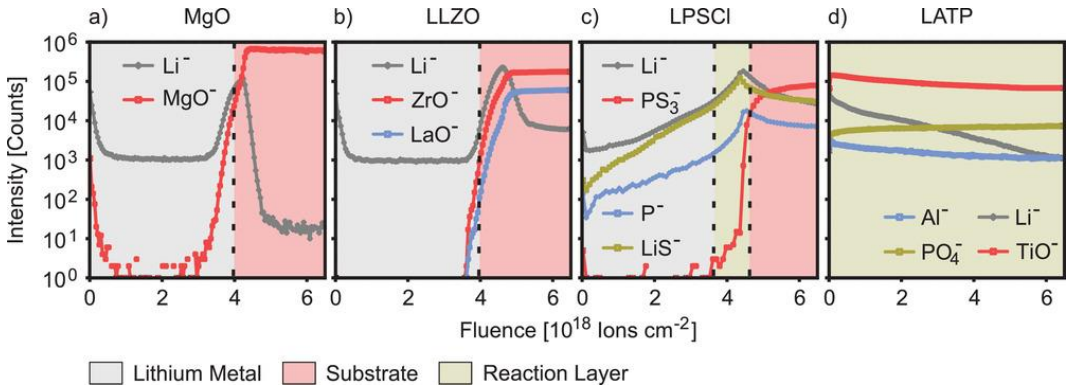


**Figure 2.** ToF-SIMS depth profile of a) Li|MgO, b) Li|LLZO, c) Li|LPSCl and d) Li|LATP ($Li_{15}Al_{0.5}Ti_{15}(PO_4)_3$) interfaces. For this, 3 µm of lithium were deposited on the substrate using vapor deposition and subsequently a depth profile was measured.[26] Reprinted with permission. Copyright © 2022 Wiley-VCH GmbH.

If the profile is ambiguous, unclear cases can be clarified by depositing different lithium thicknesses or by using different storage times and comparing the resulting depth profiles.[26] Furthermore, this method can be used to resolve seemingly contradictory results from other experiments. This was the case, for example, for the Li|LiSiPS interface studied in Publication 2 of this thesis.[21] For more detailed information on the method, the reader is referred to the work of Otto et al..[26]

Auger electron spectroscopy (AES) is another method to gain chemical information of a surface. Additionally, it can be displayed as a map and thus provide information of the chemical distribution of the sample as well. Using this method, Wood et al. show that the SEI formed at the Li|LPSCl interface is heterogeneously distributed, forming $Li_3PO_4$ domains, redox active $Li_{3-x}P$, and irreversibly formed $Li_2S$.[93] Furthermore, Kim et al. used this technique to show that a homogeneous pressurization of the cell is essential for stable cycling as the lithium migration is pressure dependent.[102]

#### *2.3.2.1 X-ray Photoelectron Spectroscopy*

As X-ray photoelectron spectroscopy was one of the main techniques used for this dissertation, it is described in greater detail than the other material characterization methods. Readers already familiar with XPS and *in situ* deposition methods used in combination with XPS may skip this chapter.

*Basic Principle of XP-Spectroscopy*

X-ray photoelectron spectroscopy is a surface-sensitive and non-destructive technique that analyzes the chemical composition of a sample. This measurement technique is based on the photoemission process. Here, a photon transfers its energy to an atom's electron, when a sample is irradiated with X-rays, resulting in electron emission from the atom. However, if the energy of the incident photons is smaller than the electron's binding energy, the electron cannot leave the atom. In addition to photoelectrons, Auger electrons can also be emitted during XPS measurements. During this process, an electron drops from an outer orbital into an unoccupied inner orbital, releasing its excess energy. This excess energy can emit a second electron, known as Auger electron. The energy of Auger electrons is independent of the energy of the initial X-ray source.[103]

This technique has a micrometer-scale lateral resolution and a probing depth in the low nanometer range (1-10 nm) since only electrons close to the surface can leave the sample without complete energy loss. However, the depth resolution can be significantly improved by combination with ion etching. All elements except for hydrogen and helium can be detected with this method at concentrations greater than 0.1 at-% and their concentration can be determined semi-quantitatively.[103]

To determine the kinetic energy (KE) of the emitted electrons, a hemisphere analyzer is employed since it only allows electrons with specific energies to pass through it. After passing through the analyzer, the number of electrons with a specific kinetic energy is counted using an electron detector. Based on the measured KE, the binding energy (BE) can be calculated using the following equation:

$$BE = h\nu - KE - \Phi_S \quad (1)$$

with $h\nu$ as the energy of the photon and $\Phi_S$ as the spectrometer work function. Typical X-ray sources are monochromatic Al $K_{\alpha 1}$ (1486.7 eV), or Mg $K_\alpha$ (1253.6 eV) radiation. Newly emerging anodes are Cr $K_\alpha$ (5415 eV) and Ag $L_\alpha$ (2984 eV).[103] A schematic diagram of a spectrometer along with the relevant energy levels is shown in Figure 3.

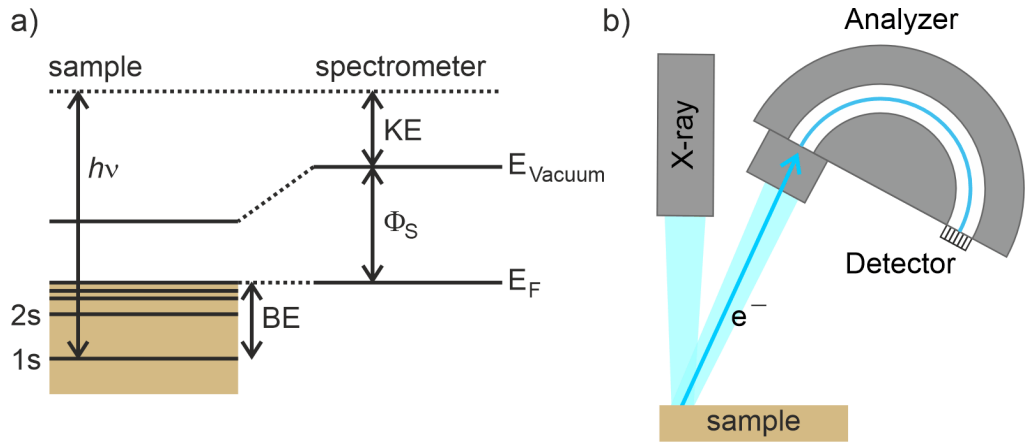


**Figure 3.** a) Energy levels of an electrically conducting sample. As the sample is grounded to the spectrometer the Fermi levels ($E_F$) align. B) schematic setup of an XP spectrometer.

The electron distribution of an atom is influenced by its chemical environment, which affects the binding energy. Therefore, measuring changes of the binding energy can provide information about the chemical environment of the measured element. These changes are referred to as chemical shifts.[103] For more detailed information, the reader is referred to literature about this method.[103,104]

*Charge Neutralization*

During XPS measurements, electrically isolated, insulating, or semiconducting samples can become charged due to the electron emission, resulting in a buildup of positive charge at the surface that cannot be compensated by contact to ground. As a result, shifts in the measured binding energy of the respective orbital can occur.[105] Moreover, if the surface potential varies or is inhomogeneous, either horizontally or vertically, the sample may become differentially charged during the measurement. This can cause broadening or deformation of peaks, and shifting of peak positions.[105–108] Therefore, it is important to consider not only chemically induced changes of the binding energy but also the measurement conditions when evaluating XP-spectra.

To overcome the issues of (differential) charging, charge neutralizers can be used to keep the sample potential consistent. In this case, the sample potential is floating and determined only by the charge neutralization, which is independent of the sample conductivity.[105,109] Modern instruments typically use dual beam neutralization with low energy electrons (~1 eV) and $Ar^+$ ions (≤10 eV) to compensate for positive and negative charges, respectively.[105] Before the measurement results can be interpreted, the spectra must be shifted to correct the charging effect accordingly.[105,109]

The combination of samples insulated from ground and dual charge compensation was also used in this doctoral thesis. To ensure that the measurements did not alter the samples, a series of consecutive measurements were conducted, and the results were compared. This proved that charge neutralization and the XPS measurement itself did not alter the surface of halide and thiophosphate SEs. However, it is essential to note that these findings are not universally applicable, and that the test must be repeated for each studied type of electrolyte.

If charge neutralization is used in combination with a grounded sample, two potentials are applied to the sample, which can result in a potential gradient within the sample. This, in turn, may amplify differential charging and lead to changes in peak shapes, binding energies, and even sample damage.[105,107] Therefore, it is important to insulate samples from ground when utilizing charge neutralization. However, in cases where a potential gradient is intended, such as when creating a "virtual electrode" (see below), careful consideration of possible side effects is necessary.

*Measurement Methodologies*

In principle, three different methodologies can be used for characterizing samples with XPS: *ex situ*, *in situ* or *operando* measurements. These methodologies differ depending on when the sample is analyzed relative to the experiment. *Ex situ* measurements are performed after the experiment, while *in situ* measurements are performed on-site of the experiment. *Operando* measurements, on the other hand, involve analyzing the sample simultaneously with the experiment. An important difference between an *in situ* and an *operando* experiment is that the *in situ* measurements capture the sample in a “relaxed” state, while *operando* measurements are fast enough to detect even metastable states.[94]

*Ex situ* measurements offer a good overview of system conditions and failure mechanisms, but they cannot reveal insights into dynamic processes during operation.[94] Moreover, sample changes may occur during disassembly and sample transfer due to the high reactivity of lithium metal, SEs and their decomposition products to residual gases, such as water, oxygen, nitrogen or organic species.[75,93,94,110,111] Probing a Li|LPSCl sample with soft and hard X-ray photoelectron spectroscopy (SOXPES and HAXPES, respectively) provides depth-resolved data on these side reactions. This experiment demonstrates that the lithium surface is completely oxidized during transfer, more carbon species are detected on the surface, and the $Li_2S$ formed upon contact is buried.[110]

In contrast, *in situ* or *operando* measurements can avoid changes in the studied surface due to side reactions.[57,93,110,111] However, it is important to consider that the pressure, due to the ultrahigh vacuum (UHV) required for XPS measurement, significantly differs from atmospheric pressure or higher pressures often required in many applications. Furthermore, the currents applied in the experiment may differ from those in regular cycle experiments. Nevertheless, a significant advantage of *in situ* or *operando* experiments is the ability to measure dynamic processes, such as intermediate steps of the decomposition reaction. Therefore, *in situ* or *operando* measurements provide valuable information on the interfacial and interphase evolution. *In situ* measurements are one of the main methods used in this doctoral thesis.

*Combining XPS Measurements and Lithium Deposition*

The Li|SE interface can also be studied in model systems by depositing thin lithium layers on top of electrolyte samples and subsequently performing *in situ* or *operando* XPS or HAXPES measurements.[94] Lithium deposition can be performed through three methods: *in situ* sputter deposition, *in situ* or *operando* electrochemical plating using the electron neutralizer, and *ex situ* vapor deposition in an adjacent preparation chamber. A schematic representation of these processes is illustrated in Figure 4. In comparison to the other two methods, the sputter deposition method is discussed in greater detail since it was used in Publications 1 and 2 of this dissertation.[21,22]

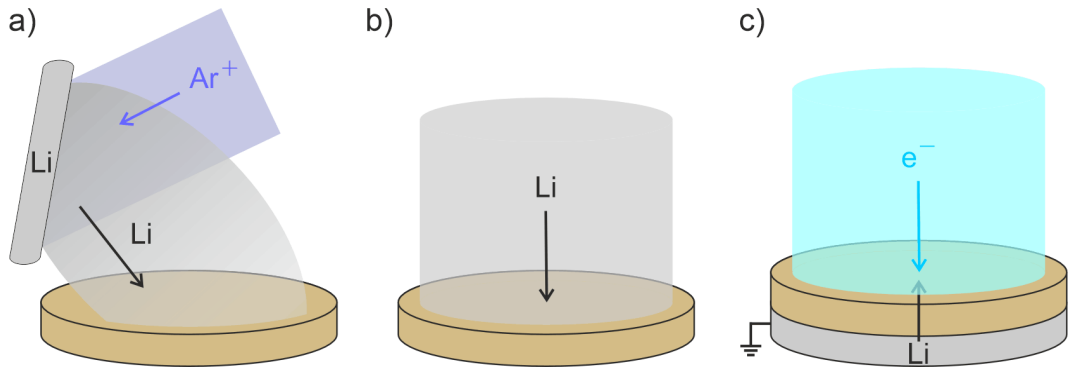


**Figure 4.** Schematic representation of *in situ* lithium deposition on the surface of the SE. Lithium can be deposited using a) sputter deposition with the $Ar^+$-ion gun and a lithium target mounted on the sample holder, b) vapor deposition of lithium, or c) creation of a "virtual electrode" using the electron neutralizer and a grounded lithium reservoir beneath the SE.

*In situ* lithium sputter deposition was initially introduced by Hartmann et al.[18] Wenzel et al. further optimized the setup,[23] and utilized it in combination with impedance spectroscopy to investigate the interphase formation of SEs, such as LPSCl, $Li_7P_3S_{11}$ or LGPS.[19,20,112] Similarly, the present thesis employs the stepwise deposition of thin lithium metal films to study the interphase formation of various SEs towards an LMA.[21,22] Especially, the reduction stability of thiophosphate SEs, such as LPSCl and LiSiPS, or halide SEs, such as LIC and LYC, against lithium metal was studied.

For the deposition of lithium, the argon ion gun of an XP-spectrometer is utilized as a sputtering source to deposit lithium from a target onto the sample surface,[23] see Figure 4a. Usually, the ion gun is employed either for neutralizing the sample surface during measurement or for sputtering a depth profile of the sample. To realize deposition within the XPS chamber, a special sample holder carrying a target holder, as well as the sample, is needed. The target holder carries the grounded lithium foil and is attached at an acute angle for the plasma cloud to deposit primarily on the sample surface that has a floating potential.

During sputter deposition, the sample holder is lowered from the measurement position and turned towards the ion gun, causing the $Ar^+$ ions to hit the lithium. The layer thickness of the deposited lithium film can be adjusted by varying the acceleration voltage of the $Ar^+$ ions as well as the deposition time. Subsequently, XP-spectra of the elements present in the electrolyte are measured, and both steps are repeated multiple times.

Different information about the Li|SE interface can be obtained depending on the amount of lithium deposited on the SE. Deposition of thin lithium films in multiple steps allows detailed identification of decomposition products before the lithium film attenuates interphase signals or excessive sputter damage occurs (see discussion below). Following the initial interphase formation, larger lithium deposition steps can be employed to differentiate between the formation of an SEI or MCI. If the interphase is an SEI, the decomposition reaction eventually ceases, leading to the formation of a lithium metal film on top of the interphase detectable in the Li1s spectrum.[20] However, if an MCI is formed, ideally no lithium metal film develops, as the lithium is continuously transported into the material and further reacts with the SE.[19,21–23]

Nonetheless, kinetic inhibitions can slow down the transportation of lithium into the sample, leading to the formation of a lithium film. To distinguish between the different scenarios, waiting steps during measurement or additional measurements of aged samples can be included. It should be noted that careful consideration of the results of these types of measurements, independent of the deposition method, in combination with other analytical methods is necessary to achieve an accurate understanding of the interphase formation at the Li|SE interface.

This method was used to investigate the lithium stability of various SEs.[19–23,112] If the SE in question, e.g., $Li_3P_4$ or $Li_6PS_5X$ (X = Cl, Br, I), contains only ions that form electrically insulating decomposition products, such as $Li_2S$, $Li_3P$ and LiX (X = Cl, Br, I), the formed interphase is stable (SEI).[20,112] However, if the SE contains metal(loid) ions, these ions are reduced upon contact forming a mixed conducting interphase that growth continuously (MCI).[19,21,22]

As mentioned above, two other techniques for lithium deposition have been reported in the literature: "virtual electrodes" induced by electron neutralizer, or evaporation in an adjacent deposition chamber. These methods have been reported in several studies.[12,24,93,110,113,114] For vapor deposition, thermal heating or an electron beam is used to evaporate lithium metal, creating a lithium film, see Figure 4b.[110,111,113] This technique enables the rapid deposition of layers in the nanometer and micrometer range, and thus, provides an abundant source of excess lithium.

The third technique for lithium deposition is the creation of a "virtual electrode" induced by the electron neutralizer of the XP-spectrometer, see Figure 4c. When a grounded Li|SE sample is irradiated with an electron beam, a negatively charged surface is formed, creating a potential gradient between the SE surface and the grounded lithium reservoir. Due to this potential gradient, lithium ions migrate to the electrolyte surface. And, upon reaching the pellet surface, the $Li^+$ ions recombine with the electrons, forming an Li|SE interface.[24,93,94,110,113] This method is comparable to the lithium deposition in reservoir-free cells.[12,113] Furthermore, the amount of lithium plated on the surface is influenced by the current of the electron beam. However, the actual amount of charge applied must be measured with the stage, since the electron beam diameter is usually larger than the sample and thus possible deviations can occur.

If a SE that forms an SEI is used, lithium metal can be detected on the surface, which is not the case for MCI-forming electrolytes.[24] The sample can also be cycled by using an additional UV light to strip the lithium away from the studied surface.[93] A study using both techniques revealed that $Li_xP$ ($0 < x \leq 3$) is redox-active, and the stoichiometry depends on the available lithium.[93] Also, by varying the beam current of the virtual electrode the influence of the kinetics on the decomposition reaction can be studied.[12]

*Examining the Impact of Deposition Methods on Measurement Results*

Before discussing the impact of the deposition method on measurement results, it is necessary to consider the kinetic energy of the atoms involved in the respective methods. Not only the thermodynamic stability is important when studying the Li|SE interface but also the kinetic energy of the impacting lithium as this can significantly impact the formation of decomposition products. According to literature, the energy distribution of sputtered particles has a maximum at a kinetic energy $E_{kin,\,max}$ of:[115]

$$E_{kin,\,max} = \frac{E_{sb}}{2(1\text{-}m)} \tag{2}$$

With $E_{sb}$ as the surface binding energy of the target material and $m$ as an energy-dependent parameter with $0 \leq m \leq 0.25$.[115]

The surface binding energy of lithium metal is $E_{sb}(Li) = 1.68$ eV/atom,[116] resulting in a maximum energy distribution of approx. 1 eV for lithium. Unfortunately, there is no available literature on the yield and energy distribution of lithium sputtered with $Ar^+$ ions, leaving the maximum energy of lithium reaching the sample surface during *in situ* deposition unknown. In general, the sputtering rate and the energy distribution of the sputtered (here Li) or reflected particles (here $Ar^+$) depend on factors such as the incident ion energy, mass ratio of particles involved, ion incident angle, and scattering angle.[117]

In the case of sputtering lithium with argon, the sputtering process of silicon with xenon can be used as an approximation due to their similar mass ratios. For this combination, the sputtered silicon has a maximum energy of 60%, and the scattered xenon has a maximum energy of 10% of the incident ion energy.[118] This approximation suggests that particles with high kinetic energies could reach the surface, potentially triggering reactions or differentially sputtering the sample surface themselves. However, further studies are necessary to confirm the validity of using the $Xe^+ \rightarrow Si$ system as an approximation for the $Ar^+ \rightarrow Li$ sputtering process.

In contrast, vapor deposition is a gentler method that causes minimal damage during deposition.[110,113] This is because the internal energy of lithium atoms during evaporation is only about 0.1 eV/atom, assuming a crucible temperature of 450 °C. For LLZO, the interface made by vapor deposition did not show the formation of an oxygen deficient interphase layer (ODI), that can be observed by other *in situ* deposition methods or by TEM measurements.[89,113] Therefore, it might also be possible that kinetic barriers to the SE reduction cannot be overcome by such low energies.[113] Additionally, it is also possible that the lithium atoms do not have sufficient energy to penetrate an impurity layer, such as adventitious carbon or carbonates, on the surface. Due to this the electrolyte would be at least partially protected from contact with the lithium metal and a higher stability of the Li|SE interface may be indicated than is the case.

While no lithium is deposited from vacuum when depositing lithium via a “virtual electrode”, this *in situ* deposition method can still influence the results. Here, electrons are accelerated with 1.4 V by the neutralizer and are directed at the surface of a grounded sample, charging the surface to approx. 1.4 V. As a result of the surface charging, the virtual electrode acts as an applied potential in a reservoir-free cell and can impact the electrolyte. Therefore, it is important to consider the virtual electrode as a potential source of surface changes, particularly if the applied potential falls below the electrochemical stability window of the studied SE.

Two studies, by Connell et al. and Gibson at al., compare the effects of the different lithium deposition methods on LLZO and LPSCl, respectively.[110,113] Both studies find that the formation of decomposition products varies depending on the deposition method, but their explanations for the observed phenomena differ. Connell et al. observe an ODI at the Li|LLZO interface for sputter deposition, which is also observed with other methods,[89] but this effect is not observed with vapor deposition.[113] However, when a virtual electrode is used, an ODI is also observed, demonstrating that the potential applied by the virtual electrode for lithium growth is sufficient for ODI formation. They conclude that the energy of the evaporated lithium is too low to overcome the kinetic barrier, which is not the case for the other two methods.[113]

In contrast, Pasta and colleagues utilized LPSCl to compare the three deposition methods and reach a different conclusion.[12,110] Their measurements show lower concentrations of certain compounds, such as carbonates or adventitious carbon, when lithium is deposited via sputter deposition.[110] Additionally, the stoichiometry of the formed phosphorus reduction compounds depends on the deposition method. While $Li_3P$ is formed during plating, $Li_xP$ ($0 < x < 3$) is formed during vapor deposition, and no reduced phosphorous can be observed after sputter deposition of 10 nm lithium.[110] However, for thinner sputtered lithium films both $Li_3P$ and $Li_xP$ were observed.[12,110] The authors conclude, that these compounds are removed and that interfacial mixing might occur due to bombardment with the $Li^+$ ions.[110]

To verify these conclusions, they applied similar methods on single layer graphene samples (SLG) deposited on $SiO_2$/Si substrates and measured the damage with Raman spectroscopy. While radiation damage to SLGs can be easily measured by Raman spectroscopy, it is essential to consider that the covalent bonds in SLGs can be easily damaged. Therefore, it is crucial to carefully evaluate whether damage to SLGs also results in damage to ionic bonds such as those present in SEs that are not polymers.

No damage was observed for lithium evaporation. In contrast, the SLG surface is clearly damaged for lithium sputter deposition, with the damage increasing with the amount of deposited lithium.[110] Unfortunately, as stated above, no experimental data on the actual sputter yield and energy distribution exist for the $Ar^+ \rightarrow Li$ sputtering process. Thus, further experiments are necessary to gain insight into the sputter process to minimize the inflicted damage caused by sputter deposition.

Some XP-spectrometers only have dual-mode charge neutralization which cannot be controlled individually. Thus, $Ar^+$ ion flux cannot be turned off during lithium plating via virtual electrode, only minimized.[119] Additionally, the sample needs to be grounded for this deposition method to enable $Li^+$ ion migration. For this reason, there are no shielding effects as there are when a sample is neutralized at the floating potential. To study the influence of $Ar^+$ charge neutralization on the grounded sample surface independent of the electron flood gun, Gibson et al. irradiated a grounded SLG sample with slow $Ar^+$ ions for 38 min. This leads to changes in the Raman spectrum, showing that the sample is damaged by the $Ar^+$ ions.[110] This highlights that the use of neutralizers and the potential (grounded vs floating) of the sample is critical when studying battery materials. For this reason, individual control of charge neutralization is mandatory for the instrument.

To assess the impact of the virtual electrode on the sample, SLGs were irradiated with either 20 µA or 30 µA for a duration of 4.5 hours.[110] Taking into account that the electron neutralizer used by Pasta and coworkers has a diameter of 5 mm,[12] approx. 20 to 30 µm of lithium would have been plated during this time.[110] This amount of lithium deposition is considerably higher than what would be suitable for studying an SEI, as no XP-signal of the SEI compounds would be detectable. For example, another study by the same group utilizes the virtual electrode for only ~10 min, resulting in a film thickness of approx. 120 nm.[12] Thus, the observed damage may be stronger than in an actual measurement and depend on the electrolyte material.

As already mentioned above, no changes due to charge neutralization or the X-ray beam itself occurred for the various thiophosphate and halide SEs used in this work. Thus, the influence of the charge neutralizers can be neglected for the results of this thesis. Beam damage from neutralizing the sample is thus not a universal issue, and the beam stability depends strongly on the studied material. Additionally, as mentioned above, it is crucial to include in the stability evaluation whether the sample was grounded or not during the experiment.

In summary, vapor deposition is unlikely to change the surface significantly due to the low energies of the deposited atoms. However, it may offer higher stabilities by potentially protecting surface contaminants. In contrast, the sputter process involves particles with energies at least ten times higher than those in vapor deposition, which can easily penetrate the top layer. However, this higher energy may also influence the decomposition reaction or cause sputter damage. For lithium plating with a virtual electrode, beam damage due to the electrons might be induced.

Moreover, current comparative studies show partly contradictory results. Therefore, further work is necessary to compare the influence of the respective deposition method on the decomposition reaction. Careful consideration of the influence of the deposition method on the studied system is also essential. To avoid the pitfalls of the respective deposition method, additional measurements are mandatory to validate the findings. A non-invasive method to study interphase evolution is impedance spectroscopy, which is discussed in the following section.

### 2.3.3 Electrochemical Characterization of Lithium Metal | Solid Electrolyte Interphases

Impedance spectroscopy is a non-destructive characterization method for monitoring transport processes in an SSB. For this purpose, a small periodic stimulation signal, e.g., an alternating potential, is applied and the response signal, e.g., the current response and its phase shift, is measured. By gradually changing the frequency $\omega$, the impedance response of the measured system is examined.[120] Typical frequencies for measuring the impedance are $10^7 – 10^{-3}$ Hz.

In principle, there are three basic elements with which impedance responses can be described: a resistor with a resistance *R*, a capacitor with a capacitance *C*, and an inductor with an inductance *L*. Their impedance *Z* can be described with the following equations:[120]

$$Z_R = R \tag{3a}$$

$$Z_C = \frac{1}{i \cdot \omega \cdot C} \tag{3b}$$

$$Z_L = i \cdot \omega \cdot L \tag{3c}$$

Since the processes observed in SSBs are often non-ideal due to inhomogeneities or porosity, constant phase elements (CPE) *Q* are used instead of capacitors to better describe the impedance response. This element can be described in the following way:[120]

$$Z_Q = \frac{1}{Q_0 \cdot (i \cdot \omega)^{\alpha}} \tag{4}$$

The exponent $\alpha$ is a constant with values between −1 (the CPE is purely inductive), 0 (the CPE is purely resistive) and 1 (the CPE is an ideal capacitor).[120,121] In this thesis $\alpha$ is close to but less than 1 to describe the imperfect capacitance response of the studied processes.

Electrochemical systems are described effectively using a combination of resistors, capacitors, and constant phase elements. These components provide a comprehensive understanding of various aspects within this system. For example, the migration of ions in SEs, whether in the bulk or along grain boundaries, can be described using parallel *RQ* elements.[15,71,121,122] Similarly, the evolution of interphases can also be explained using this equivalent circuit.[19–22,25,112]

In general, the ionic conductivity and dielectric constant determine the characteristic frequency of the respective process.[123,124] Therefore, the impedance response gradually decreases with measurement frequency from processes with high conductivities and low dielectric constants to processes with low conductivities and high dielectric constants.[123,124] Consequently, the measurement of the impedance response of a cell captures the bulk contributions at high frequencies. In the frequency domain, as the frequency decreases, the measurement reflects the contributions from grain boundaries and interphases.[121,122,125] At lower frequencies, interface contributions such as charge transfer, and self-diffusion of lithium can be assessed.[121]

However, if the ionic conductivity of the SE is exceptionally high, the impedance response of the bulk or grain boundaries might be out of the measured frequency range. To distinguish between these processes, measurements at lower temperatures are required, as this slows lithium migration. The low temperature measurements are then used to determine room temperature conductivity.[37,41,45,121,122] For more detailed information on impedance spectroscopy the reader is referred to the literature.[120]

In this thesis, impedance spectroscopy was used to study the interphase evolution of various Li|SE interfaces in symmetric Li|SE|Li cells at room temperature. The impedance response of the formed interphase, which generally has a lower ionic conductivity, can be accurately measured at room temperature. Typically, these systems can be described by several *R* and *RQ* elements. If the conductivity is very high, the characteristic frequency lies outside of the measuring range and the capacitance cannot be calculated reliably. Therefore, this process is usually only described by a single *R* element. For highly conducting SEs, the bulk and possibly also the grain boundary conductivity are often described this way. Depending on the number of further processes, additional *RQ* elements are used to describe the grain boundary and interphase processes. In Figure 5 an *R*-*RQ* equivalent circuit is shown.[21,22]

A commonly used method for the representation of impedance spectra are Nyquist plots. Here, the negative imaginary part of the impedance is plotted against the real part of the impedance.[120,121] Figure 5 shows the impedance of a Li|LPSCl|Li cell as an example. For this system, an *R*(bulk)-*R*(SEI)*Q*(SEI) equivalent circuit is used because both the bulk and grain boundaries have high conductivities, resulting in the fitting process yielding a combined resistance value *R*(bulk). It is important to note, however, that the signals at low frequencies to which charge transfer at the Li|SEI interface and lithium self-diffusion respond are not fitted here since the focus is on the SEI evolution.[25] Using this method, the interphase growth kinetics are studied in this thesis.

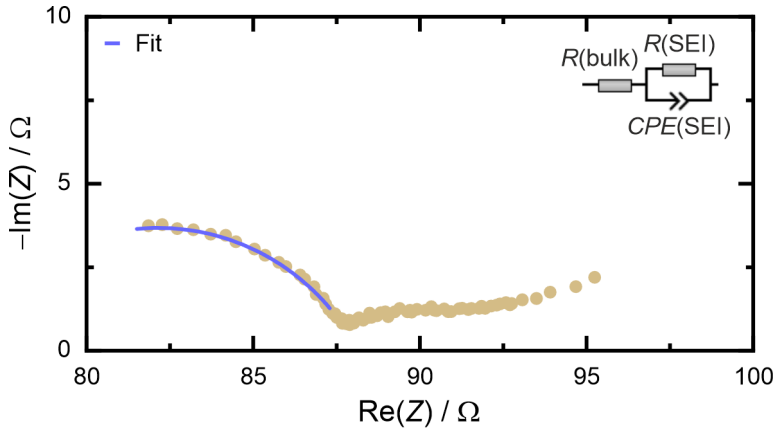


**Figure 5.** Nyquist plot of a symmetrical Li|LPSCl|Li cell. A *R*(bulk)-*R*(SEI)*Q*(SEI) equivalent circuit is used to fit the contribution of the LPSCl and the forming SEI. The measured frequency range was between 1 MHz and 100 mHz.

While impedance spectroscopy is an excellent method to obtain information on conductivities, interfacial evolution, or diffusion processes, it does not provide information on chemical processes.[12] Therefore, a combination with chemical analysis methods is required to fully understand the processes, e.g., chemical degradation in cells.

#### *2.3.3.1 Measurements with a Reference Electrode Cell Design*

In conventional two-electrode cells, the contribution of both electrodes and the electrolytes are measured, e.g., cell potential or impedance response. However, since the entire cell is measured, signals superimpose, making it difficult to interpret the measurements results.[126] To overcome this and unequivocally measure the properties of one half-cell, measurements with a reference electrode (RE), i.e., in a three-electrode cell setup, are required. This way, both half cells can be measured separately against the reference electrode.[126–129]

Figure 6 shows the impedance response of a symmetric Li|LPSCl|In/InLi@Ni|LPSCl|Li cell used in Publication 3 to separate the impedance response of both SEI contributions.[25] Here, a nickel mesh covered in 3.8 µm In/InLi is used as the RE to separate the impedance response of the working electrode (WE) and counter electrode (CE). The impedance response of the full cell is the sum of the half-cells.

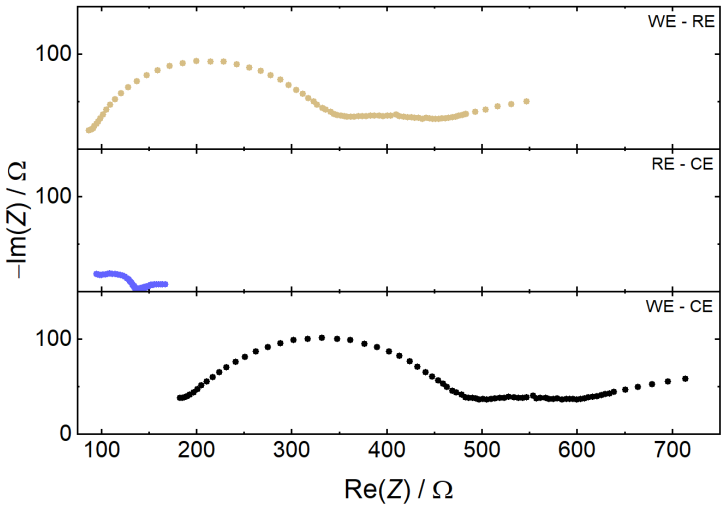


**Figure 6.** Nyquist plots of the impedance response of both half-cells, working electrode (WE-RE, brown) and counter electrode (RE-CE, blue) against the reference electrode, respectively, as well as the full cell (black) of a symmetrical Li|LPSCl|In/InLi@Ni|LPSCl|Li cell. The measured frequency range of the cell was between 1 MHz and 100 mHz.

To obtain reproducible results, the reference electrode in an SSB must meet three criteria.[127] A constant chemical potential is required, since the potentials of both half-cells are measured against the potential of the RE.[127] Therefore, if potential of the RE is not stable, the measurements are erroneous. In addition, there should be no or minor side reactions between RE and the SE, as these can change the chemical potential of the RE.[127] Furthermore, the reference should not distort the electric field within the cell, as this affects the impedance measurement, leading to signal artefacts.[127,128,130,131] Both, the RE position relative to the electrodes, and the position of both electrodes relative to each other, can affect the electric field.[127,128,131] Placing the RE next to the electrodes, either as a ring or as a separate disc, distorts the electric field and therefore affects impedance measurements of these cells.[127,130] Therefore, the RE must be implemented within the SSB, which is experimentally challenging.

Two cell designs that have been successfully implemented in SSBs are mesh-shaped REs and µ-sized wire-type REs.[25,126,129,132] Wire-shaped REs are easier to assemble and inhibit $Li^+$ migration less. Mesh-shaped REs, on the other hand, are more tedious to fabricate and may inhibit $Li^+$ migration if the mesh size is too small. However, because of their larger surface area compared with a wire, mesh-like RE have a lower impedance and are less prone to artifacts caused by asymmetries.[127,128] Which of the two setups is better suited to obtain the desired information needs to be assessed for each individual cell system. Nevertheless, both setups separate both electrode impedances well.[25,126,129,132]

### 2.3.4 Theoretical model of interphase growth

Since SEI growth changes the internal resistance of the cell, it is important to quantify the change in order to estimate the long-term evolution. Impedance measurements on symmetric Li|LPSCl|Li cells show that the SEI growth follows a parabolic rate law, indicating a diffusion-controlled process.[20] Therefore, Wenzel et al. modified the Wagner's model describing diffusion-controlled solid-state reactions to quantify the interphase growth.[20,90] The derivation of this model is described in detail in the dissertation of S. Wenzel,[90] and describes the SEI resistance $R$(SEI) with the following equation:

$$R(\mathrm{SEI}) = \frac{1}{A} \cdot \frac{\sigma_{\mathrm{el}}^{0.5}}{\sigma_{\mathrm{ion}}} \cdot \left( \frac{2 \cdot M_{\mathrm{SEI}} \cdot \mu_{\mathrm{Li}}^{0}}{F^2 \cdot \rho_{\mathrm{SEI}} \cdot x} \right)^{0.5} \cdot t^{0.5} = k' \cdot t^{0.5} \tag{5}$$

with $A$ as the macroscopic (geometric) electrode area, $\sigma_{\mathrm{el}}$ and $\sigma_{\mathrm{ion}}$ as the mean electronic and ionic partial conductivities of the SEI, $M_{\mathrm{SEI}}$ as the mean molar mass of the SEI, $\mu_{\mathrm{Li}}^{0}$ as the chemical potential of pure lithium metal, $F$ as the Faraday constant, $\rho_{\mathrm{SEI}}$ as the mean density of the SEI, $x$ as the stoichiometric factor of lithium metal consumption, the time $t$, and $k'$ as the parabolic rate constant of the interphase reaction.[20,90]

Plotting the resistance obtained by impedance spectroscopy against the square root of time yields the parabolic rate constant and the intercept $B$. The intercept is caused by a delay between cell assembly and the start of the measurement. Using these values and approximating the conductivity of the SEI by the conductivity of $Li_2S$, Wenzel et al. calculated the SEI thickness $d$(SEI) for several electrolytes:[20,90]

$$d(\mathrm{SEI}) = \sigma_{ion} \cdot R(\mathrm{SEI}) \cdot A = \sigma_{ion} \cdot \left( B + k' \cdot t^{0.5} \right) \tag{6}$$

Otto et al. chose a different method to characterize interphase formation between lithium metal and different SEs,[26] more closely described in chapter 2.3.2. By combining ToF-SIMS and AFM measurements the layer thickness of the formed SEI in a Li|LPSCl sample was measured for the first time. It is approx. 250 nm thick,[26] which is two orders of magnitude larger than the 2.1 nm layer thickness estimated by Wenzel et al. after 24 h of contact.[20]

Yet another approach was used by Bron et al. to obtain the MCI layer thickness in a Li|LGPS cell.[91] Also using impedance spectroscopy, the layer thickness $d$(MCI) was calculate with the measured capacitance $C$(MCI):[91]

$$d(\mathrm{MCI}) = \frac{\varepsilon_0 \cdot \varepsilon_{\mathrm{r}}}{C(\mathrm{MCI})} \tag{7}$$

With $\varepsilon_0$ as the vacuum permittivity and $\varepsilon_{\mathrm{r}}$ as the relative permittivity of the MCI.[91]

The film thickness obtained by Bron et al. using equation (7) is in the µm range after 24 hours of contact. This is two orders of magnitude higher than the 17 nm calculated by Wenzel et al..[19,91] For the calculation of the SEI layer thickness, Wenzel et al. assumed that the ionic conductivity is close to the conductivity of $Li_2S$, and the electronic conductivity is negligible.[19] However, the electronic and ionic conductivities determined by Bron et al. for the MCI of LGPS are both in the $\mu S \cdot cm^{-1}$ range.[91] This proves that the interphase is indeed a mixed conductor and that the assumptions made by Wenzel et al.,[20] cannot be used for calculating the layer thickness. This shows that the conductivity of the respective layer must be known for the layer thickness determination. Otherwise, large errors may be caused.

Both, Bron's and Otto's results show that the approximation of the ionic conductivity of interphases by that of $Li_2S$ underestimates the actual layer thickness.[19,20,26,91] However, since measurements of

electronic and ionic conductivity have not yet been performed on bulk samples of interphases, further studies must be carried out to better represent their actual properties. Therefore, no interphase thicknesses were calculated in this thesis.

# 3 Results

At the beginning of this dissertation, knowledge of interfacial degradation between solid electrolytes and lithium metal anodes was limited. Due to the high reactivity of lithium, and the difficulties in studying interfaces, few stability studies had been reported in the literature. The objective of this work was to extend the chemical stability investigation to emerging electrolytes, among others, to advance lithium metal solid-state batteries. In addition, the growth kinetics of the interphases were to be investigated, and the influence of the components used to be determined.

## 3.1 Publication 1: "Lithium-Metal Anode Instability of the Superionic Halide Solid Electrolytes and the Implications for Solid-State Batteries"

In Publication 1 of this thesis, the interface stability between halide SEs and lithium metal was investigated and an alternative to the direct contact was explored. *In situ* XPS measurements were performed to elucidate the chemical decomposition. Furthermore, impedance spectroscopy was used to gain insight into the temporal evolution of the interphase reaction and the overall cell resistance.

*In situ* deposition of lithium und subsequent XPS measurements revealed the decomposition reaction of $Li_3MCl_6$ (M = In, Y) in contact with lithium metal. In this process, the (transition) metal ions are reduced to their respective metals, which leads to electronic conductivity in the interphase, causing it to grow continuously. The temporal impedance evolution also shows a fast-growing MCI formation, which increases the overall cell resistance and lowers cell performance. Therefore, halide SEs cannot be used in direct contact with a lithium metal anode. A possible solution to this instability is to implement a protective layer, such as LPSCl, between LMC and the lithium metal anode. Therefore, the LMC|LPSCl interface was additionally characterized by impedance spectroscopy to investigate the suitability of such an interlayer. This revealed a relatively low interfacial impedance, indicating the suitability of such a layered system.

Overall, the publication shows for the first time experimental data on the interfacial stability between halide SEs and lithium metal, and demonstrates the reduction of the respective metal ions during the formation of an MCI. This work illustrates that this class of electrolyte is not suitable for use with a lithium metal anode.

The experiments for this work were designed and planned by the first author under the supervision of W. G. Zeier and J. Janek. R. Schlem synthesized the LMC. The first author performed the XPS and impedance measurements of the Li|LMC|Li cells and analyzed the corresponding data. J. Sann supported the analyses of the XPS data. R. Schlem performed the measurement and analysis of the LPSCl|LMC|LPSCl transfer resistance and supported the first author with the analysis of the temporal impedance evolution of the Li|LMC|Li cells. W. G. Zeier and J. Janek assisted with the scientific discussion of the impedance data, respectively. The manuscript was written by the first author and edited by four co-authors.

Reprinted with permission from Riegger, L. M.; Schlem, R.; Sann, J.; Zeier, W. G.; Janek, J. Lithium-Metal Anode Instability of the Superionic Halide Solid Electrolytes and the Implications for Solid-State Batteries. *Angewandte Chemie International Edition* **2021**, *60* (12), 6718–6723. DOI: 10.1002/anie.202015238. 

GDCh Research Articles Angewandte International Edition Chemie

Solid-State Batteries Hot Paper

How to cite: *Angew. Chem. Int. Ed.* **2021**, *60*, 6718–6723
International Edition: doi.org/10.1002/anie.202015238
German Edition: doi.org/10.1002/ange.202015238

# Lithium-Metal Anode Instability of the Superionic Halide Solid Electrolytes and the Implications for Solid-State Batteries

*Luise M. Riegger, Roman Schlem, Joachim Sann, Wolfgang G. Zeier,* and Jürgen Janek**

***Abstract:*** *Owing to high ionic conductivity and good oxidation stability, halide-based solid electrolytes regain interest for application in solid-state batteries. While stability at the cathode interface seems to be given, the stability against the lithium metal anode has not been explored yet. Herein, the formation of a reaction layer between $Li_3InCl_6$ ($Li_3YCl_6$) and lithium is studied by sputter deposition of lithium metal and subsequent in situ X-ray photoelectron spectroscopy as well as by impedance spectroscopy. The interface is thermodynamically unstable and results in a continuously growing interphase resistance. Additionally, the interface between $Li_3InCl_6$ and $Li_6PS_5Cl$ is characterized by impedance spectroscopy to discern whether a combined use as cathode electrolyte and separator electrolyte, respectively, might enable long-term stable and low impedance operation. In fact, oxidation stable halide-based lithium superionic conductors cannot be used against Li, but may be promising candidates as cathode electrolytes.*

## Introduction

Solid state batteries (SSB) are currently regarded as a possible alternative to conventional lithium ion batteries (LIB) with liquid electrolyte (LE) due to the projected higher energy densities when using a lithium metal anode (LMA).[1–3] When solidifying a battery, the solid electrolyte (SE) replaces the LE and hence requires a high ionic conductivity to achieve reasonable power densities. In addition, stability in contact with cathode active materials (CAM) is needed to prevent detrimental side reactions.[4,5] Currently, most inorganic SSBs employ lithium thiophosphates such as $Li_6PS_5X$ (X = Cl, Br, I) or Argyrodite-type SEs, $Li_3PS_4$ and $Li_{10}GeP_2S_{12}$, all of which are good ionic conductors, but which have severe drawbacks at the cathode due to their inherent instability at high potentials.[2,6]

In order to find SEs that are oxidation stable at high potentials, halides have recently been reconsidered as suitable candidates.[7] In 2018, Asano et al.[8] reevaluated halide SEs with the general composition $Li_3MX_6$ ($M^{3+}$, X = Cl, Br, I), of which mostly $Li_3InCl_6$ and $Li_3YCl_6$ have gained a lot of attention. This group of compounds exhibits a broad range of possible compositions such as for example, $Li_3InCl_6$, $Li_3YCl_6$, $Li_3YBr_6$, $Li_3ErCl_6$ and $Li_3ErI_6$,[8–14] which all show promising ionic conductivities, especially after ball-milling synthesis,[13] and high stability against oxidation that is required for the application in high-voltage SSBs.[11] First cell studies show good stability of the halide SEs in contact with CAMs such as $LiCoO_2$ and $LiNi_{0.8}Co_{0.1}Mn_{0.1}O_2$, and side reactions with the CAMs were not reported.[8–11,15] This is in accordance with theoretical predictions that suggest high oxidation stability of the halide anions.[7,14] According to theoretical predictions, the electrochemical stability windows (ESW) of $Li_3InCl_6$ and $Li_3YCl_6$ are 2.38–4.26 V and 0.62–4.02 vs. $Li^+$/Li, respectively,[14] showing that these electrolytes can be used in contact with most CAMs but that the anode interface may be unstable. Due to the expected instability against the LMA, a lithium thiophosphate separator electrolyte is mostly used, and the halide SEs are primarily used as cathode electrolyte.[8–11] Interestingly, no experimental studies on the interface stability of halide SEs against the LMA have been reported. Figure 1 shows a schematic SSB setup with the halide SE at the LMA, as well as when it is used as the cathode electrolyte only. In addition to the unexplored

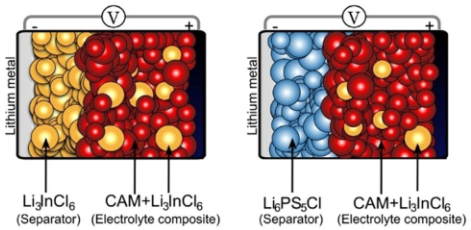


***Figure 1.*** Schematic SSB cell arrangements using $Li_3InCl_6$, a) as both separator electrolyte and cathode electrolyte with the cathode active material (CAM), b) as cathode electrolyte combined with a lithium thiophosphate separator electrolyte towards the lithium metal anode.

[*] L. M. Riegger, Dr. J. Sann, Prof. J. Janek
Institute of Physical Chemistry, Justus-Liebig-University Gießen
Heinrich-Buff-Ring 17, 35392 Giessen (Germany)
and
Center for Materials Research (LaMa), Justus-Liebig-University Gießen
Heinrich-Buff-Ring 17, 35392 Gießen (Germany)
E-mail: juergen.janek@phys.chemie.uni-giessen.de
R. Schlem, Prof. W. G. Zeier
Institute for Inorganic and Analytical Chemistry, University of Münster
Corrensstr. 30, 48149 Münster (Germany)
E-mail: wzeier@uni-münster.de
Supporting information and the ORCID identification number(s) for the author(s) of this article can be found under: https://doi.org/10.1002/anie.202015238.

reactions at the LMA interface, the interface impedance for lithium ion transfer between a lithium thiophosphate separator electrolyte and a halide-based cathode electrolyte has yet not been considered.[16]

To monitor the stability of the halide SEs $Li_3InCl_6$ and $Li_3YCl_6$ against lithium metal, we deposited lithium metal on a SE pellet and performed in situ X-ray photoelectron spectroscopy to analyze the reaction products in detail. Impedance measurements were performed to assess solid electrolyte interphase (SEI) formation between the halide SEs in contact with the LMA, and to quantify the impedance of the interface between the lithium metal halides and the lithium thiophosphate $Li_6PS_5Cl$.

In earlier work, our group investigated decomposition reactions and reaction layers that form when various thiophosphate based electrolytes such as $Li_{10}GeP_2S_{12}$, $Li_3PS_4$ or $Li_6PS_5X$ (X = Cl, Br, I) are exposed to lithium metal, using in situ X-ray photoelectron spectroscopy.[17–20] While all lithium thiophosphates are inherently unstable against lithium metal, the transport properties of the growing interphase decide whether kinetical stability is achieved: (1) If the reaction products form an mixed ion/electron conducting interphase (MCI), then a continuous reaction is expected that will ultimately lead to a short circuit of the SSB over time.[17,21] Mixed conducting interphases are typically observed in SEs that contain metal cations $M^{4+}$ (e.g. M = Ge, Ti), which are then reduced to $M^0$ after contact with lithium forming an electrically conductive reaction layer.[17,18] (2) If the decomposition products are primarily ion-conducting and show negligible electronic conductivity, growth of a stable SEI can occur. As long as the SEI growth is self-limiting and does not add a too high interphase impedance the SE may still be used, like in the case of $Li_3PS_4$ and $Li_6PS_5Cl$.[3,5,20,22]

## Results and Discussion

Figure 2 shows X-ray photoelectron spectra of $Li_3InCl_6$ during deposition, with the In-3d lines, the In-MNN Auger lines as well as the Li-1s lines for pristine $Li_3InCl_6$ after two different lithium deposition times. A pure indium metal reference was used to obtain the shape of the metal In-$3d_{5/2}$ line as well as the position of the characteristic In-MNN line, see Figure S1. In addition, $InCl_3$ was measured as reference to obtain the binding energies of an In-Cl environment. When monitoring the In-3d spectrum, an immediate change in the oxidation state was seen upon lithium deposition. The pristine sample exhibits one line at 446.1 eV, which can be assigned to $Li_3InCl_6$. After ten minutes of lithium deposition two more lines caused by $In_2O_3$ (444.8 eV) and metallic indium (443.7 eV) were found in addition to the original $Li_3InCl_6$. As thermodynamics predicts, $In^{3+}$ is reduced by lithium to form $In^0$. The occurring $In_2O_3$ signal is probably caused by an immediate reaction of the indium metal with oxygen either from a decontamination layer at the surface or with residual oxygen within the chamber. However, the $In_2O_3$ signal increases after a waiting step in the measurement chamber so the influence of residual oxygen seems to be the stronger influence. After an hour of lithium metal deposition (approx. 15 nm), the ongoing decomposition becomes even more apparent. Now the In-3d line of $Li_3InCl_6$ is significantly decreased indicating an ongoing interphase growth that buries the SE. It must be mentioned that $Li_3InCl_6$ and $InCl_3$ exhibit the same binding energy (see Supporting Information Figure S3) and it is not possible to distinguish how much of $Li_3InCl_6$ has potentially reacted to reduced indium chloride species such as $InCl_2$ and InCl.

The formation of metallic indium is also seen in the In-MNN Auger spectrum. At 1081.7 eV a characteristic line is found in $Li_3InCl_6$. Ten minutes of lithium deposition causes

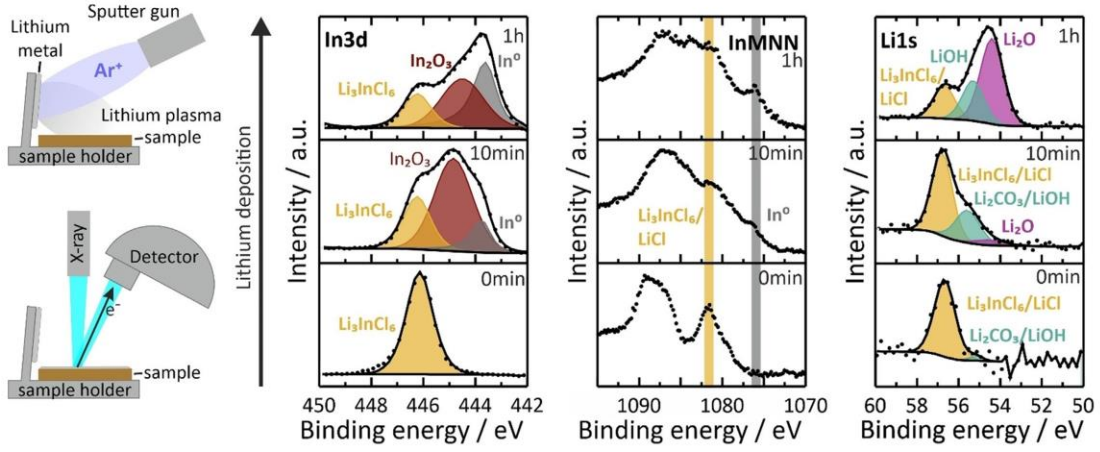


*Figure 2.* a) Schematic illustration of lithium metal deposition on SE with an argon sputter gun and subsequent X-ray photoelectron spectroscopy. X-ray photoelectron In-3d and Li-1 s (b,d) and Auger In-MNN (c) spectra during/after lithium deposition on $Li_3InCl_6$. $Li_3InCl_6$ decomposes in contact with lithium metal to metallic indium, which readily reacts with any remaining oxygen in the UHV chamber to $In_2O_3$. The intensity of lines representing pristine $Li_3InCl_6$ decrease with time indicating coverage of the SE by the growing interphase.

  

a reduction of this $Li_3InCl_6$ signal and a second characteristic peak starts to evolve at 1076.0 eV that is characteristic of In metal (see Supporting Information Figure S1). The In metal signal is even more distinct after an hour of lithium deposition indicating that a significant fraction of the indium has become metallic.

Like in the indium spectra, the decomposition of $Li_3InCl_6$ is seen in the Li-1 s spectrum as well. The Li-1s spectrum shows $Li_3InCl_6$ with a binding energy of 56.7 eV and an additional line at 55.2 eV, which can be assigned to surface contaminations such $Li_2CO_3$ or LiOH. Within ten minutes of lithium deposition, the $Li_3InCl_6$ signal (56.8 eV) is reduced and superimposed by $Li_2CO_3$ and LiOH on the pellet surface. Similar to the In signal, the binding energy of $Li_3InCl_6$ and LiCl is the same, and no distinction can be made in the Li-1s spectrum (see Figure S3). While carbonates can be detected, after ten minutes of lithium deposition, $Li_2O$ is detected at a binding energy of 54.3 eV (Figure S2). After an hour of deposition, the $Li_2O$ signal (54.4 eV) dominates the Li-1s spectrum and the $Li_3InCl_6$/LiCl (56.7 eV) and LiOH (55.3 eV) signals are significantly decreased. The decrease of LiOH can be rationalized either due to a reaction with lithium metal to form $Li_2O$ or by superposition of the $Li_2O$ signal. While lithium metal is constantly deposited on top of the sample, no metallic lithium was detected indicating its quick reaction and ongoing decomposition of the $Li_3InCl_6$ and possible further reactions of Li with the interphase (vide infra).

In addition to $Li_3InCl_6$, the spectra of $Li_3YCl_6$ recorded in situ during lithium deposition can be found in the Figures S4 and S5. Similar to $Li_3InCl_6$, yttrium is reduced upon contact between $Li_3YCl_6$ and lithium as shown in Figure S4. $Y^{3+}$ is reduced to $Y^0$ within ten minutes of lithium deposition and $Y^0$ then reacts further with decontaminations of the antechamber or neighboring species forming $Y_2O_3$ or $Y_2(CO_3)_3$, which results in a broadened XPS signal. Similar to $Li_3InCl_6$, signals of the reduced yttrium components become stronger with time indicating an advancing reaction front. The Li-1s spectra of the $Li_3YCl_6$ show the same behavior as in $Li_3InCl_6$ in which the $Li_3YCl_6$/LiCl signals decrease with deposition time and are being superposed by newly formed $Li_2CO_3$, LiOH and $Li_2O$.

Considering the measured spectra during decomposition with Li metal, we propose the following idealized net reaction:

$$Li_3MCl_6 + 3Li \rightarrow 6LiCl + M^0 \quad (M = In, Y) \tag{1}$$

Of course, intermediate reduced species such as $InCl_2$ and InCl may form as indicated in the Cl-2p spectrum (Supporting Information, Figure S2) by shifting towards the binding energy of $InCl_3$. However, these species cannot be distinguished in the measured spectra. From the thermodynamic perspective, the ongoing reaction will ultimately end at a fully reduced metal species. Clearly, the in situ deposition experiments prove that the halide SEs are unstable against lithium metal, showing a continuously growing reaction layer.

To study SEI growth, time resolved impedance spectroscopy was performed on $Li_3InCl_6$ symmetric cells with lithium metal electrodes. Figure 3 a shows the impedance spectrum of $Li_3InCl_6$ with blocking electrodes to obtain the typical capacitance of bulk $Li_3InCl_6$, which was found to be 20 pF together with an ionic conductivity of 0.5 $mS\,cm^{-1}$. Figure 3 c then shows the collected impedance spectra (15 min intervals at the beginning, then 30 min and later 1 hour intervals). The collected time-resolved spectra were fitted with an equivalent circuit consisting of three parallel *RQ* elements in series (*R*: resistance, *Q*: constant phase element, CPE). Figure 3 b shows an exemplary fit of one impedance spectrum and the capacitances evaluated for the three processes. Bulk conduction within $Li_3InCl_6$ is observed at high frequencies with a capacitance of 84.3 pF (pellet thickness is a quarter of the pellet with the blocking electrodes). A low frequency process is visible that we attribute to the Li | SE (or better Li/SEI) interface as a much higher capacitance of 3.1 μF is observed due to the planar electrodes. In addition, a third process is visible in the intermediate frequency range (0.7 MHz to 4 kHz). The capacitance of this process with 8.4 nF indicates a grain boundary process, likely indicative of the growing interphase. This process, while described via one constant phase element/resistor element, shows low α values of down to 0.65.[23] It is therefore highly likely that multiple underlying processes with quite close relaxation times are occurring, indicating a rather distributed microstructural and compositional nature of the forming interphase.

When extracting the resistances of the different processes (see Figure 3 d), the bulk contribution does not vary significantly with time. The resistance that is assigned to the interphase (cyan) is continuously growing with time, together with the interface resistance (blue) towards Li, and a high overall interfacial resistance of 854 Ω has already formed after one hour. Based on the classification by Wenzel et al.[24] the ongoing growth of the interphase together with the growing resistance is indicative of an SEI in which the ionic conductivity of the interphase is lower than the conductivity of the bulk electrolyte. If Equation (1) applies, the SEI is formed from a composite of indium metal in LiCl.[25] The volume fraction of indium from the decomposition reaction compared to LiCl is relatively small (1:8), and the SEI resistance may be dominated by LiCl. Interestingly enough, the decomposition behavior leading to a mixed-conducting interphase is observed in $Li_3YCl_6$ as shown in the Supporting Information, Figure S6. At this point, the discrepancy between the transport behavior of $Li_3InCl_6$ and $Li_3YCl_6$ may be explained by the fact that indium is prone to alloying with Li already at room temperature.[26] This LiIn alloy formation would form a metal electrode dispersed within LiCl as an electrolyte, which shows the behavior of a SEI development in the impedance measurement.[25] In any case, both $Li_3InCl_6$ and $Li_3YCl_6$ are clearly exhibiting fast decomposition at the LMA and cannot be used as separator electrolyte materials in SSBs.

$Li_3InCl_6$ and $Li_3YCl_6$ have been tested in SSBs as cathode electrolyte components, whereas thiophosphates are often also used as separator electrolyte material.[8–11] In order to employ halide-based SEs as cathode electrolytes in combination with thiophosphate SEs, the transfer resistance at their interface needs to be sufficiently small. In order to study this interfacial resistance a symmetric cell setup was used

  

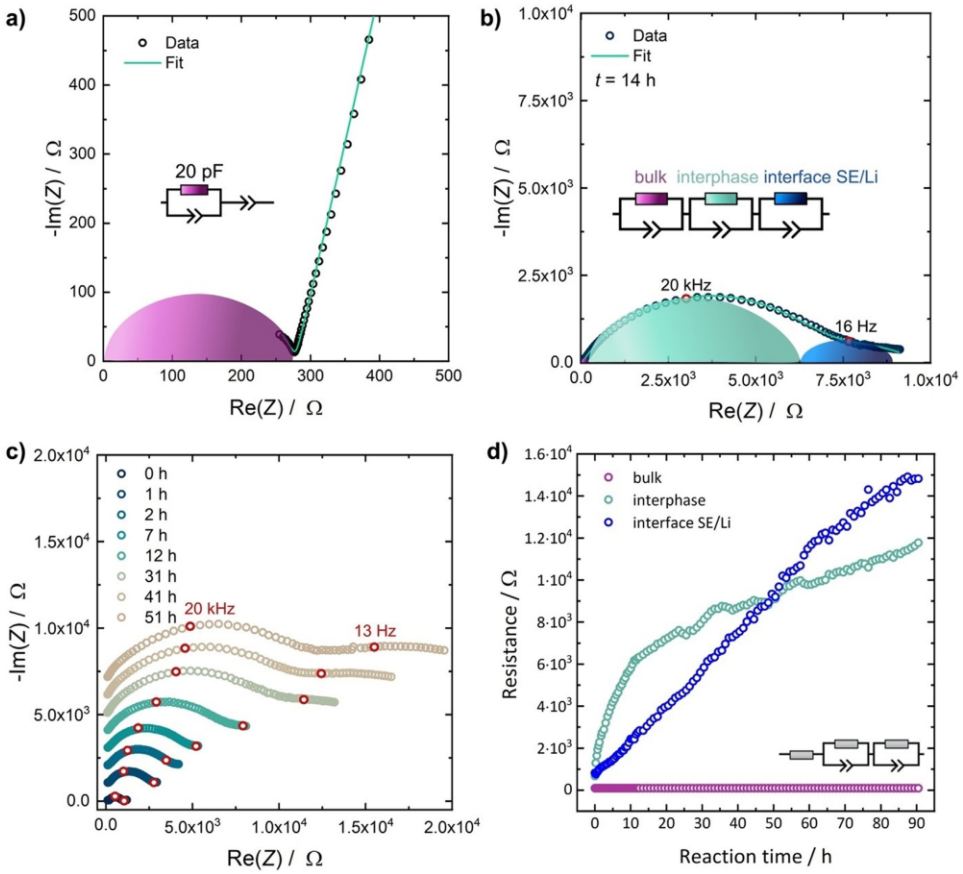


***Figure 3.*** a) Impedance spectra of $Li_3InCl_6$ using blocking electrodes. b) Representative fit of an impedance spectrum of a symmetric cell Li/$Li_3InCl_6$/Li after 14 hours, showing the bulk transport process in $Li_3InCl_6$ (shown in purple), the interface Li/SEI (blue) and the growing resistance of the interphase (cyan). c) Temporal evolution of the impedance response of a symmetric Li | $Li_3InCl_6$ | Li cell, stacked without rescaling and shifted by 1 kΩ for each spectrum. d) Temporal evolution of the resistances of the different processes.

consisting of a $Li_3InCl_6$ pellet sandwiched between a layer of $Li_6PS_5Cl$ with Li electrodes on each side. At room temperature, only one process is visible in the impedance spectrum (see Figure 4a). To resolve the respective ionic transfer process, the impedance was measured at low temperatures down to 173 K. Figure 4a shows a representative Nyquist Plot at 193 K, as well as a schematic of the cell setup and the used equivalent circuit as insets. At these temperatures, a single semi-circle was observed for the bulk contribution, which is indicative for virtually similar fast conduction in both electrolytes and a combined capacitance of 51.8 pF, indicative of a bulk process. A second process is found that corresponds to the $Li_6PS_5Cl$ | $Li_3InCl_6$ interphase with a capacitance of 0.4 μF. The high capacitance rules out that these are grain boundary resistances, as these are expected to have capacitances in the nF range. The deconvolution of both processes provides the respective resistances, which are shown in Figure 4b. A slightly higher activation barrier for the ion transfer between $Li_6PS_5Cl$ and $Li_3InCl_6$ is found compared to bulk transport. Overall the $Li_6PS_5Cl$ | $Li_3InCl_6$ charge transfer resistance is roughly one order of magnitude smaller than the bulk contribution and is 59 Ω cm$^2$ compared to 589 Ω cm$^2$ for the bulk process at 193 K, thus it is negligible at room temperature. This small resistance for Li ion charge transfer at the hetero-contact $Li_6PS_5Cl$ | $Li_3InCl_6$ supports the general finding that the interface resistance two inorganic SEs is small, once good contact is achieved.[16]

## Conclusion

In conclusion, this communication reports firstly on the instability of $Li_3InCl_6$ and $Li_3YCl_6$ at the LMA. Decomposition by reduction is found via in situ X-ray spectroscopy that leads to a fast-growing interphase, which is detrimental for the overall cell resistance. This rules out the use of lithium metal

  

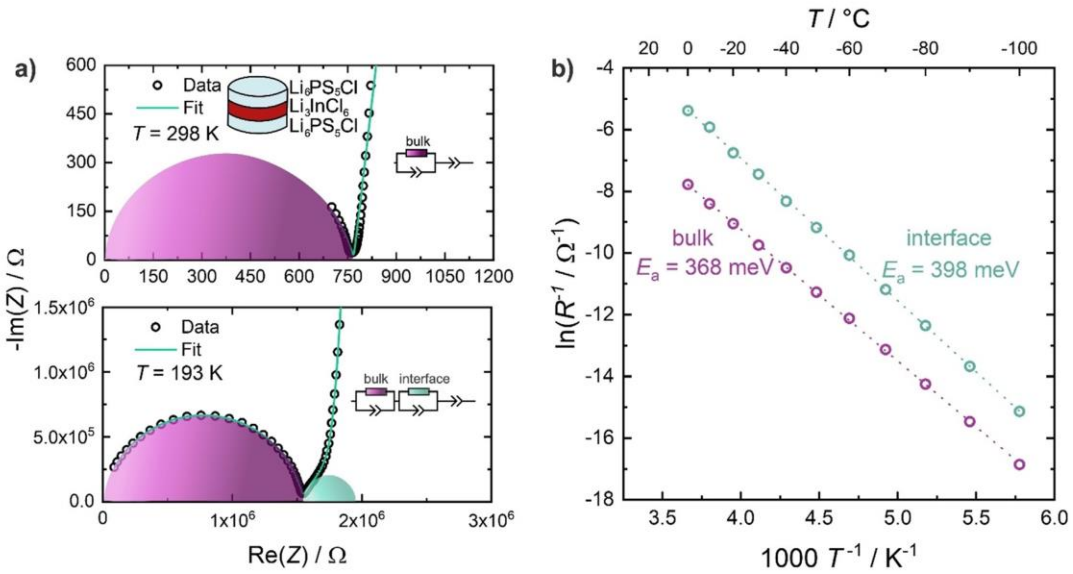


***Figure 4.*** a) Representative impedance of the symmetric $Li_6PS_5Cl\,|\,Li_3InCl_6\,|\,Li_6PS_5Cl$ sandwich cell at room temperature and 193 K. While both processes cannot be deconvoluted at room temperature and are described well with a single bulk process (40 pF) at lower temperatures a clear assignment can be made corresponding to a bulk (51.8 pF) and an interface contribution (0.4 μF). b) Arrhenius behavior of the two processes in the bulk and at the $Li_6PS_5Cl\,|\,Li_3InCl_6$ interface.

halides as separator electrolyte materials in SSBs with LMA. Secondly, a relatively low interface impedance is measured at the (unoptimized) $Li_6PS_5Cl\,|\,Li_3InCl_6$ interface. Thus, the combination of stable SEI-forming $Li_6PS_5Cl$ together with $Li_3InCl_6$ as cathode electrolyte, or the use of the halide SE as a stable coating of an CAM, may be a suitable solution in practice.

## Acknowledgements

The research was supported by the Federal Ministry of Education and Research (BMBF) within the project FESTBATT under grant numbers 03XP0117A and 03XP0176D. We greatly appreciate helpful discussions with S. Burkhardt. Open access funding enabled and organized by Projekt DEAL.

## Conflict of interest

The authors declare no conflict of interest.

**Keywords:** electrochemical energy storage · lithium metal anode · solid electrolyte interphase · solid-state batteries · x-ray photoelectron spectroscopy

[1] a) J. Janek, W. G. Zeier, *Nat. Energy* **2016**, *1*, 1167; b) J. Betz, G. Bieker, P. Meister, T. Placke, M. Winter, R. Schmuch, *Adv. Energy Mater.* **2019**, *9*, 1803170.

[2] Y.-G. Lee, S. Fujiki, C. Jung, N. Suzuki, N. Yashiro, R. Omoda, D.-S. Ko, T. Shiratsuchi, T. Sugimoto, S. Ryu, et al., *Nat. Energy* **2020**, *5*, 299.

[3] S. Randau, D. A. Weber, O. Kötz, R. Koerver, P. Braun, A. Weber, E. Ivers-Tiffée, T. Adermann, J. Kulisch, W. G. Zeier, et al., *Nat. Energy* **2020**, *5*, 259.

[4] a) S. P. Culver, R. Koerver, T. Krauskopf, W. G. Zeier, *Chem. Mater.* **2018**, *30*, 4179; b) S. P. Culver, R. Koerver, W. G. Zeier, J. Janek, *Adv. Energy Mater.* **2019**, *9*, 1900626; c) W. D. Richards, L. J. Miara, Y. Wang, J. C. Kim, G. Ceder, *Chem. Mater.* **2016**, *28*, 266.

[5] R. Koerver, F. Walther, I. Aygün, J. Sann, C. Dietrich, W. G. Zeier, J. Janek, *J. Mater. Chem. A* **2017**, *5*, 22750.

[6] a) F. Walther, R. Koerver, T. Fuchs, S. Ohno, J. Sann, M. Rohnke, W. G. Zeier, J. Janek, *Chem. Mater.* **2019**, *31*, 3745; b) J. Auvergniot, A. Cassel, J.-B. Ledeuil, V. Viallet, V. Seznec, R. Dedryvère, *Chem. Mater.* **2017**, *29*, 3883; c) W. Zhang, D. A. Weber, H. Weigand, T. Arlt, I. Manke, D. Schröder, R. Koerver, T. Leichtweiss, P. Hartmann, W. G. Zeier et al., *ACS Appl. Mater. Interfaces* **2017**, *9*, 17835; d) R. Koerver, I. Aygün, T. Leichtweiß, C. Dietrich, W. Zhang, J. O. Binder, P. Hartmann, W. G. Zeier, J. Janek, *Chem. Mater.* **2017**, *29*, 5574.

[7] S. Muy, J. Voss, R. Schlem, R. Koerver, S. J. Sedlmaier, F. Maglia, P. Lamp, W. G. Zeier, Y. Shao-Horn, *iScience* **2019**, *16*, 270.

[8] T. Asano, A. Sakai, S. Ouchi, M. Sakaida, A. Miyazaki, S. Hasegawa, *Adv. Mater.* **2018**, *30*, 1803075.

[9] X. Li, J. Liang, N. Chen, J. Luo, K. R. Adair, C. Wang, M. N. Banis, T.-K. Sham, L. Zhang, S. Zhao, et al., *Angew. Chem. Int. Ed.* **2019**, *58*, 16427–16432; *Angew. Chem.* **2019**, *131*, 16579–16584.

  

[10] X. Li, J. Liang, J. Luo, M. Norouzi Banis, C. Wang, W. Li, S. Deng, C. Yu, F. Zhao, Y. Hu, et al., *Energy Environ. Sci.* **2019**, *12*, 2665.
[11] K.-H. Park, K. Kaup, A. Assoud, Q. Zhang, X. Wu, L. F. Nazar, *ACS Energy Lett.* **2020**, *5*, 533.
[12] a) X. Li, J. Liang, X. Yang, K. R. Adair, C. Wang, F. Zhao, X. Sun, *Energy Environ. Sci.* **2020**, *13*, 1429; b) R. Schlem, T. Bernges, C. Li, M. A. Kraft, N. Minafra, W. G. Zeier, *ACS Appl. Energy Mater.* **2020**, *3*, 3684.
[13] R. Schlem, S. Muy, N. Prinz, A. Banik, Y. Shao-Horn, M. Zobel, W. G. Zeier, *Adv. Energy Mater.* **2020**, *10*, 1903719.
[14] S. Wang, Q. Bai, A. M. Nolan, Y. Liu, S. Gong, Q. Sun, Y. Mo, *Angew. Chem. Int. Ed.* **2019**, *58*, 8039; *Angew. Chem.* **2019**, *131*, 8123.
[15] a) J. Liang, X. Li, S. Wang, K. R. Adair, W. Li, Y. Zhao, C. Wang, Y. Hu, L. Zhang, S. Zhao, et al., *J. Am. Chem. Soc.* **2020**, *142*, 7012; b) C. Wang, J. Liang, M. Jiang, X. Li, S. Mukherjee, K. Adair, M. Zheng, Y. Zhao, F. Zhao, S. Zhang, et al., *Nano Energy* **2020**, *76*, 105015; c) C. Yu, Y. Li, K. R. Adair, W. Li, K. Goubitz, Y. Zhao, M. J. Willans, M. A. Thijs, C. Wang, F. Zhao, et al., *Nano Energy* **2020**, *77*, 105097.
[16] M. Weiss, F. J. Simon, M. R. Busche, T. Nakamura, D. Schröder, F. H. Richter, J. Janek, *Electrochem. Energy Rev.* **2020**, *3*, 221.
[17] S. Wenzel, T. Leichtweiss, D. Krüger, J. Sann, J. Janek, *Solid State Ionics* **2015**, *278*, 98.
[18] S. Wenzel, S. Randau, T. Leichtweiß, D. A. Weber, J. Sann, W. G. Zeier, J. Janek, *Chem. Mater.* **2016**, *28*, 2400.
[19] S. Wenzel, D. A. Weber, T. Leichtweiss, M. R. Busche, J. Sann, J. Janek, *Solid State Ionics* **2016**, *286*, 24.
[20] S. Wenzel, S. J. Sedlmaier, C. Dietrich, W. G. Zeier, J. Janek, *Solid State Ionics* **2018**, *318*, 102.
[21] P. Hartmann, T. Leichtweiss, M. R. Busche, M. Schneider, M. Reich, J. Sann, P. Adelhelm, J. Janek, *J. Phys. Chem. C* **2013**, *117*, 21064.
[22] a) Z. Liu, A. Borodin, G. Li, X. Liu, Y. Li, F. Endres, *J. Phys. Chem. C* **2020**, *124*, 300; b) S. Boulineau, J.-M. Tarascon, J.-B. Leriche, V. Viallet, *Solid State Ionics* **2013**, *242*, 45; c) S. Wang, Y. Zhang, X. Zhang, T. Liu, Y.-H. Lin, Y. Shen, L. Li, C.-W. Nan, *ACS Appl. Mater. Interfaces* **2018**, *10*, 42279.
[23] G. J. Brug, A. van den Eeden, M. Sluyters-Rehbach, J. H. Sluyters, *J. Electroanal. Chem. Interfacial Electrochem.* **1984**, *176*, 275.
[24] S. Wenzel, T. Leichtweiss, D. A. Weber, J. Sann, W. G. Zeier, J. Janek, *ACS Appl. Mater. Interfaces* **2016**, *8*, 28216.
[25] X. Liang, Q. Pang, I. R. Kochetkov, M. S. Sempere, H. Huang, X. Sun, L. F. Nazar, *Nat. Energy* **2017**, *2*, 17119.
[26] A. L. Santhosha, L. Medenbach, J. R. Buchheim, P. Adelhelm, *Batteries Supercaps* **2019**, *2*, 524.

Manuscript received: November 15, 2020
Accepted manuscript online: December 14, 2020
Version of record online: February 1, 2021

  

## 3.2 Publication 2: "Instability of the $Li_7SiPS_8$ Solid Electrolyte at the Lithium Metal Anode and Interphase Formation"

In Publication 2 of this dissertation, the interfacial stability between LiSiPS and lithium metal was investigated using impedance spectroscopy, *in situ* XPS, ToF-SIMS, XRD and solid-state MAS-NMR. In addition, density functional theory (DFT) calculations and ab initio molecular dynamics (AIMD) simulations were conducted to further elucidate the decomposition reaction.

Temporal impedance measurements were performed to investigate the influence of the interphase formation on the total cell impedance. This showed that LiSiPS and lithium react strongly upon contact, increasing the resistivity by two orders of magnitude. Stripping/plating experiments on Li|LiSiPS|Li cells confirmed the formation of a high-resistance layer and showed rapid overpotential development of the cells. ToF-SIMS profiles of the Li|LiSiPS interface measured after different storage times revealed a continuous interphase growth, confirming the electrochemical measurement results. Thus, this electrolyte cannot be implemented in a cell with an LMA.

To obtain chemical information about the decomposition reaction, *in situ* XPS measurements were performed. Although these proved that the SE readily decomposed upon contact with lithium metal, neither $Si^0$ nor Li-Si signals were measured. To verify the XPS measurements and to clarify which decomposition products cause the MCI formation, MAS-NMR measurements were performed on a reacted Li-LiSiPS sample. This confirmed the XPS results. In addition, the $^{31}P$ spectrum showed an unknown peak that could be caused by phosphidosilicates. These are possibly the cause of a sufficiently high partial electronic conductivity which allows the interphase to grow continuously and distinguishes LiSiPS from other Li-P-S electrolytes.

In addition, DFT calculations and AIMD simulations were conducted to study the interface reaction as well as the interface evolution at different temperatures. The DFT calculations confirmed the instability of LiSiPS in contact with lithium. AIMD simulations revealed that the formed interphase is mostly amorphous and that the $SiS_4^{4-}$ units seem to be more stable than the $PS_4^{3-}$ units.

While LiSiPS could be a promising SE for industrial applications due to its high ionic conductivity, this study unfortunately showed that it is not suitable for applications with direct contact to a lithium metal anode. In addition, it was found that the interphase formed was electronically conductive even though no metal or alloy was formed during decomposition. Therefore, careful testing of the stability of SE containing metal(-loid) ions against lithium metal is generally recommended.

The experiments for this work were designed and planned by the first author under the supervision of F. H. Richter and J. Janek. L. G. Balzat and S. Harm synthesized the material and performed the XRD measurements and Rietveld refinement under supervision of B. V. Lotsch. The first author performed the XPS measurements and analyzed the corresponding data. J. Sann supported the analyses of the XPS data. The first author performed the measurement and data analyses of the temporal impedance evolution of Li|LiSiPS|Li cells. O. Kötz performed the cycling of Li|LiSiPS|Li cells under supervision of the first author who performed the data analyses. S. Burkhardt and F. H Richter assisted with the scientific discussion of the impedance data, respectively. S.-K. Otto performed the ToF-SIMS measurement and analyses. S. Jovanovic and S. Merz performed the NMR characterization and data analyses under supervision of J. Granwehr. B. V. Lotsch assisted with the scientific discussion of the NMR data. M. Sadowski performed the theoretical calculations under supervision of K. Albe. The manuscript was written through contributions of the first author (abstract, introduction, electrochemical characterization, XPS characterization, and conclusions), S. Harm (material synthesis), S.-K. Otto (ToF-SIMS characterization), S. Jovanovic and S. Merz (NMR characterization) and M. Sadowski (theoretical calculations). The manuscript was edited by thirteen co-authors.

CHEMISTRY OF MATERIALS

pubs.acs.org/cm Article

# Instability of the $Li_7SiPS_8$ Solid Electrolyte at the Lithium Metal Anode and Interphase Formation

Luise M. Riegger, Svenja-K. Otto, Marcel Sadowski, Sven Jovanovic, Olaf Kötz, Sascha Harm, Lucas G. Balzat, Steffen Merz, Simon Burkhardt, Felix H. Richter, Joachim Sann, Rüdiger-A. Eichel, Bettina V. Lotsch, Josef Granwehr, Karsten Albe, and Jürgen Janek*

Cite This: *Chem. Mater.* 2022, 34, 3659–3669 Read Online

ACCESS | Metrics & More | Article Recommendations | Supporting Information

**ABSTRACT:** Thiophosphate solid electrolytes containing metalloid ions such as silicon or germanium show a very high lithium-ion conductivity and the potential to enable solid-state batteries (SSBs). While the lithium metal anode (LMA) is necessary to achieve specific energies competitive with liquid lithium-ion batteries (LIBs), it is also well known that most of the metalloid ions used in promising thiophosphate solid electrolytes are reduced in contact with an LMA. This reduction reaction and its products formed at the solid electrolyteLMA interface can compromise the performance of an SSB due to impedance growth. To study the reduction of these metalloid ions and their impact more closely, we used the recently synthesized $Li_7SiPS_8$ as a member of the tetragonal $Li_{10}GeP_2S_{12}$ (LGPS) family. Stripping/plating experiments and the temporal evolution of the impedance of symmetric Li|$Li_7SiPS_8$|Li transference cells show a severe increase in cell resistance. We characterize the reduction of $Li_7SiPS_8$ after lithium deposition with in situ X-ray photoelectron spectroscopy, time-of-flight secondary-ion mass spectrometry, and solid-state nuclear magnetic resonance spectroscopy. The results indicate a continuous reaction without the formation of elemental silicon. For elucidating the reaction pathways, density functional theory calculations are conducted followed by ab initio molecular dynamics simulations to study the interface evolution at finite temperature. The resulting electronic density of states confirms that no elemental silicon is formed during the decomposition. Our study reveals that $Li_7SiPS_8$ cannot be used in direct contact with the LMA, even though it is a promising candidate as both a separator and a catholyte material in SSBs.

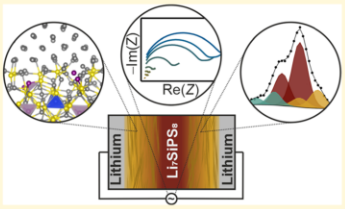


## INTRODUCTION

The increasing demand for improved electrochemical energy storage devices calls for solid-state batteries (SSBs) as these promise safer device applications due to their nonflammable components and a wider operation temperature range.[1,2] An important key-performance indicator for high-power applications such as electric vehicles is the high ionic conductivity of the solid electrolyte (SE).[3] Since the first publication in 2011 by Mitsui and co-workers,[4] thiophosphate solid electrolytes such as $Li_{10}GeP_2S_{12}$ (LGPS),[4−6] $Li_{10}Sn_2P_2S_{12}$,[7,8] as well as $Li_{10}SiP_2S_{12}$[9,10] and $Li_{11}Si_2PS_{12}$[11] have been developed reaching ionic conductivities in the order of 10 mS $cm^{-1}$. Another member of this family is the superionic conductor $Li_7SiPS_8$, which was recently synthesized in the tetragonal (t-$Li_7SiPS_8$) and orthorhombic (o-$Li_7SiPS_8$) phase by Harm et al.[12]

The here-studied t-$Li_7SiPS_8$ polymorph is isotypic to tetragonal $Li_7GePS_8$ and crystallizes in the space group $P4_2/nmc$ (no. 137) with mixed occupancy by $PS_4^{3-}/SiS_4^{4-}$ tetrahedra at the 4d site and no Si occupation at the 2b site. The total Li conductivity of t-$Li_7SiPS_8$ is about 2 mS $cm^{-1}$, which has been rationalized by the glassy (ceramic) nature of this material.[12]

For further improving the gravimetric energy density of SSBs, both high-voltage cathode materials and high-capacity anode materials such as the lithium metal should be employed.[2] Unfortunately, most SEs are inherently unstable against the low potential of the lithium metal anode (LMA) and form a decomposition layer upon contact.[1,2,13,14] Thus, the compatibility between the SE and an LMA as well as the impact of potentially forming interphases on the cell performance require closer inspection.

The electrochemical stability window of an SE provides information about its stability toward the electrode-active materials and indicates the electrode potentials at which the oxidation state of individual components in the SE changes. Theoretical (thermodynamic) stability windows have been calculated for a range of SEs including $\beta$-$Li_3PS_4$ (LPS), $Li_6PS_5Cl$ (LPSCl), and LGPS using density functional theory (DFT) calculations to determine which phases are thermodynamically most stable.[15−18] These studies found that thiophosphate SEs decompose already at a potential of 1.71

Received: December 15, 2021
Revised: March 25, 2022
Published: April 11, 2022





https://doi.org/10.1021/acs.chemmater.1c04302
*Chem. Mater.* 2022, 34, 3659−3669

V vs $Li^+/Li$ due to the reduction of $P^{5+}$ ions to $P^0$. Upon decreasing the potential further, $P^0$ is reduced forming various Li−P phases until $Li_3P$ is formed at 0.87 V vs $Li^+/Li$.[15−19] If the SE does not contain phosphorus, the stability window is shifted to different reduction potentials.[17,20] The reduction of $Li_4GeS_4$ or $Li_4SiS_4$, for example, starts at 1.65 V or 1.38 V vs $Li^+/Li$, respectively, indicating that the $GeS_4^{4-}$ and $SiS_4^{4-}$ tetrahedra are more stable against reduction than the $PS_4^{3-}$ anions. The reduction of the anions is accompanied by the formation of $Li_2S$ in all electrolytes.[15−20] The t-$Li_7SiPS_8$ studied in this paper can be considered a solid solution of $Li_3PS_4$ and $Li_4SiS_4$. It contains two complex anions with slightly different reduction potentials. Thus, the reduction of the $P^{5+}$ ions in the $PS_4$ tetrahedra is expected to occur before the $Si^{4+}$ ions are reduced to $Si^0$.

Experimental studies by Schwietert et al. measuring the practical reduction stability show that LPSCl is reduced to $P^0$, $Li_2S$, and LiCl at 1.08 V vs $Li^+/Li$ via the intermediate $Li_{11}PS_5Cl$ followed by the formation of $Li_3P$, $Li_2S$, and LiCl at 0.8 V vs $Li^+/Li$.[21] Similar results are found by Ohno et al.[22] In their study, the reduction of LPSCl starts at 0.8 V vs In/LiIn (1.42 V vs $Li^+/Li$). Upon decreasing the potential further, this reduction is followed by a decomposition at 0.6 V vs In/LiIn (1.22 V vs $Li^+/Li$), which was assigned to the reduction of $P^{5+}$ in $PS_4^{3-}$ tetrahedra.[22] The onset of germanium metal formation in LGPS starts between 0.9 and 0.5 V vs $Li^+/Li$.[23] The difference between theoretical (thermodynamic) and practical (electrochemical) stability windows is assumed to be linked to reaction kinetics not considered in the theoretical calculations.[21]

No practical stability windows have yet been reported for SEs containing silicon. While $PS_4^{3-}$ is always reduced at 1.71 V vs $Li^+/Li$ in theoretical calculations independent of the SE it is contained in,[15−19] it is reasonable to assume that the onset of reduction of $SiS_4^{4-}$ is independent of the SEs and starts at lower potentials than for the $PS_4^{3-}$ or $GeS_4^{4-}$ ion, as predicted in theoretical works.[17,20]

Generally, $Li_3P$ and $Li_2S$ are formed during the reduction of a ternary Li−P−S compound.[24−27] In 2016, Wenzel et al. characterized the decomposition of LGPS by in situ X-ray photoelectron spectroscopy (XPS) as well as impedance spectroscopy revealing that a germanium−lithium phase or elemental germanium are formed upon contact with lithium.[28] Other SEs such as thiophosphate-based materials, like $Li_6PS_5X$ (X = Cl, Br, and I) or halide-based electrolytes like $Li_3XCl_6$ (X = In and Y), have been studied by this method as well.[24,25,29,30] The decomposition reaction between an SE and the lithium metal leads to the formation of an interphase. According to Wenzel et al. these interphases are typically distinguished based on their partial electronic conductivity:[29] (1) If the interphase has negligible partial electronic conductivity and is mainly ion-conducting, a stable "solid electrolyte interphase" (SEI) is formed. If the ionic resistance of such an SEI is low, the SE can be used in combination with an LMA, without any measures to avoid the decomposition reaction. (2) If the partial electronic conductivity of the interphase is not negligible due to the formation of sufficiently electron-conducting compounds such as $Ge^0$, $In^0$, or $Y^0$, a "mixed-conducting interphase" (MCI) is formed. Due to its capability to transfer electrons reasonably well, the decomposition reaction will proceed and the MCI grows continuously until either the SE or the LMA is depleted.[17,28,30,31] Otto et al. recently reported on another technique to characterize the interphase and distinguish between the SEI and the MCI.[32] In this method, lithium is deposited on top of the SE and the formed interphase is investigated with time-of-flight secondary-ion mass spectrometry (ToF-SIMS). Depending on the nature of the interphase, depth profiles through the deposited lithium layer and across the lithium|SE interface show distinct features and allow the differentiation between the SEI and the MCI.[32]

Since neither the practical electrochemical stability window of silicon-containing SEs nor the general mechanism in contact with lithium are known, the applicability of highly conductive t-$Li_7SiPS_8$ is unclear. As the conductivity of pure $Li_4SiS_4$ is approximately five orders of magnitude lower than that of t-$Li_7SiPS_8$, $Li_4SiS_4$ is not a suitable SE.[12,33] Therefore, only the stability of t-$Li_7SiPS_8$ in contact with lithium metal is assessed in this study. Stripping/plating experiments and time-resolved impedance spectroscopy were employed to evaluate the evolution of a symmetric Li|t-$Li_7SiPS_8$|Li cell with time as well as the resistance of the formed interphase. To characterize the interphase, lithium was deposited on a t-$Li_7SiPS_8$ pellet and the reactants were monitored subsequently with in situ XPS as well as ToF-SIMS. The decomposition products were analyzed using solid-state nuclear magnetic resonance (NMR) spectroscopy to gain additional insights into the formed products and to verify possible reaction pathways derived from ab initio molecular dynamics (AIMD) simulations.

## EXPERIMENTAL SECTION

**Synthesis and Structural Characterization.** Tetragonal $Li_7SiPS_8$ (t-$Li_7SiPS_8$) was prepared by mixing $Li_2S$ (Sigma-Aldrich, 99.98%), Si (Alfa Aesar, 99.999%), red P (Merck, 99%), and S (sublimed in vacuo) in stoichiometric amounts with an additional 5 wt % excess of sulfur to ensure an oxidizing atmosphere during synthesis. The mixture was ball-milled in 10 g batches in an airtight 50 mL $ZrO_2$ jar using 10 $ZrO_2$ balls (10 mm diameter) for 24 h at 500 rpm (5 min milling, 1 min pause) in a Retsch PM 200 ball mill. The resulting mixture was filled in glassy carbon crucibles, sealed in quartz glass ampoules under vacuum ($<10^{-2}$ mbar), subsequently heated to 525 °C in a tube furnace with a heating rate of 50 °C $h^{-1}$, and held at this temperature for 100 h. After the end of the annealing program, the furnace was switched off and the samples were left in the furnace to slowly cool down to room temperature. The resulting microcrystalline powders are slightly yellow and moisture-sensitive. Therefore, all procedures were conducted in an argon-filled glovebox by M. Braun Inertgas-Systeme GmbH ($p(O_2)/p < 5$ ppm, $p(H_2O)/p < 5$ ppm) or in argon-filled sealed containers.

Powder X-ray diffraction (PXRD) experiments were carried out using a Stoe STADI P diffractometer (Cu $K\alpha_1$ radiation, Ge-(111) monochromator, Mythen 1 K detector) in Debye−Scherrer geometry. All samples were sealed in glass capillaries with a diameter of 0.3 mm under an argon atmosphere. All samples were measured over eight ranges between 5.00° and 60.68° for a total of 13 h. The intensities of the obtained ranges were then added together to obtain a better signal−noise ratio. Rietveld refinements of the obtained PXRD patterns have been carried out with the program Topas 6.[34] The Rietveld refinements of the materials used for this work can be found in the Supporting Information Figures S1 and S2 as well as Tables S1 and S2.

**Electrochemical Characterization.** Symmetrical Li|t-$Li_7SiPS_8$|Li cells were assembled to investigate the reduction stability. The samples were prepared in an M. Braun glovebox ($p(O_2)/p < 5$ ppm, $p(H_2O)/p < 5$ ppm) and measurements were carried out at 25 °C using a VMP300 potentiostat (BioLogic).

For measuring the stripping/plating behavior of t-$Li_7SiPS_8$, lithium foil was fabricated by pressing a piece of fresh lithium (Albermarle Corp.) between two sheets of pouch cell foil to obtain a thickness between 60 and 80 $\mu$m. Afterward, a disk with 6 mm diameter was punched out and applied with 8.5 MPa to an 80 mg of t-$Li_7SiPS_8$



https://doi.org/10.1021/acs.chemmater.1c04302
Chem. Mater. 2022, 34, 3659−3669

pellet (10 mm diameter, 0.07 mm thickness, uniaxially pressed with 3 tons for 30 s). Lilt-$Li_7SiPS_8$|Li cells were cycled using a current density of 0.1 or 1 mA·cm$^{-2}$ for 1 h, respectively. Current densities were calculated using the geometric area of the lithium electrode with a diameter of 6 mm before application of pressure. Impedance measurements with an amplitude of 10 mV were conducted between 3 MHz and 1 Hz before the cycling started and after each stripping or plating step. Before each impedance experiment, the cell was equilibrated for 30 min.

For measuring the temporal evolution of the impedance of Lilt-$Li_7SiPS_8$|Li cells, a pellet with 100 mg of t-$Li_7SiPS_8$ was pressed at 3 tons for 30 s. Lithium foil (Honjo Metal) with a diameter of 9 mm and a thickness of 40 $\mu$m was then brought into contact at both pellet sides. The impedance measurement was carried out at frequencies starting from 7 MHz to 1 Hz with an amplitude of 5 mV. For data evaluation, frequencies between 2 MHz and 1 Hz were used to exclude possible influences of the measurement setup. A constant pressure of 6.4 MPa was applied during the impedance measurement.

**In Situ XPS Characterization.** XPS measurements were conducted using a PHI 5000 VersaProbe II Scanning ESCA Microprobe (Physical Electronics) with a monochromated Al $K_\alpha$ X-ray source (beam diameter: 200 $\mu$m, X-ray power: 50 W). A step time of 50 ms, a step size of 0.2 eV, and an analyzer pass energy of 46.95 eV were used for measuring the detailed spectra. The sample surface was charge-neutralized with slow electrons and argon ions; the pressure was ranging from $10^{-7}$ to $10^{-6}$ Pa during the measurement. To sputter the lithium metal, an unscanned argon-ion beam with an acceleration voltage of 2 kV and an argon-ion current of 2.5 $\mu$A was used. For a detailed description of the measurement setup, the authors refer to Wenzel et al.[29] Lithium metal foil (Rockwood Lithium) was cleaned mechanically by scraping with a doctor blade and used as a target. The samples were prepared in a glovebox (M. Braun Inertgas-Systeme GmbH, ($p(O_2)/p$ < 5 ppm, $p(H_2O)/p$ < 5 ppm)) and transferred from the glovebox to the analysis chamber via a transfer shuttle. Data analysis was performed using CasaXPS software and the charge correction was done using the $PS_4^{3-}$ signals in the S 2p (161.8 eV) and P 2p (131.2 eV) spectra.

**In Situ ToF-SIMS.** For lithium deposition, pieces of a lithium rod (99.8%, abcr GmbH) were placed in a crucible of a NTEZ low temperature effusion cell (MBE Components). A crucible temperature of 450 °C resulted in a lithium layer thickness of 1 $\mu$m after 10 min of deposition time. The chamber for lithium deposition is directly attached to the main chamber of the ToF-SIMS instrument, which was used for depth profiling (ToF-SIMS 5, IONTOF GmbH). The instrument is equipped with a 25 kV Bi cluster primary-ion gun for analysis and a dual-source column (DSC) for $Cs^+$ depth profiling. Depth profiles were measured in spectrometry mode (bunched, about 40,000 cts/s, FWHM $m/\Delta m$ = 5000@$m/z$ = 17.00 ($OH^-$)) with $Cs^+$ (300 × 300 $\mu m^2$, 2 kV, 130 nA) as sputter species and $Bi^+$ (1.2 pA, 100 × 100 $\mu m^2$) as primary ions. Between 25 s sputter steps with 2 s pause time, five frames were analyzed with two shots/frame/pixel and 128 × 128 pixels in random raster mode. In all measurements, the cycle time was 100 $\mu$s and negative polarity was used. Data were evaluated with SurfaceLab 7.2 (IONTOF GmbH). Spectra were calibrated using the signals of $^6Li^-$, $Si^-$, $LiS_2^-$, $LiS_3^-$, and $LiS_4^-$. Signals are assigned based on the elements contained in the sample and the smallest deviation to the potential fragments. The samples were electrically isolated from the sample holder and measured with electron neutralization by a flood gun.

**Solid-State NMR Spectroscopy.** For further characterization of the decomposition products, 150 mg of t-$Li_7SiPS_8$ powder was mixed with excess liquid lithium (0.038 g, Honjo Metal) at 250 °C in order to achieve complete reduction of the SE (Rietveld refinement see Supporting Information Figure S3 and Table S3). A $ZrO_2$ magic-angle-spinning (MAS) rotor with a 3.2 mm outer diameter was filled with the reacted t-$Li_7SiPS_8$ powder, ensuring a homogeneous sample distribution. The rotor was closed airtight. All sample preparation steps were carried out in a glovebox by M. Braun ($p(O_2)/p$ < 5 ppm, $p(H_2O)/p$ < 5 ppm).

$^7Li$, $^{29}Si$, and $^{31}P$ MAS NMR spectra of the reacted mixture were obtained using a Bruker Avance III HD spectrometer with a 14.1 T magnet and a 3.2 mm MAS probe (PH MASDVT 600 W2 BL3.2 X/Y/H). The spinning rate was set to 24 kHz, and 90° pulse lengths and powers as well as repetition times for each nucleus are given in Table 1. The $^{29}Si$ and $^{31}P$ spectra were referenced to the t-$Li_7SiPS_8$ NMR measurements by Harm et al.,[12] and the $^7Li$ spectrum was referenced to $Li_4Ti_5O_{12}$ (LTO).[35]

**Table 1. List of NMR Parameters**

| nucleus | $^7Li$ | $^{29}Si$ | $^{31}P$ |
|---|---|---|---|
| 90° pulse length/$\mu$s | 4.0 | 1.5 | 3.0 |
| 90° pulse power/W | 100 | 80 | 80 |
| repetition time/s | 1.0 | 1.0 | 1.0 |

**DFT Calculations.** The Vienna Ab initio Simulation Package (VASP)[36−39] was used to perform DFT calculations using projector augmented wave (PAW) pseudopotentials[40,41] and the exchange-correlation functional parametrized by Perdew−Burke−Ernzerhof (PBE)[42−44] within the generalized gradient approximation (GGA). Owing to its partial occupancies, an initial structure for t-$Li_7SiPS_8$ was generated based on the supercell program.[45] A 2 × 2 × 1 supercell was set up with Si and P atoms randomly distributed while the Li sites were partially occupied. The site occupation of Li ions was split into two parts. First, the Li2 and Li4 sites were simultaneously occupied while keeping the Li3 sites at fixed occupancies and every pair of Li1 sites, located close to each other, was merged into one single Li site located at their midpoint. The model with the lowest electrostatic energy was then used to occupy the remaining Li3 sites. The atomic positions and cell geometry of the structure with the lowest electrostatic energy were optimized using static DFT calculations with an energy cutoff for the plane-wave basis set of 600 eV, a $k$-spacing of 0.25 Å$^{-1}$, and a convergence criterion for the electronic optimization and the atomic forces of $10^{-6}$ eV and $10^{-2}$ eV Å$^{-1}$, respectively.

An interface model with the Li metal was constructed based on the optimized structure. A slab of the t-$Li_7SiPS_8$ structure (12 formula units) with exposed (001) surfaces was prepared without the breaking of $PS_4^{3-}$ or $SiS_4^{4-}$ units, with a remaining surface roughness of the t-$Li_7SiPS_8$. The Li metal slab (150 Li atoms) was prepared likewise with exposed (001) surfaces, and the in-plane lattice constants were adopted to the t-$Li_7SiPS_8$ slab. A vacuum layer was added to both slabs and they were relaxed with a fixed in-plane lattice constant.

The two slabs (354 atoms in total) were then contacted using two different slab separation distances, structurally optimized, and the interface reactions were monitored. Since the defined convergence criteria were not reached after approximately 500 ionic optimization steps, the structures were subjected to AIMD simulations at 300, 500, and 700 K to monitor the evolution of the interface at a finite temperature. The AIMD simulations were performed in the canonical ensemble (NVT), treating only the gamma point. The default cutoff of the pseudopotentials of approximately 500 eV, time steps of 1 fs, and an electronic convergence criterion of $10^{-5}$ eV were used.

Snapshots structures were extracted from the AIMD simulations every picosecond and the atomic positions were optimized relying on the settings described above until forces fell below $2{\cdot}10^{-2}$ eV Å$^{-1}$. Afterward, a non-self-consistent calculation with an increased $k$-point density ($k$-spacing of 0.125 Å$^{-1}$) was performed to obtain an accurate electronic density of states (eDOS) used for the identification of reaction phases. The eDOS of potential reaction phases was obtained similarly, and their initial structure models were taken from the literature.

## ■ RESULTS AND DISCUSSION

An SE can be used in different cell components of an SSB imposing different requirements that have to be fulfilled. For its use as a separator, it needs to ensure a sufficiently low area-



https://doi.org/10.1021/acs.chemmater.1c04302
Chem. Mater. 2022, 34, 3659−3669

specific resistance (ASR) and to prevent short-circuiting under various operation and storage conditions, in particular if an LMA is used. The ASR is determined by the SE's ionic conductivity, its thickness, the size of its interfacial area toward the active materials, and the interfacial contact resistance. In a lithium metal SSB, the separator is in direct contact with the reactive lithium metal, which often leads to the interphase formation already discussed. As this can severely affect the ASR, SE separators are often characterized in terms of their performance in symmetric cells with two lithium electrodes on each side.

Probing their capability of both avoiding a short-circuit as well as a too high ASR, the reversible stripping and plating of lithium through t-$Li_7SiPS_8$ separators was tested using symmetric Lilt-$Li_7SiPS_8$|Li cells under various current densities (Figure 1). A current density of 0.1 mA $cm^{-2}$ causes a

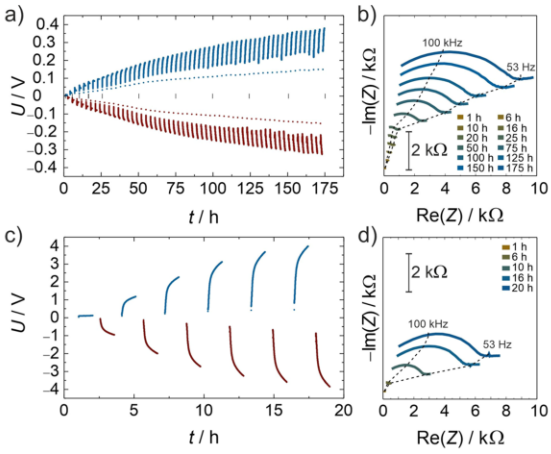


**Figure 1.** Overpotential of Lilt-$Li_7SiPS_8$|Li cells during alternating stripping and plating with a current density of (a) 0.1 mA $cm^{-2}$ and (c) 1 mA $cm^{-2}$, respectively. Between each stripping and plating step, an impedance measurement was conducted to monitor the evolution of the cell impedance during stripping and plating at the corresponding current density (b and d).

continuously increasing overpotential to 0.38 V within 175 h (Figure 1a). This increase is accompanied by a continuous increase of the overall cell impedance (see Figure 1b) measured between each stripping and plating phase. An enlarged Nyquist plot of the first measurements is shown in Figure S4. The cell impedance rises significantly from 94 Ω to 9.8 kΩ within 175 h indicating the formation of a highly resistive layer between the LMA and the SE. In addition to the cell impedance, the overpotential increases simultaneously by two orders of magnitude (Figure 1a). The overpotential is caused by the formation of an interphase layer with a lower conductivity compared to t-$Li_7SiPS_8$. Thus, the potential of the cell rises with the increasing cell impedance. As the interphase expands with time, the overpotential also increases.

If a higher current density of 1 mA $cm^{-2}$ is applied, the cell voltage increases quickly (Figure 1c). Due to the increased $Li^+$ migration, the decomposition reaction also increases and the overpotential reached 4.0 V after 17.5 h. Additionally, pores may be formed at the lithium metal interface as the lithium vacancy diffusion is slower compared to the $Li^+$ diffusion in the SE,[46] reducing the load-bearing contact area and constricting the pathways across the interface. The fast increase in overpotential demonstrates that the application of a t-$Li_7SiPS_8$ separator requires further improvements to achieve reasonable performance for such current densities. The cell impedance increases from 138 Ω to 7.0 kΩ within 18 h (Figure 1d).

It is difficult to explain the impedance/overpotential increase in the data presented in Figure 1, as a distinction between the formation of a more resistive interphase or loss of contact (formation of pores) is difficult. It will be shown in the following section that the interphase formation due to a chemical reaction between t-$Li_7SiPS_8$ and the lithium metal considerably contributes to the observed impedance increase in the present case.

To distinguish the formation of a resistive interphase from the loss of contact, as well as to distinguish between different types of interphases, the cell impedance of a symmetric cell as a function of time (at zero current) has been studied, see Figure 2. The kinetics of interphase formation in symmetric Lilt-$Li_7SiPS_8$|Li cells were investigated by measuring the cell impedance at different times, starting with time intervals of 15 min, later 30 min intervals, and finally 1 h intervals. The impedance data of the cells (Figure 2a) show an increasing cell

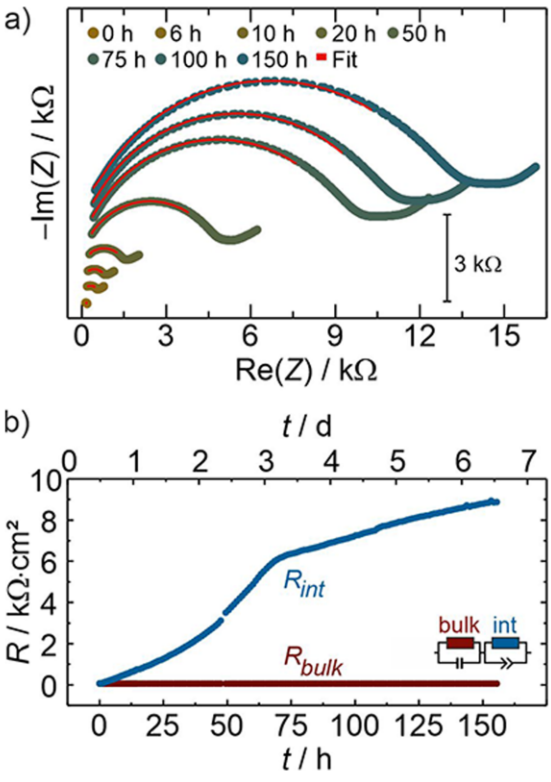


**Figure 2.** (a) Temporal evolution of the cell impedance of a symmetric Lilt-$Li_7SiPS_8$|Li cell. The red line shows the results of a fitting process using a series of two parallel circuits $R_{bulk}$-$C_{bulk}$ and a $R_{int}$-$CPE_{int}$ (constant phase element) to describe the impedance of the bulk and the forming interphase, respectively. (b) Temporal evolution of the bulk ionic resistance $R_{bulk}$ (red) of the SE and the ionic resistance $R_{int}$ of the forming interphase (blue) according to the shown equivalent circuit.



https://doi.org/10.1021/acs.chemmater.1c04302
Chem. Mater. 2022, 34, 3659−3669

impedance reaching approximately 12.5 kΩ after 160 h of contact. An enlarged Nyquist plot of the first measurements is shown in Supporting Information Figure S5. The data were fitted with an equivalent circuit resembling the different charge transport processes expected to contribute to the measured impedance (see Figure 2b). These processes are the transport process in the bulk of the SE and the transport process in the interphase. The transport process in the bulk is described by a parallel *R-C* element describing the bulk resistance $R_{bulk}$ as well as the geometric capacitance. A parallel $R_{int}$-$CPE_{int}$ (constant phase element) was used to describe the impedance of the forming interphase. Bulk- and interphase-related elements are connected in series.

The resistances $R_{bulk}$ and $R_{int}$ are determined as a function of time by fitting the impedance of the equivalent circuit to the measured impedance of the symmetric cells (see Figure 2b). The capacitances can be found in Supporting Information Figure S6. The bulk capacitance $C_{bulk}$ slightly increases over time. The interphase capacitance $C_{int}$, on the other hand, decreases in the beginning of the experiment and increases again after approx. 60 h. The reason for this change could be the superposition of changes in the interface area, interphase thickness, the relative permittivity of the evolving interphase, as well as current constrictions due to pores at the interface or in the MCI. The superimposition could also be seen in the alpha value obtained with the CPE-model, as it was low with a value of approximately 0.7. Thus, a precise calculation of $C_{int}$ is difficult and only a qualitative statement of the evolution of $C_{int}$ is possible. The bulk resistance of the SE $R_{bulk}$ was calculated using the conductivity of the material (1 mS $cm^{-1}$), as only a small part of this process' characteristic frequencies can be measured at room temperature. As the resistance change of the bulk material after reaction with lithium is negligible, see Table S4, $R_{bulk}$ was kept constant during the fitting process. In contrast, the interphase resistance rapidly increases directly after contacting the SE and the LMA, with accelerated growth observed during the first 65 h. The reason for this acceleration is unknown. However, after approximately 70 h of contact time, the temporal evolution of the interphase resistance changes to a square root time dependence ($t^{0.5}$, see Figure S7 and Table S5), indicating a change toward a diffusion-controlled layer growth that can be described using Wagner's model.[24,28,47]

The high impedance is apparently caused by the formation of an MCI and indicates a significantly lower conductivity of the MCI compared to the bulk conductivity of the SE. This may be caused by the high volume fraction of poorly conductive $Li_2S$ formed in the interphase, as will be discussed later.

To better understand the reduction of t-$Li_7SiPS_8$ and the MCI formation, in situ XPS and ToF-SIMS measurements as well as solid-state NMR studies were conducted, see Figures 3–5.

For studying the interphase formation, lithium was deposited on a t-$Li_7SiPS_8$ pellet and XPS spectra were measured subsequently. The normalized detail spectra of S 2p, P 2p, and Si 2p of the pristine sample as well as after 15 min and 2 h of lithium deposition are depicted in Figure 3. The spectra of the pristine sample have peaks assigned to $PS_4^{3-}$/$SiS_4^{4-}$ (red) of the bulk material at 161.8 eV in the S 2p spectrum, 132.3 eV in the P 2p spectrum, and 101.2 eV in the Si 2p spectrum. The peak at 163.5 eV in the S 2p spectrum can be attributed to P–$[S]_n$–P-type anions[48–50] (green) such as

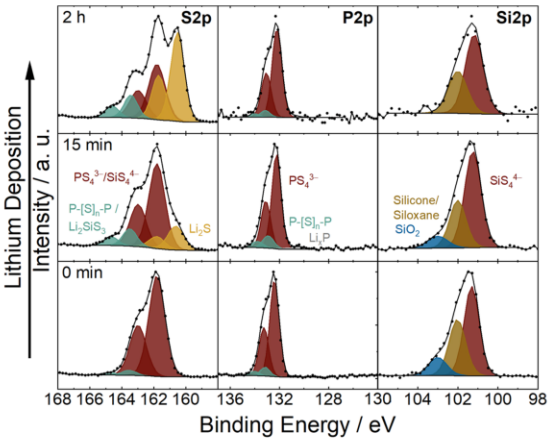


**Figure 3.** Li deposition on a t-$Li_7SiPS_8$ pellet and subsequent in situ XPS measurements of the normalized S 2p, P 2p, and Si 2p spectra for a pristine sample, after 15 min and 2 h of Li deposition.

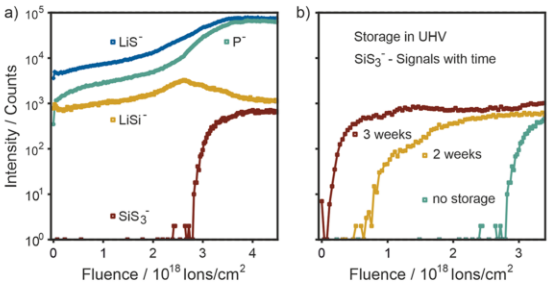


**Figure 4.** ToF-SIMS depth profiles of t-$Li_7SiPS_8$ with 3 μm of deposited Li (a) directly after lithium deposition and (b) evolution of the $SiS_3^-$ signal with storage time. $SiS_3^-$ is shown as a representative for a group of signals, which appear at a similar fluence.

P═S, $P_2S_n$, or $Li_2S_n$,[50] which presumably formed during synthesis. This peak can also be found in the P 2p spectrum at 133.0 eV (green). There are no signals indicating the presence of $Li_3P$ in the spectra of the pristine sample. However, a small amount of $Li_xP$ ($1 < x < 3$) can be detected at 130.4 eV after 15 min of lithium deposition indicating a reduction of the $PS_4^{3-}$ tetrahedra. This signal cannot be detected after 2 h of lithium deposition, which means that the $Li_xP$ concentration is below the detection limit of 0.05 at % for P 2p (see Supporting Information Table S6). A very small fraction of $Li_3P$ and a large fraction of $Li_2S$ would also explain the high resistance of the interphase as the ionic conductivity of $Li_2S$ is lower than that of $Li_3P$. Small impurities of silicone or siloxane (brown) appear at 102.1 eV (Si 2p spectrum).[51] A contamination with $SiS_2$ (102.5 eV[52]) can be excluded based on the NMR results. Another impurity at 103.0 eV is caused by $SiO_2$ (blue). Both impurities could also be due to side reactions with oxygen during synthesis in glassy carbon crucibles, storage in a glovebox, or during the sample transfer to the machine.

Lithium deposition on the SE pellet leads to the reduction of the SE. In the S 2p spectrum, the formation of $Li_2S$ (yellow) can be observed at 160.6 eV and its concentration increases with the amount of lithium deposited (approx. 30 nm after 2 h) until it dominates the spectrum after 2 h. The intensity of



https://doi.org/10.1021/acs.chemmater.1c04302
Chem. Mater. 2022, 34, 3659–3669

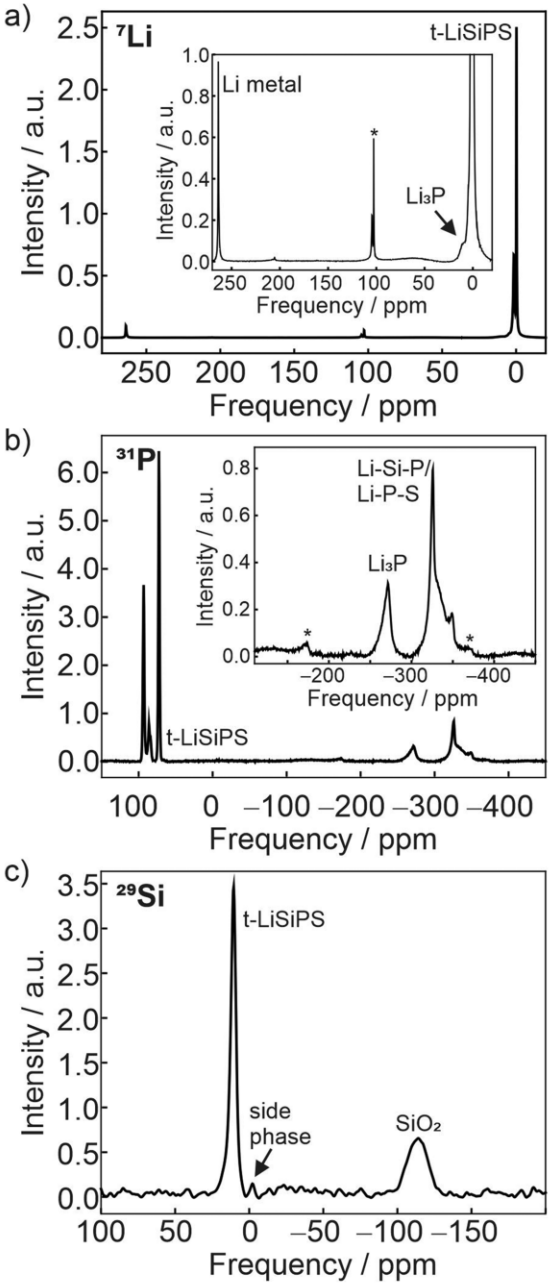


**Figure 5.** (a) $^{7}$Li, (b) $^{31}$P, and (c) $^{29}$Si MAS NMR spectra of t-$Li_7SiPS_8$ reacted with the liquid lithium metal. Spinning side bands, i.e., peaks that are artifacts of the MAS, are marked with an asterisk (*). The t-$Li_7SiPS_8$ peak in (c) could superimpose phosphidosilicate signals. The spectra were obtained at a spinning frequency of 24 kHz.

the P−$[S]_n$−P doublet increases upon Li deposition, which could be caused by the formation of the reduction product $Li_2SiS_3$ that has a doublet between 162.1 and 163.3 eV in the S 2p spectra superimposing the P−$[S]_n$−P peak.[52] As the Si 2p peak position of $Li_2SiS_3$ has the same position as t-$Li_7SiPS_8$, the distinction is not possible. The concentration of oxygen decreases from 19 at % in the pristine material to 13 at % after 2 h of lithium deposition. Likewise, the fractions of all three silicon compounds decrease with each deposition step as they get reduced as well as superimposed by the deposited lithium and formed $Li_2S$. It is noticeable that no $Si^0$ (99.5 eV[53]) or Li−Si alloy (≤97.5 eV[54]) was detected during the reaction, which could be due to the detection limit of the experimental setup. Another reason could be the higher stability of the $SiS_4^{4-}$ tetrahedron compared to the $PS_4^{3-}$ tetrahedron[17,20] so that the phosphorus tetrahedra are reduced first and the silicon tetrahedra remain stable, which is also predicted by the DFT calculations presented below.

The stability of the $SiS_4^{4-}$ anion is in contrast to the reaction of LGPS with lithium, as approximately 4 at % $Ge^0$ is formed during the reaction.[28] Additionally, the lower electrical conductivity and lithium diffusivity in silicon compared to germanium[55] could hinder the MCI formation in t-$Li_7SiPS_8$, which would explain the difference in reactivity compared to LGPS. Even though no elemental silicon or Li−Si alloy was detected with any of the analytical methods used in this work, the reaction between the SE and lithium continues (see electrochemical and ToF-SIMS results). This MCI growth might be caused by the formation of a compound with a partial electronic conductivity high enough to continue the decomposition reaction without decreasing the overall cell resistance, as can be seen in Figures 1 and 2.

ToF-SIMS was used to further investigate the Lilt-$Li_7SiPS_8$ interface and to study the nature of the formed interphase.[32] For this purpose, 1−3 $\mu$m thick lithium layers were deposited on the surface of an SE pellet and the resulting bilayers were investigated by ToF-SIMS depth profiling. In Figure 4a, the depth profile through a 3 $\mu$m thick lithium layer is shown. $LiS^-$ and $P^-$ signals, which are related to the elements contained in t-$Li_7SiPS_8$, are present since the beginning of the profiling process and show a pronounced increase in intensity with ongoing sputtering. Also, signals that appear only after a certain sputter time, like the $SiS_3^-$ signal, were identified, which indicates the formation of an SEI.[32] The $LiSi^-$ signal shows a maximum in signal intensity before the mentioned $SiS_3^-$ signal appears, which may indicate the presence of Li/Si compounds above other interphase reaction products. To learn more about the evolution of the interface with time, the sample with 3 $\mu$m of lithium on top of the SE pellet was stored under ultrahigh vacuum (UHV) conditions and remeasured after defined periods of storage time. It is important to note that the $SiS_3^-$ signal appears after shorter sputter time with increasing storage periods of 2 and 3 weeks as shown in Figure 4b. For further comparison, ToF-SIMS depth profiles of t-$Li_7SiPS_8$ with thinner lithium layers are shown in Supporting Information Figure S8. As for the 3 $\mu$m sample after storage, the $SiS_3^-$ signal appears after shorter sputter time for these samples and the evolution in intensity for the other described signals is shifted accordingly to lower sputter times. The similarity between the stored sample and the samples with thinner lithium layers indicates further growth of the interphase at the Lilt-$Li_7SiPS_8$ interface after initial deposition. This explains the ongoing increase of the interface resistance during electrochemical testing. Importantly, a non-negligible partial electronic conductivity of the interphase is necessary to explain this behavior. The measured profiles indicate the formation of an initially thin MCI that grows continuously afterward. This example emphasizes the need for time-dependent acquisition



https://doi.org/10.1021/acs.chemmater.1c04302
Chem. Mater. 2022, 34, 3659−3669

of ToF-SIMS depth profiles for the Li|SE samples as discussed elsewhere.[32]

The product formation of the reaction between t-$Li_7SiPS_8$ and the lithium metal was characterized by solid state MAS NMR spectroscopy. In Figure 5a, the $^7$Li NMR spectrum of the mixture is shown. In addition to the t-$Li_7SiPS_8$ peaks at 0 ppm and 2 ppm, a signal of the unreacted lithium metal is present at 264 ppm. The lithium metal signal occurs at a high chemical shift due to the Knight shift inherent to conductive compounds.[56] A broad resonance is visible at about 60 ppm. The shift is outside the chemical shift range characteristic for $^7$Li in a diamagnetic environment,[35] which indicates the presence of another electronically conductive phase. An additional, electronically conductive phase had also been suggested to explain the electrochemical as well as ToF-SIMS data. Another $^7$Li signal at 5 ppm is observed as a shoulder of the t-$Li_7SiPS_8$ peak, which can be assigned to $Li_3P$.[57]

The occurrence of $Li_3P$ is supported by the resonance at −270 ppm in the $^{31}$P spectrum (Figure 5b).[58] The two $^{31}$P signals at 73 and 94 ppm are assigned to t-$Li_7SiPS_8$.[12] Additionally, a $^{31}$P resonance at 86 ppm is observed, which was explained by the formation of an amorphous side phase during synthesis of t-$Li_7SiPS_8$ by Harm et al.[12] Furthermore, overlapping narrow and broad $^{31}$P signals are observed at approx. −326 ppm. For $^{31}$P, more negative values of the chemical shift correlate with an increased electron density at the phosphorus nucleus. Similarly, high-field shifted $^{31}$P signals have been reported for phosphidosilicates.[59,60] Alternatively, such a signal may be explained by a—potentially amorphous—solid solution of $Li_2S$ and $Li_3P$.[61,62] The relatively narrow width of some of the features of this signal indicates that well-ordered structures with some preferred $Li_2S$−$Li_3P$ compositions may exist. At the same time, some of the $^{31}$P nuclei appear to give rise to a rather broad signal contribution that points toward a more gradual distribution of the composition for parts of the sample.[61,62]

In the $^{29}$Si spectrum of the t-$Li_7SiPS_8$/lithium metal mixture three peaks are apparent (Figure 5c). The signal at 11 ppm can be assigned to t-$Li_7SiPS_8$. However, phosphidosilicates also have a peak in this range; thus, a superposition of both signals is possible.[59,60] The second peak at −2 ppm is barely distinguishable from noise and has been reported to originate from an amorphous side phase formed during the synthesis of the SE.[12] In line with other published data, the side phase peak amounts to about 1.1 at %. A broad peak for $SiO_2$ is observed at −114 ppm.[63] This signal is primarily assigned to a background signal caused by the MAS probe. Small fractions of $SiO_2$ that may be formed during the reaction of t-$Li_7SiPS_8$ with liquid lithium or during storage, as was suggested based on the XPS data, would not amount to such a large signal. Due to the large amplitude of this background, such a byproduct cannot be identified reliably by NMR. Consistent with the XPS spectra, no $SiS_2$[64,65] or elemental silicon signals are observed in the $^{29}$Si spectrum.

To summarize, the chemical characterization and the XPS, ToF-SIMS, and MAS NMR measurements show that a slowly growing MCI is formed even though no silicon metal can be detected.

To get more insights into the atomistic processes that occur at the interface between t-$Li_7SiPS_8$ and the lithium metal, DFT calculations have been employed. First, the stability of t-$Li_7SiPS_8$ was estimated based on the following reaction:

$$Li_7SiPS_8 + 8Li \rightarrow 4Li_2S + Li_3P + Li_4SiS_4 \quad (1)$$

The reaction is found to be exothermic with a calculated reaction energy of −11.87 eV, corresponding to −475 meV/atom or −1145 kJ/mol. The large reaction energy proves the thermodynamic instability of t-$Li_7SiPS_8$ in contact with the lithium metal, other decomposition reactions might be even more exothermic.

The interface reactions are investigated using explicit interface models and the initial structural model is shown in Figure 6a. The t-$Li_7SiPS_8$ slab has two interfaces with the Li metal. First, a $PS_4^{3-}$-rich interface with four $PS_4^{3-}$ units located in the center of the simulation cell, and second, a $SiS_4^{4-}$-rich interface with four $SiS_4^{4-}$ units at the bottom (connected to the Li metal via the periodic boundary conditions). Two different models with slightly different slab separation distances at the $PS_4^{3-}$-rich interface were generated and statically optimized (see Supporting Information Figure S9). The initial slab separation distance seems to have a negligible influence on the outcome of the interface reaction and substantial interface reactions are already observed in the static calculations.

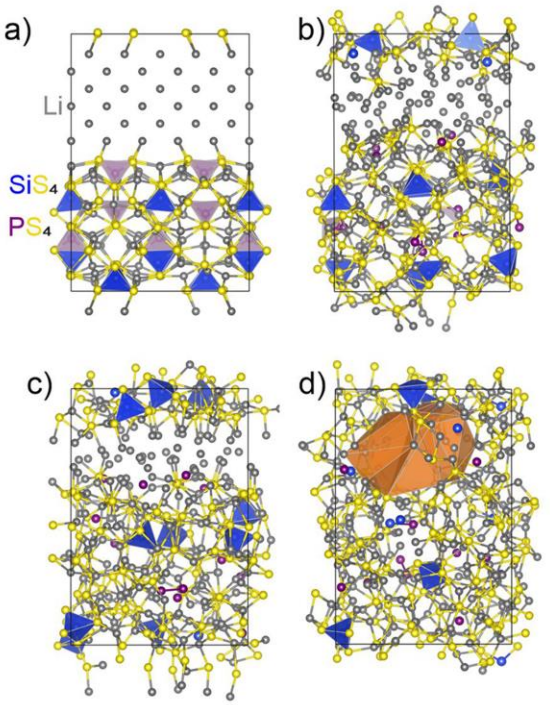


**Figure 6.** (a) Illustration of the initial t-$Li_7SiPS_8$|Li interface for DFT calculations, which was first optimized in static calculations and then subjected to AIMD simulations at various temperatures to monitor the ongoing interface reaction. The resulting interphases are mostly amorphous and shown in (b) obtained after 60 ps at 300 K, (c) after 60 ps at 500 K, and (d) after 50 ps at 700 K. The large, orange object in (d) indicates a pore that formed during the simulation.

To investigate how the interface evolves at a finite temperature, AIMD simulations at 300, 500, and 700 K were conducted using the statically optimized interface models as the starting structure. The obtained structures after 50 to 60 ps are mostly amorphous and are shown in Figure 6b−d.



https://doi.org/10.1021/acs.chemmater.1c04302
Chem. Mater. 2022, 34, 3659−3669

Additional structures at different times can be seen in Supporting Information Figure S10. Most notably, the $PS_4^{3-}$ units are vulnerable to decomposition, similarly as reported for other sulfide SEs.[66,67] In the AIMD simulations, we observe that all $PS_4^{3-}$ units are dissociated after only 10 ps at 300 K. In contrast, several $SiS_4^{4-}$ remain intact even after 55 ps at 700 K, hinting at their superior stability relative to the $PS_4^{3-}$ unit. Comparable observations have been made for LGPS|Li interface simulations.[68] Given the short simulation times that can be reached with the state-of-the-art AIMD simulations, however, we expect that also the remaining $SiS_4^{4-}$ units will dissociate at prolonged simulation times if enough Li metal is locally available. Potentially this could lead to the phosphidosilicates observed in the NMR studies.

The identification of reaction phases is complicated by the amorphous structure of the interphase. Nevertheless, the onset of an amorphous $Li_2S$ formation can be speculated, as there are several regions were six to eight $Li^+$ ions span irregular coordination polyhedra around $S^{2-}$ ions. Likewise, P ions are found to be surrounded by irregular coordination polyhedra of eight or nine $Li^+$ ions that might be attributed to the early stages of $Li_3P$.[67] Furthermore, the formation of pores is observed (see Figure 6d), which is due to the fact that the reaction products most likely lead to a reduction of the volume as shown in Supporting Information Table S7. In this regard, the constant volume conditions of the simulation certainly promote pore formation if reactions lead to volume reduction.

To monitor the energetics of the system, snapshot structures were extracted from the AIMD simulations every picosecond and structurally optimized to remove any thermal influence. The obtained reaction energies are shown in Supporting Information Figure S11 and indicate a continuously proceeding exothermic reaction. After 55 ps at 700 K, the reaction energy approximates −480 meV/atom, close to the one for the assumed reaction in eq 1.

In addition to the amorphous interfaces, also the formation of an ordered interface was observed during a simulation at 500 K. A side view of the structure obtained after 60 ps together with an inclined top view on one of its layers are shown in Figure 7a,b, respectively. Additional structural models are visualized in Supporting Information Figures S12 and S13. The local atomic arrangement indicates that nanocrystalline regions of $Li_2S$ have formed.

Thin $Li_2S$ layers have already been suggested as a protective coating for LPS against the lithium metal and showed an improved cycling performance of cells employing LMAs and LTO.[69,70] The ongoing reaction observed in the impedance and ToF-SIMS measurements, however, indicates that $Li_2S$ is not able to passivate the interface in the present case. This might be due to the fact that $Li_2S$ is either (partly) amorphous, as observed in the remaining simulations, or that the ordered $Li_2S$ phase is highly defective: $PLi_x$ clusters, intact $SiS_4^{4-}$ units but also $SiS_3^{2-}$ units are embedded in the ordered $Li_2S$ interphase. As a result, coordination polyhedra such as $S(SiLi_6)$ around the $S^{2-}$ ions are observed. This is similar to $Li_2S$, where lithium has partially been substituted with silicon. Effectively, this introduces $Li^+$ vacancies in $Li_2S$ (e.g., the indicated $SLi_7$ coordination polyhedra in Figure 7b) that might improve the $Li^+$ conduction of the interphase. Possibly, the high defect density might also enable the diffusion of other species that might contribute to the ongoing growth of the interphase.

The eDOS was calculated to investigate whether the interphase exhibits a mixed electronic−ionic conductivity

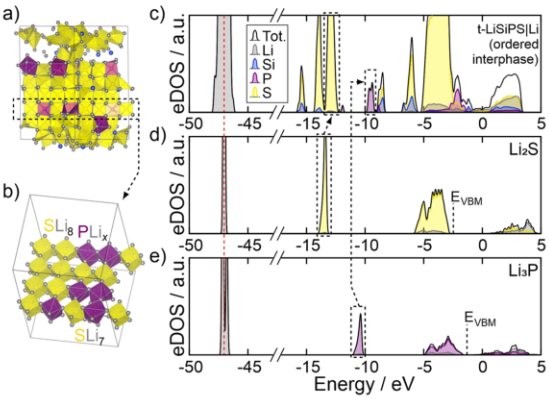


**Figure 7.** (a) Side view of the t-$Li_7SiPS_8$|Li interface where an ordered interphase formed during an AIMD simulation at 500 K. (b) Inclined top view on the indicated layer. Visualized $SLi_8$ and $PLi_x$ (with $x$ = 8 or 9) coordination polyhedra indicate the formation of $Li_2S$ and early stages of $Li_3P$. Additionally, one $SLi_7$ unit is marked. The eDOS is shown for (c) model with the ordered interphase, (d) bulk $Li_2S$, and (e) bulk $Li_3P$. The eDOS has been aligned according to the Li(1s) core states (red, dashed line).

(see Figure 7c). Indeed, a slight metallic character is observed for the interface with the ordered interphase. This observation, however, is rather attributed to thin, yet unreacted lithium metal layers and the exact properties of the interphase are difficult to extract. In accordance to the structural analysis, the eDOS of the ordered interface shows features of the eDOS of the binary phases $Li_2S$ and $Li_3P$ (Figure 7d,e). Remarkably, the eDOS of the ordered interface resembles those of the amorphous structures, as shown in Supporting Information Figure S14, indicating that at least their local atomic arrangements are comparable.

Despite the small system size and simulation times compared to real systems, the generated insights into the interface/interphase evolution between t-$Li_7SiPS_8$ and the lithium metal certainly aid the further understanding of interface degradation mechanisms, interphase formation, and further interface phenomena. This might be helpful for the development of protection schemes for t-$Li_7SiPS_8$ or comparable SEs.

## ■ CONCLUSIONS

Tetragonal $Li_7SiPS_8$ (t-$Li_7SiPS_8$) SE is unstable against reaction with the LMA. The temporal evolution of the Li|t-$Li_7SiPS_8$|Li cell impedance shows a severe degradation with a resistance increase over two orders of magnitude as well as a change in the interphase growth kinetics, which may indicate a change in the rate-determining step. In situ XPS and ToF-SIMS, as well as NMR spectroscopy are used to study the decomposition reaction. The XPS measurements show that the main decomposition product formed during lithium deposition is $Li_2S$, and no elemental silicon or Li−Si alloy is detected. This is confirmed by NMR spectroscopy of a mixture prepared from the liquid lithium metal and t-$Li_7SiPS_8$ powder. Furthermore, $Li_3P$ and possibly phosphidosilicates are detected. We hypothesize that the phosphidosilicates could serve as a source for sufficient partial electronic conductivity[59,60] to enable the continuous growth of the interphase, which distinguishes this SE from pure Li−P−S electrolytes.



https://doi.org/10.1021/acs.chemmater.1c04302
Chem. Mater. 2022, 34, 3659−3669

ToF-SIMS depth profiling through micrometer-thick lithium layers deposited on the SE showed initially a picture typical for SEI formation. However, repeating the depth profiling after a defined storage time revealed an ongoing interphase growth, which indicates the formation of a steadily growing MCI. This is in accordance with the observations of the electrochemical reaction by impedance measurements.

The experimental findings are in line with DFT calculations and AIMD simulations showing that $PS_4^{3-}$ tetrahedra are more prone to dissociation than $SiS_4^{4-}$ tetrahedra. Thus, silicon-containing solid electrolytes seem to be promising candidates for metal-ion containing solid electrolytes in principle. However, a careful individual consideration is necessary, and the compound studied in this paper cannot be combined with an LMA without a protective anode concept.

## ■ ASSOCIATED CONTENT

### Supporting Information

The Supporting Information is available free of charge at https://pubs.acs.org/doi/10.1021/acs.chemmater.1c04302.

XRD diffractograms and crystallographic data from Rietveld refinement of synthesized and reacted t-$Li_7SiPS_8$; enlarged Nyquist plots for the first hours of measurements of Figures 1 and 2; temporal evolution of capacitances; interphase resistance vs square root of time; detection limit of the P 2p XPS signal; ToF-SIMS depth profiles using 1 and 2 $\mu$m of lithium, respectively; DFT calculations and AIMD simulations of t-$Li_7SiPS_8$; calculated volume changes; calculation of the reaction energy; and the eDOS of possible decomposition products (PDF)

## ■ AUTHOR INFORMATION


### Corresponding Author

**Jürgen Janek** − *Institute of Physical Chemistry, Justus-Liebig-University Giessen, Giessen D-35392, Germany; Center for Materials Research (ZfM), Justus-Liebig-University Giessen, Giessen D-35392, Germany;* orcid.org/0000-0002-9221-4756; Email: juergen.janek@phys.chemie.uni-giessen.de

### Authors

**Luise M. Riegger** − *Institute of Physical Chemistry, Justus-Liebig-University Giessen, Giessen D-35392, Germany; Center for Materials Research (ZfM), Justus-Liebig-University Giessen, Giessen D-35392, Germany*

**Svenja-K. Otto** − *Institute of Physical Chemistry, Justus-Liebig-University Giessen, Giessen D-35392, Germany; Center for Materials Research (ZfM), Justus-Liebig-University Giessen, Giessen D-35392, Germany*

**Marcel Sadowski** − *Institute of Materials Science, Technical University of Darmstadt, Darmstadt D-64287, Germany;* orcid.org/0000-0001-9869-6162

**Sven Jovanovic** − *Forschungszentrum Jülich GmbH, IEK-9: Fundamental Electrochemistry, Jülich D-52425, Germany*

**Olaf Kötz** − *Institute of Physical Chemistry, Justus-Liebig-University Giessen, Giessen D-35392, Germany; Center for Materials Research (ZfM), Justus-Liebig-University Giessen, Giessen D-35392, Germany*

**Sascha Harm** − *Max Planck Institute for Solid State Research, Stuttgart D-70569, Germany; Department of Chemistry, Ludwig-Maximilians-Universität München, München D-81377, Germany*

**Lucas G. Balzat** − *Max Planck Institute for Solid State Research, Stuttgart D-70569, Germany; Department of Chemistry, Ludwig-Maximilians-Universität München, München D-81377, Germany*

**Steffen Merz** − *Forschungszentrum Jülich GmbH, IEK-9: Fundamental Electrochemistry, Jülich D-52425, Germany*

**Simon Burkhardt** − *Institute of Physical Chemistry, Justus-Liebig-University Giessen, Giessen D-35392, Germany; Center for Materials Research (ZfM), Justus-Liebig-University Giessen, Giessen D-35392, Germany*

**Felix H. Richter** − *Institute of Physical Chemistry, Justus-Liebig-University Giessen, Giessen D-35392, Germany; Center for Materials Research (ZfM), Justus-Liebig-University Giessen, Giessen D-35392, Germany;* orcid.org/0000-0002-6587-7757

**Joachim Sann** − *Institute of Physical Chemistry, Justus-Liebig-University Giessen, Giessen D-35392, Germany; Center for Materials Research (ZfM), Justus-Liebig-University Giessen, Giessen D-35392, Germany*

**Rüdiger-A. Eichel** − *Forschungszentrum Jülich GmbH, IEK-9: Fundamental Electrochemistry, Jülich D-52425, Germany; Institute of Physical Chemistry, RWTH Aachen University, Aachen D-52056, Germany;* orcid.org/0000-0002-0013-6325

**Bettina V. Lotsch** − *Max Planck Institute for Solid State Research, Stuttgart D-70569, Germany; Department of Chemistry, Ludwig-Maximilians-Universität München, München D-81377, Germany;* orcid.org/0000-0002-3094-303X

**Josef Granwehr** − *Forschungszentrum Jülich GmbH, IEK-9: Fundamental Electrochemistry, Jülich D-52425, Germany*

**Karsten Albe** − *Institute of Materials Science, Technical University of Darmstadt, Darmstadt D-64287, Germany;* orcid.org/0000-0003-4669-8056

Complete contact information is available at: https://pubs.acs.org/10.1021/acs.chemmater.1c04302


### Author Contributions

The manuscript was written through contributions of L.R. (abstract, introduction, electrochemical characterization, XPS characterization, and conclusions), S.-K.O. (ToF-SIMS characterization), M.S. (theoretical calculations), S.J. and S.M. (NMR characterization), and S.H. (material synthesis). Data curation was done by L.R. (temporal impedance evolution and XPS measurements), S.-K.O. (ToF-SIMS measurement), M.S. (theoretical calculations), S.J. and S.M. (NMR measurement), and S.H. and L.G.B. (material synthesis and Rietveld refinement). Manuscript editing was done by S.B., F.H.R., J.S., F.R., B.V.L., J.G., K.A., and J.J. Funding acquisition was done by B.V.L., J.G., K.A., and J.J. All authors have given approval to the final version of the manuscript. S.J. and S.M. contributed equally to the NMR measurement. S.H and L.G.B. contributed equally to the material synthesis and Rietveld refinement.

### Notes

The authors declare no competing financial interest.

## ■ ACKNOWLEDGMENTS

This work has been partly funded by the German Federal Ministry of Education and Research (BMBF) within the project "FESTBATT," grant identifier 03XP0177A, 03XP0177D, 03XP0177B, 03XP0176, and 03XP0174A.

Calculations for this research were conducted on the Lichtenberg high performance computer of Technical University of Darmstadt. We greatly appreciate helpful discussions with R. Rueß. Furthermore, the authors thank Conrad Szcuka and Clare P. Grey for the fruitful discussions about their analytical results on NMR resonances of $Li_2S$−$Li_3P$ solid solutions.[61]

## ■ REFERENCES

(1) Sun, Y.-K. Promising All-Solid-State Batteries for Future Electric Vehicles. *ACS Energy Lett.* **2020**, *5*, 3221−3223.
(2) Janek, J.; Zeier, W. G. A solid future for battery development. *Nat. Energy* **2016**, *1*, 1167.
(3) Weiss, M.; Ruess, R.; Kasnatscheew, J.; Levartovsky, Y.; Levy, N. R.; Minnmann, P.; Stolz, L.; Waldmann, T.; Wohlfahrt-Mehrens, M.; Aurbach, D.; Winter, M.; Ein-Eli, Y.; Janek, J. Fast Charging of Lithium-Ion Batteries: A Review of Materials Aspects. *Adv. Energy Mater.* **2021**, No. 2101126.
(4) Kamaya, N.; Homma, K.; Yamakawa, Y.; Hirayama, M.; Kanno, R.; Yonemura, M.; Kamiyama, T.; Kato, Y.; Hama, S.; Kawamoto, K.; Mitsui, A. A lithium superionic conductor. *Nat. Mater.* **2011**, *10*, 682−686.
(5) Hori, S.; Kato, M.; Suzuki, K.; Hirayama, M.; Kato, Y.; Kanno, R. Phase Diagram of the $Li_4GeS_4$-$Li_3PS_4$ Quasi-Binary System Containing the Superionic Conductor $Li_{10}GeP_2S_{12}$. *J. Am. Ceram. Soc.* **2015**, *98*, 3352−3360.
(6) Kuhn, A.; Köhler, J.; Lotsch, B. V. Single-crystal X-ray structure analysis of the superionic conductor $Li_{10}GeP_2S_{12}$. *Phys. Chem. Chem. Phys.* **2013**, *15*, 11620−11622.
(7) Bron, P.; Johansson, S.; Zick, K.; Schmedt auf der Günne, J.; Dehnen, S.; Roling, B. $Li_{10}SnP_2S_{12}$: an affordable lithium superionic conductor. *J. Am. Chem. Soc.* **2013**, *135*, 15694−15697.
(8) Bron, P.; Dehnen, S.; Roling, B. $Li_{10}Si_{0.3}Sn_0\ P_2S_{12}$ − A low-cost and low-grain-boundary-resistance lithium superionic conductor. *J. Power Sources* **2016**, *329*, 530−535.
(9) Whiteley, J. M.; Woo, J. H.; Hu, E.; Nam, K.-W.; Lee, S.-H. Empowering the Lithium Metal Battery through a Silicon-Based Superionic Conductor. *J. Electrochem. Soc.* **2014**, *161*, A1812−A1817.
(10) Kato, Y.; Saito, R.; Sakano, M.; Mitsui, A.; Hirayama, M.; Kanno, R. Synthesis, structure and lithium ionic conductivity of solid solutions of $Li_{10}(Ge_{1-x}M_x)P_2S_{12}$ (M = Si, Sn). *J. Power Sources* **2014**, *271*, 60−64.
(11) Kuhn, A.; Gerbig, O.; Zhu, C.; Falkenberg, F.; Maier, J.; Lotsch, B. V. A new ultrafast superionic Li-conductor: ion dynamics in $Li_{11}Si_2PS_{12}$ and comparison with other tetragonal LGPS-type electrolytes. *Phys. Chem. Chem. Phys.* **2014**, *16*, 14669−14674.
(12) Harm, S.; Hatz, A.-K.; Moudrakovski, I.; Eger, R.; Kuhn, A.; Hoch, C.; Lotsch, B. V. Lesson Learned from NMR: Characterization and Ionic Conductivity of LGPS-like $Li_7SiPS_8$. *Chem. Mater.* **2019**, *31*, 1280−1288.
(13) Richards, W. D.; Miara, L. J.; Wang, Y.; Kim, J. C.; Ceder, G. Interface Stability in Solid-State Batteries. *Chem. Mater.* **2016**, *28*, 266−273.
(14) Lau, J.; DeBlock, R. H.; Butts, D. M.; Ashby, D. S.; Choi, C. S.; Dunn, B. S. Sulfide Solid Electrolytes for Lithium Battery Applications. *Adv. Energy Mater.* **2018**, *8*, No. 1800933.
(15) Zhu, Y.; He, X.; Mo, Y. Origin of Outstanding Stability in the Lithium Solid Electrolyte Materials: Insights from Thermodynamic Analyses Based on First-Principles Calculations. *ACS Appl. Mater. Interfaces* **2015**, *7*, 23685−23693.
(16) Zhu, Y.; He, X.; Mo, Y. First principles study on electrochemical and chemical stability of solid electrolyte−electrode interfaces in all-solid-state Li-ion batteries. *J. Mater. Chem. A* **2016**, *4*, 3253−3266.
(17) Zhu, Y.; He, X.; Mo, Y. Strategies Based on Nitride Materials Chemistry to Stabilize Li Metal Anode. *Adv. Sci.* **2017**, *4*, No. 1600517.
(18) Han, F.; Zhu, Y.; He, X.; Mo, Y.; Wang, C. Electrochemical Stability of $Li_{10}GeP_2S_{12}$ and $Li_7La_3Zr_2O_{12}$ Solid Electrolytes. *Adv. Energy Mater.* **2016**, *6*, No. 1501590.
(19) Ong, S. P.; Mo, Y.; Richards, W. D.; Miara, L.; Lee, H. S.; Ceder, G. Phase stability, electrochemical stability and ionic conductivity of the $Li_{10\pm1}MP_2X_{12}$ (M = Ge, Si, Sn, Al or P, and X = O, S or Se) family of superionic conductors. *Energy Environ. Sci.* **2013**, *6*, 148−156.
(20) Chen, F.; Cheng, S.; Liu, J.-B.; Li, S.; Ouyang, W.; Liu, B. Insights into the Electrochemical Stability and Lithium Conductivity of $Li_4MS_4$ (M = Si, Ge, and Sn). *ACS Appl. Mater. Interfaces* **2021**, *13*, 22438−22447.
(21) Schwietert, T. K.; Arszelewska, V. A.; Wang, C.; Yu, C.; Vasileiadis, A.; de Klerk, N. J. J.; Hageman, J.; Hupfer, T.; Kerkamm, I.; Xu, Y.; van der Maas, E.; Kelder, E. M.; Ganapathy, S.; Wagemaker, M. Clarifying the relationship between redox activity and electrochemical stability in solid electrolytes. *Nat. Mater.* **2020**, *19*, 428−435.
(22) Ohno, S.; Rosenbach, C.; Dewald, G. F.; Janek, J.; Zeier, W. G. Linking Solid Electrolyte Degradation to Charge Carrier Transport in the Thiophosphate-Based Composite Cathode toward Solid-State Lithium-Sulfur Batteries. *Adv. Funct. Mater.* **2021**, *31*, No. 2010620.
(23) Han, F.; Gao, T.; Zhu, Y.; Gaskell, K. J.; Wang, C. A Battery Made from a Single Material. *J. Adv. Mater.* **2015**, *27*, 3473−3483.
(24) Wenzel, S.; Sedlmaier, S. J.; Dietrich, C.; Zeier, W. G.; Janek, J. Interfacial reactivity and interphase growth of argyrodite solid electrolytes at lithium metal electrodes. *Solid State Ionics* **2018**, *318*, 102−112.
(25) Wenzel, S.; Weber, D. A.; Leichtweiss, T.; Busche, M. R.; Sann, J.; Janek, J. Interphase formation and degradation of charge transfer kinetics between a lithium metal anode and highly crystalline $Li_7P_3S_{11}$ solid electrolyte. *Solid State Ionics* **2016**, *286*, 24−33.
(26) Wood, K. N.; Steirer, K. X.; Hafner, S. E.; Ban, C.; Santhanagopalan, S.; Lee, S.-H.; Teeter, G. Operando X-ray photoelectron spectroscopy of solid electrolyte interphase formation and evolution in $Li_2S$-$P_2S_5$ solid-state electrolytes. *Nat. Commun.* **2018**, *9*, 2490.
(27) Liu, Z.; Borodin, A.; Li, G.; Liu, X.; Li, Y.; Endres, F. X-ray Photoelectron Spectroscopy Probing of the Interphase between Solid-State Sulfide Electrolytes and a Lithium Anode. *J. Phys. Chem. C* **2020**, *124*, 300−308.
(28) Wenzel, S.; Randau, S.; Leichtweiß, T.; Weber, D. A.; Sann, J.; Zeier, W. G.; Janek, J. Direct Observation of the Interfacial Instability of the Fast Ionic Conductor $Li_{10}GeP_2S_{12}$ at the Lithium Metal Anode. *Chem. Mater.* **2016**, *28*, 2400−2407.
(29) Wenzel, S.; Leichtweiss, T.; Krüger, D.; Sann, J.; Janek, J. Interphase formation on lithium solid electrolytes—An in situ approach to study interfacial reactions by photoelectron spectroscopy. *Solid State Ionics* **2015**, *278*, 98−105.
(30) Riegger, L. M.; Schlem, R.; Sann, J.; Zeier, W. G.; Janek, J. Lithium-Metal Anode Instability of the Superionic Halide Solid Electrolytes and the Implications for Solid-State Batteries. *Angew. Chem., Int. Ed.* **2021**, *60*, 6718−6723.
(31) Wenzel, S.; Leichtweiss, T.; Weber, D. A.; Sann, J.; Zeier, W. G.; Janek, J. Interfacial Reactivity Benchmarking of the Sodium Ion Conductors Na3PS4 and Sodium $\beta$-Alumina for Protected Sodium Metal Anodes and Sodium All-Solid-State Batteries. *ACS Appl. Mater. Interfaces* **2016**, *8*, 28216−28224.
(32) Otto, S.-K.; Riegger, L. M.; Fuchs, T.; Kayser, S.; Schweitzer, P.; Burkhardt, S.; Henss, A.; Janek, J. In Situ Investigation of Lithium Metal−Solid Electrolyte Anode Interfaces with ToF-SIMS. *Adv. Mater. Interfaces* **2022**, No. 2102387.
(33) Ahn, B. T.; Huggins, R. A. Synthesis and lithium conductivities of $Li_2SiS_3$ and $Li_4SiS_4$. *Mat. Res. Bull.* **1989**, *24*, 889−897.
(34) Coelho, A. A. TOPAS and TOPAS-Academic: an optimization program integrating computer algebra and crystallographic objects written in C++. *J. Appl. Crystallogr.* **2018**, *51*, 210−218.
(35) Köcher, S. S.; Schleker, P. P. M.; Graf, M. F.; Eichel, R.-A.; Reuter, K.; Granwehr, J.; Scheurer, C. Chemical shift reference scale



https://doi.org/10.1021/acs.chemmater.1c04302
*Chem. Mater.* 2022, 34, 3659−3669

for Li solid state NMR derived by first-principles DFT calculations. *J. Magn. Reson.* **2018**, *297*, 33−41.
(36) Kresse, G.; Hafner, J. Ab initio molecular-dynamics simulation of the liquid-metal–amorphous-semiconductor transition in germanium. *Phys. Rev. B* **1994**, *49*, 14251−14269.
(37) Kresse, G. Ab initio molecular dynamics for liquid metals. *J. Non-Cryst. Solids* **1995**, *192*−*193*, 222−229.
(38) Kresse, G.; Furthmüller, J. Efficiency of ab-initio total energy calculations for metals and semiconductors using a plane-wave basis set. *Comput. Mater. Sci.* **1996**, *6*, 15−50.
(39) Kresse, G.; Furthmüller, J. Efficient iterative schemes for ab initio total-energy calculations using a plane-wave basis set. *Phys. Rev. B: Condens. Matter* **1996**, *54*, 11169−11186.
(40) Blöchl, P. E. Projector augmented-wave method. *Phys. Rev. B: Condens. Matter* **1994**, *50*, 17953−17979.
(41) Kresse, G.; Joubert, D. From ultrasoft pseudopotentials to the projector augmented-wave method. *Phys. Rev. B: Condens. Matter* **1999**, *59*, 1758−1775.
(42) Perdew, J. P.; Burke, K.; Ernzerhof, M. Generalized Gradient Approximation Made Simple. *Phys. Rev. Lett.* **1996**, *77*, 3865−3868.
(43) Zhang, Y.; Yang, W. Comment on "Generalized Gradient Approximation Made Simple". *Phys. Rev. Lett.* **1998**, *80*, 890.
(44) Perdew, J. P.; Burke, K.; Ernzerhof, M. Generalized Gradient Approximation Made Simple. *Phys. Rev. Lett.* **1997**, *78*, 1396.
(45) Okhotnikov, K.; Charpentier, T.; Cadars, S. Supercell program: a combinatorial structure-generation approach for the local-level modeling of atomic substitutions and partial occupancies in crystals. *Aust. J. Chem.* **2016**, *8*, 17.
(46) Krauskopf, T.; Hartmann, H.; Zeier, W. G.; Janek, J. Toward a Fundamental Understanding of the Lithium Metal Anode in Solid-State Batteries-An Electrochemo-Mechanical Study on the Garnet-Type Solid Electrolyte $Li_{6.25}Al_{0.25}La_3Zr_2O_{12}$. *ACS Appl. Mater. Interfaces* **2019**, *11*, 14463−14477.
(47) Schmalzried, H. *Chemical Kinetics of Solids*; Wiley-VCH Verlag GmbH, 1995.
(48) Simon, F. J.; Hanauer, M.; Richter, F. H.; Janek, J. Interphase Formation of $PEO_{20}$:LiTFSI-$Li_6PS_5Cl$ Composite Electrolytes with Lithium Metal. *ACS Appl. Mater. Interfaces* **2020**, *12*, 11713−11723.
(49) Walther, F.; Koerver, R.; Fuchs, T.; Ohno, S.; Sann, J.; Rohnke, M.; Zeier, W. G.; Janek, J. Visualization of the Interfacial Decomposition of Composite Cathodes in Argyrodite-Based All-Solid-State Batteries Using Time-of-Flight Secondary-Ion Mass Spectrometry. *Chem. Mater.* **2019**, *31*, 3745−3755.
(50) Walther, F.; Randau, S.; Schneider, Y.; Sann, J.; Rohnke, M.; Richter, F. H.; Zeier, W. G.; Janek, J. Influence of Carbon Additives on the Decomposition Pathways in Cathodes of Lithium Thiophosphate-Based All-Solid-State Batteries. *Chem. Mater.* **2020**, *32*, 6123−6136.
(51) Beamson, G.; Briggs, D. *High resolution XPS of organic polymers: The Scienta ESCA300 database*; Wiley, 1992.
(52) Foix, D.; Gonbeau, D.; Taillades, G.; Pradel, A.; Ribes, M. The structure of ionically conductive chalcogenide glasses: a combined NMR, XPS and ab initio calculation study. *Solid State Sci.* **2001**, *3*, 235−243.
(53) Jensen, D. S.; Kanyal, S. S.; Madaan, N.; Vail, M. A.; Dadson, A. E.; Engelhard, M. H.; Linford, M. R. Silicon (100)/$SiO_2$ by XPS. *Surf. Sci. Spectra* **2013**, *20*, 36−42.
(54) Philippe, B.; Dedryvère, R.; Allouche, J.; Lindgren, F.; Gorgoi, M.; Rensmo, H.; Gonbeau, D.; Edström, K. Nanosilicon Electrodes for Lithium-Ion Batteries: Interfacial Mechanisms Studied by Hard and Soft X-ray Photoelectron Spectroscopy. *Chem. Mater.* **2012**, *24*, 1107−1115.
(55) Abel, P. R.; Chockla, A. M.; Lin, Y.-M.; Holmberg, V. C.; Harris, J. T.; Korgel, B. A.; Heller, A.; Mullins, C. B. Nanostructured $Si_{(1-x)}Ge_x$ for tunable thin film lithium-ion battery anodes. *ACS Nano* **2013**, *7*, 2249−2257.
(56) Arai, J.; Okada, Y.; Sugiyama, T.; Izuka, M.; Gotoh, K.; Takeda, K. In Situ Solid State $^7$Li NMR Observations of Lithium Metal Deposition during Overcharge in Lithium Ion Batteries. *J. Electrochem. Soc.* **2015**, *162*, A952−A958.
(57) León, B.; Corredor, J. I.; Tirado, J. L.; Pérez-Vicente, C. On the Mechanism of the Electrochemical Reaction of Tin Phosphide with Lithium. *J. Electrochem. Soc.* **2006**, *153*, A1829.
(58) Mayo, M.; Griffith, K. J.; Pickard, C. J.; Morris, A. J. Ab Initio Study of Phosphorus Anodes for Lithium- and Sodium-Ion Batteries. *Chem. Mater.* **2016**, *28*, 2011−2021.
(59) Strangmüller, S.; Eickhoff, H.; Müller, D.; Klein, W.; Raudaschl-Sieber, G.; Kirchhain, H.; Sedlmeier, C.; Baran, V.; Senyshyn, A.; Deringer, V. L.; van Wüllen, L.; Gasteiger, H. A.; Fässler, T. F. Fast Ionic Conductivity in the Most Lithium-Rich Phosphidosilicate $Li_{14}SiP_6$. *J. Am. Chem. Soc.* **2019**, *141*, 14200−14209.
(60) Toffoletti, L.; Kirchhain, H.; Landesfeind, J.; Klein, W.; van Wüllen, L.; Gasteiger, H. A.; Fässler, T. F. Lithium Ion Mobility in Lithium Phosphidosilicates: Crystal Structure, $^7$Li, $^{29}$Si, and $^{31}$P MAS NMR Spectroscopy, and Impedance Spectroscopy of $Li_8SiP_4$ and $Li_2SiP_2$. *Chem. − Eur. J.* **2016**, *22*, 17635−17645.
(61) Szczuka, C.; Grey, C. P. Private Communication, 2021.
(62) Szczuka, C. Investigation of the ternary Li-P-S phase diagram for application in electrochemical systems. Master Thesis, RWTH Aachen: Aachen, 2019.
(63) Leonardelli, L.; Facchini, L.; Fretigny, C.; Tougne, P.; Legrand, A. P. Silicon-29 NMR study of silica. *J. Am. Chem. Soc.* **1992**, *114*, 6412−6418.
(64) Eckert, H.; Kennedy, J. H.; Pradel, A.; Ribes, M. Structural transformation of thiosilicate glasses: $^{29}$Si MAS-NMR evidence for edge-sharing in the system $Li_2S$-$SiS_2$. *J. Non-Cryst. Solids* **1989**, *113*, 287−293.
(65) Pradel, A.; Taillades, G.; Ribes, M.; Eckert, H. $^{29}$Si NMR structural studies of ionically conductive silicon chalcogenide glasses and model compounds. *J. Non-Cryst. Solids* **1995**, *188*, 75−86.
(66) Lepley, N. D.; Holzwarth, N. A. W. Modeling interfaces between solids: Application to Li battery materials. *Phys. Rev. B* **2015**, *92*, No. 214201.
(67) Camacho-Forero, L. E.; Balbuena, P. B. Exploring interfacial stability of solid-state electrolytes at the lithium-metal anode surface. *J. Power Sources* **2018**, *396*, 782−790.
(68) Chen, B.; Ju, J.; Ma, J.; Zhang, J.; Xiao, R.; Cui, G.; Chen, L. An insight into intrinsic interfacial properties between Li metals and $Li_{10}GeP_2S_{12}$ solid electrolytes. *Phys. Chem. Chem. Phys.* **2017**, *19*, 31436−31442.
(69) Lepley, N. D.; Holzwarth, N. A. W.; Du, Y. A. Structures, $Li^+$ mobilities, and interfacial properties of solid electrolytes $Li_3PS_4$and $Li_3PO_4$ from first principles. *Phys. Rev. B* **2013**, *88*, No. 104103.
(70) Chen, H.; Pei, A.; Lin, D.; Xie, J.; Yang, A.; Xu, J.; Lin, K.; Wang, J.; Wang, H.; Shi, F.; Boyle, D.; Cui, Y. Uniform High Ionic Conducting Lithium Sulfide Protection Layer for Stable Lithium Metal Anode. *Adv. Energy Mater.* **2019**, *9*, No. 1900858.



https://doi.org/10.1021/acs.chemmater.1c04302
*Chem. Mater.* 2022, 34, 3659−3669

## 3.3 Publication 3: "Evolution of the Interphase between Argyrodite-based Solid Electrolytes and the Lithium Metal Anode – The Kinetics of Solid Electrolyte Interphase Growth"

In Publication 3 of this doctoral thesis, a three-electrode setup is presented and used to study the SEI evolution of symmetric Li|$Li_6PS_5Cl$|In/InLi@Ni|$Li_6PS_5Cl$|Li cells. Using differently treated lithium foils, the influence of the lithium metal anode surface on SEI growth is investigated.

First, the newly developed three-electrode setup was tested by unidirectional plating and subsequent impedance spectroscopy. These measurements proved that the impedance of both half cells can be separated and the formation of pores on the stripping side can be measured. Moreover, the evolution of the overpotential of the cells was similar to that reported in the literature. Thus, the setup is suitable to study the Li|LPSCl interface.

Having proven this, the three-electrode setup was used to study the temporal evolution of the Li|LPSCl interface using differently treated lithium metal foils. One foil was freshly prepared and had no passivation layer. The other was a commercially available, 40 µm thick foil with a passivation layer at the surface. In both cases the LPSCl decomposes and an SEI is formed, however, the temporal SEI evolution differed significantly. The interphase growth of the cells with freshly fabricated lithium metal anodes is self-limiting, showing that a stable interphase is formed after a formation step. On the other hand, cells built with passivated lithium foil show higher interface resistances, and moreover, the SEI evolution of these cells is not self-limiting within the duration of the conducted experiments but continues to grow. While the interfacial resistance decreases with increasing cell pressure, the parabolic rate constant which is derived from the normalized resistance evolution increases. This is due to the increased penetration of the passivation layer, which enables more direct contact between lithium metal and SE and proves that the passivation layer inhibits lithium transfer.

This work provides fundamental insights into how the properties of the lithium anode affect cell performance as well as the kinetics of interfacial growth. This may prove to be an important aspect for long term stability. Unfortunately, the reason for the difference in SEI growth is not clear to date, but this work lays the foundation for further investigation. Nevertheless, this work suggests that reservoir-free cells may be more suitable for industrial applications, as they can contribute to the formation of favorable interphases that quickly saturate the resistance.

The experiments for this work were designed and planned by the first author under the supervision of F. H Richter and J. Janek. The cells were built by S. Mittelsdorf under the supervision of the first author. The first author performed the impedance measurements and analyzed the corresponding data. R. Rueß and F. H. Richter assisted with the scientific discussion of the impedance data. T. Fuchs performed the TIC and FIB-SEM measurements. The first author performed SEM and EDX measurements and data analysis. The manuscript was written by the first author and edited by four co-authors.

Reprinted with permission from Riegger, L. M.; Mittelsdorf, S.; Fuchs, T.; Rueß, R.; Richter, F. H.; Janek, J. Evolution of the Interphase between Argyrodite-based Solid Electrolytes and the Lithium Metal Anode – The Kinetics of Solid Electrolyte Interphases Growth. *Chemistry of Materials* **2023**, *35* (13), 5091-5099. DOI: 10.1021/acs.chemmater.3c00676. 

CHEMISTRY OF MATERIALS

pubs.acs.org/cm Article

# Evolution of the Interphase between Argyrodite-Based Solid Electrolytes and the Lithium Metal Anode—The Kinetics of Solid Electrolyte Interphase Growth

Luise M. Riegger, Sophie Mittelsdorf, Till Fuchs, Raffael Rueß, Felix H. Richter, and Jürgen Janek*

Cite This: https://doi.org/10.1021/acs.chemmater.3c00676 Read Online

ACCESS | Metrics & More | Article Recommendations | Supporting Information

**ABSTRACT:** Argyrodite-based solid electrolytes (SEs) are promising candidates for application in solid-state batteries (SSBs) due to their high ionic conductivity and mechanical malleability. However, they are reduced by lithium and form interphases when they are in contact with a lithium metal anode, which are needed to construct cells with high energy density. If the interphase is electronically insulating, a so-called solid electrolyte interphase (SEI) is formed that can protect the solid electrolyte from further degradation and grows only slowly. Careful evaluation of individual lithium metal anodelSE interface reactions and their growth kinetics is necessary to advance the concept of lithium metal batteries. Here, the interphase growth in symmetric Li|Li$_6$PS$_5$Cl|Li cells is studied quantitatively by impedance spectroscopy using a three-electrode cell setup. Unidirectional plating experiments show that the three-electrode cell is well suited to study the SEI evolution. Passivated and freshly prepared lithium foils are investigated, and the impedance evolution is studied to explore the influence of the lithium metal anode surface on SEI growth. The study reveals that an inherent passivation layer, present on most commercial lithium foils, influences the rate of SEI formation and causes high internal cell resistance. The lithium reservoir-free anode ("anode-free concept") is recommended to overcome the issues caused by chemically poorly defined lithium foil surfaces.

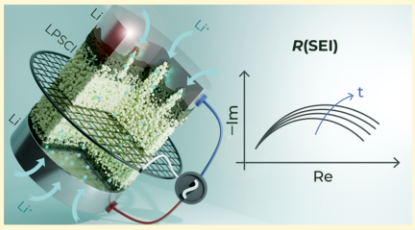


## INTRODUCTION

As the progress of solid-state battery (SSB) research approaches industrial application, the impact that more advanced components, such as lithium metal anodes (LMAs), have on cell performance is coming into focus.[1−3] Lithium metal anodes may be implemented to increase the energy and power densities of SSBs,[4] as lithium metal has a high theoretical capacity (3860 mAh g$^{-1}$) and a large negative potential (−3.06 V vs standard hydrogen electrode).[5,6] Unfortunately, lithium metal is highly reactive and decomposes most commonly used SEs that have high ionic conductivities, such as lithium argyrodites (Li$_6$PS$_5$X, X = Cl, Br, I), Li$_{10}$GeP$_2$S$_{12}$, or Li$_7$SiPS$_8$.[7−11] The "lithiation" of SEs forms either a "mixed conducting interphase" (MCI) or a "solid electrolyte interphase" (SEI), depending on the electronic conductivity of the formed products.[7−10,12,13] Wenzel et al. showed that lithium argyrodites decompose into a heterogeneous composite of binary compounds when they come into contact with lithium metal as follows:[8]

$$\mathrm{Li_6PS_5X} + 8\,\mathrm{Li} \rightarrow 5\,\mathrm{Li_2S} + \mathrm{Li_3P} + \mathrm{LiX},\ (\mathrm{X} = \mathrm{Cl, Br, I}) \quad (1)$$

As the decomposition products are electronically insulating or at least have very low electronic partial conductivity, an SEI is formed. The impedance evolution of symmetric Li|Li$_6$PS$_5$X|Li cells revealed that the SEI growth is diffusion-controlled and can be described by a Wagner-type model with the following equation:[8,14]

$$R(\mathrm{SEI}) = \frac{1}{A}\cdot\frac{\sigma_{\mathrm{el}}^{0.5}}{\sigma_{\mathrm{ion}}}\cdot\left(\frac{2\cdot M_{\mathrm{SEI}}\cdot\mu_{\mathrm{Li}}^{0}}{F^2\cdot\rho_{\mathrm{SEI}}\cdot x}\right)^{0.5}\cdot t^{0.5} = k'\cdot t^{0.5} \quad (2)$$

with $A$ as the macroscopic (geometric) electrode area, $\sigma_{\mathrm{el}}$ and $\sigma_{\mathrm{ion}}$ as the mean electronic and ionic partial conductivities of the SEI, $M_{\mathrm{SEI}}$ as the mean molar mass of the SEI, $\mu_{\mathrm{Li}}^{\circ}$ as the chemical potential of pure lithium metal, $F$ as the Faraday constant, $\rho_{\mathrm{SEI}}$ as the mean density of the SEI, $x$ as the stoichiometric factor of lithium metal consumption, the time $t$, and $k'$ as the parabolic rate constant of the interphase reaction.[8,14]

To form a suitable and stable and nonresistive SEI, its electronic partial conductivity should be low, while its ionic partial conductivity should be high.[8,14] Wenzel et al. reported that the Li|Li$_6$PS$_5$Cl interphase growth did not stop during a

Received: March 23, 2023
Revised: May 23, 2023





https://doi.org/10.1021/acs.chemmater.3c00676
Chem. Mater. XXXX, XXX, XXX−XXX

measurement time of 30 h.[8] Contrary to this, Otto et al. reported that the SEI growth on $Li_6PS_5Cl$ is self-limiting and leads to a layered SEI microstructure.[10] The authors also clarified the discrepancy between the SEI thickness measured by ToF-SIMS and the SEI thickness estimated earlier by Wenzel et al. from EIS results.[8,10] Despite these studies, the influence of the preparation method on the interphase growth is still unclear, as Otto et al. used vapor-deposited lithium metal and Wenzel et al. used commercial lithium foil, which typically is covered by a native passivation layer.[8,10]

Commercially available lithium foils are usually treated to form a uniform passivation layer that prevents side reactions of the lithium with its environment.[15−20] As lithium hydroxide (LiOH) and lithium carbonate ($Li_2CO_3$) form well-covering surface films, the passivation layer is mostly formed out of these compounds. In addition, the storage conditions (e.g., atmosphere in a dry room, glovebox, pouch container, etc.) influence the passivation layer composition due to reaction with residual gases, increasing the $Li_2CO_3$ content at the surface as well as the LiOH-rich and oxygen-rich regions within the layer.[16] The reactions with residual gases let the passivation layer generally grow thicker during storage of the commercial lithium foil.

The Li|SE interface resistance depends on the thickness and composition of the passivation layer of the lithium foil as well as on the surface roughness of the solid electrolyte, as this determines the intimacy of contact and contact area between lithium metal and the SE. With increasing pressure applied during cell construction, more solid electrolyte can mechanically penetrate the passivation layer of the lithium foil, which likely causes more SEI growth.[15] As $Li_6PS_5Cl$ immediately reacts when it comes into contact with lithium metal,[8,10] the passivation layer on the lithium metal anode as well as the contact pressure are expected to influence the SEI growth kinetics.

These considerations clearly mean that symmetric Li|SE|Li cells may well show two different Li|SE interfaces, and any direct current across the cell will increase the difference between both sides of the cell. In order to unequivocally measure the properties of a single electrode, the use of a reference electrode (RE) and the construction of a three-electrode cell are then mandatory. While three-electrode (3E) cells are well established for lithium-ion batteries,[21−23] there are only a few publications on 3E cells, including EIS measurements for SSBs.[24−27] A major reason for this is the difficult construction of a proper RE in the solid-state environment. Theoretical analyses of the influence of the RE position relative to the electrodes and the RE geometry on the respective cell impedances were published by Ivers−Tiffée and co-workers.[21,28,29] They reported that while a mesh-shaped RE might inhibit ion migration more than a wire-shaped RE, chemical and geometrical asymmetries have a smaller or no influence on the cell impedance.[21,28] Additionally, the higher surface area of a mesh, compared to that of a wire, lowers the impedance of the RE, and measurement artifacts caused by the RE may be less problematic.[30−32] However, as Simon et al. and Hertle et al. demonstrated with a $\mu$-sized wire-type RE, the proper separation of the two-electrode impedance works very well in SSBs and leads to consistent results.[27,33]

In this work, the influence of differently prepared lithium foils on the SEI growth kinetics is systematically studied, employing a three-electrode cell. A mesh-shaped In/InLi@Ni RE is used that has an open cross section of 83% and is coated with a 3.8 $\mu$m In/InLi coating to impede ion migration as little as possible.[28] Fresh lithium foil (f-Li) and commercially available—passivated—lithium foil (p-Li) are compared to investigate the influence of the different passivation layers of the commercially available LMA on SEI development. Additionally, the contact pressure is varied between 6.4 and 38.2 MPa for cells built with passivated lithium foil. The applied pressure influences the contact area and the amount of solid electrolyte that can penetrate through the passivation layer.[15] Thus, the applied pressure influences the area of direct contact between solid electrolyte and pure lithium metal, thereby changing the kinetics of SEI formation.

## EXPERIMENTAL SECTION

**Preparation of the Reference Electrode.** As the basis of the reference electrode, a nickel mesh (Goodfellow Cambridge Limited, GB) with a wire diameter of 41 $\mu$m and a nominal openness of 0.34 mm was used. 800 nm lithium (99.8%, ABCR Gambia, Germany) and subsequently 3 $\mu$m indium (99.999% ChemPur, Germany) were deposited on the mesh by thermal evaporation. After this dual deposition, the other side of the mesh was coated as well. The pressure of the deposition chamber was evacuated below $5 \times 10^{-6}$ mbar before the metals were deposited to prevent side reactions.

**Cell Preparation.** Cell preparation was carried out in an MBraun glovebox ($p(O_2)/p < 5$ pm, $p(H_2O)/p < 5$ pm). For this, a spacer was placed on one side of the coated mesh, and 100 mg of $Li_6PS_5Cl$ (NEI Corporation) was pressed at 3 t for 30 s (counter electrode (CE) side). Then, the spacer was removed, and an additional 100 mg of $Li_6PS_5Cl$ was put on the other side of the mesh and pressed for 30 s at 3 t as well (working electrode (WE) side). Afterward, lithium foil was brought into contact on the CE side. Lithium was plated on the reference with a current density of 118 $\mu A\ cm^{-2}$ using the geometric area of the lithium anode until the end of the potential plateau of the two-phase region In/InLi at 622 mV to ensure a maximum lithiation of the In/InLi RE. Due to overpotentials occurring during this lithiation step, the single-phase region InLi was not reached, but a high lithium content of the RE was secured. The lithium electrode of the WE side was then added.

Fresh lithium surfaces were prepared by pressing a piece of fresh lithium foil (Albemarle Corp.) within a pouch cell to obtain thinner foils with either a thickness of 60 or 100 $\mu$m. A disk with a diameter of 8 mm was punched out. Passivated lithium foil with a thickness of 40 $\mu$m was obtained from Honjo Metal Co., Ltd. (Japan) and used as received. A disk with a diameter of 9 mm was punched out. 12.7 MPa was applied to cells built with freshly prepared lithium foils. To study the pressure dependence of the SEI evolution, 6.4, 12.7, 19.1, and 38.2 MPa were applied to the cells built with passivated lithium during measurement.

**Electrochemical Tests.** To show that the mesh-shaped reference electrode does not interfere with cycling, lithium was plated from the WE to the CE with a current density of 0.10 ma $cm^{-2}$ using the geometric area of the lithium anode in 1 h steps for 15 h of plating in total. Before plating lithium as well as after each plating step, an impedance measurement was conducted. The cells were equilibrated for 30 min before each impedance measurement. Impedance was measured in a climate chamber at 25 °C using a Biologic VMP 300 potentiostat (BioLogic, France). An amplitude of 5 mV was applied within a frequency range between 2 MHz and 100 MHz. For the first 2 h, cell impedance was measured every 15 min, for the next 10 h every 30 min, and thereafter, impedance was measured every hour to ensure that an adequate number of data points is acquired.

**Scanning Electron Microscopy (SEM) and Energy-Dispersive Spectroscopy (EDS) Measurements.** Focused ion beam (FIB)-cutting was carried out using a XEIA3 GMU SEM/Plasma-FIB (Tuscan) in combination with a cry-stage at −140 °C. The reference mesh was also cut using an ion beam milling system (Luca EM TIC 3X). For this, argon ions with an acceleration voltage of 6 kV and a current of 2.2 mA were used. To reduce alterations of the sample,



https://doi.org/10.1021/acs.chemmater.3c00676
Chem. Mater. XXXX, XXX, XXX−XXX

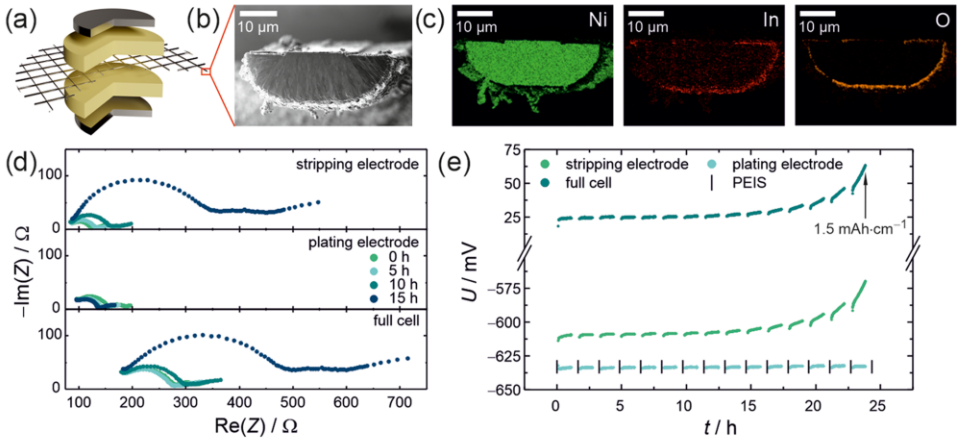


**Figure 1.** (a) Schematic of a symmetric three-electrode LilLi$_6$PS$_5$ClIn/InLi@NilLi$_6$PS$_5$ClLi-cell with an In/InLi reference electrode Ni mesh in the center. (b) SEM image and (c) corresponding nickel, indium, and oxygen EDX maps of the reference electrode cross section after deposition of 0.8 $\mu$m of lithium and 3 $\mu$m of indium with vapor deposition. (d) Impedance evolution and (e) overpotential evolution of the respective half-cells (stripping and plating electrode) and the full cell during 15 h of unidirectional stripping.

sample milling was carried out at −140 °C using liquid nitrogen cooling.

A Merlin ultra-field emission scanning electron microscopy (SEM) instrument from Carl Zeiss (Germany) was used to study the coating of the reference mesh. EDS measurements were carried out with an X-Max Extreme silicon drift detector (Oxford Instruments). All sample transfers were carried out by using a Luca transfer module system (EM VCT500, Luca, Germany) to avoid contact of the oxygen and moisture-sensitive mesh with air.

**Surface Roughness Measurements.** A profilometer ($\alpha$-Step IQ surface profiler, KLA Tencor) in an MBraun glovebox ($p(O_2)/p < 5$ ppm, $p(H_2O)/p < 5$ ppm) was used to determine the surface roughness of the $Li_6PS_5Cl$ pellets. A scan length of 500 $\mu$m each was measured, and the profiles were leveled by setting two zones to the same average height. The roughness parameter $R_a$ value was calculated from the leveled profiles, and the given value is the average of three determined $R_a$ values.

## ■ RESULTS AND DISCUSSION

**Validation of 3E Cell Design by Unidirectional Stripping.** Cell cycling experiments were conducted to verify if the mesh-shaped RE is well suited for analyzing the impedance of half-cells. For this, the effect of lithium stripping or plating on the impedance evolution was investigated separately in each half-cell. The reference electrodes were placed in the center of the solid electrolyte separators (Figure 1a). A stepwise assembly of the $Li_6PS_5Cl$ on each side of the reference electrode was necessary to ensure complete contact between the $Li_6PS_5Cl$ separator and mesh. This way, symmetrical LilLi$_6$PS$_5$ClIn/InLi@NilLi$_6$PS$_5$ClLi cells were assembled (see the Experimental Section). Lithium was then plated in 1 h steps with a current density of 0.1 mA cm$^{-2}$ from the stripping electrode (WE) to the plating electrode (CE). After a waiting step of 30 min, PEIS was measured (Figure 1e). The total duration of plating was 15 h.

A cross-sectional image of the used reference mesh shows the expected core−shell structure (Figure 1b). The nickel core that gives the RE its structural stability is surrounded by the deposited indium. EDS mapping (Figure 1c) confirms that the nickel core is covered by indium. Oxygen is enriched as well, which indicates that lithium has partly reacted with oxygen during the vapor deposition or cross section preparation. However, a stable potential of 622 mV vs Li$^+$/Li between RE and the electrodes was measured in the symmetrical cells. Thus, the In/InLi$_x$ layer has indeed a composition $0 < x \leq 1$, even though lithium metal cannot be detected by EDS.

Unfortunately, sputter damage occurred during preparation of the cross section as can be seen by the redeposition of nickel on the outside and a thin indium cover on the flat part of the nickel mesh. A cross section prepared by a focused ion beam with lower energy and without sputter damage can be found in the Supporting Information Figure S1. This SEM image shows a uniform layer of In/InLi$_x$ ($0 < x \leq 1$) covering the nickel mesh. EDX measurements were not possible for this sample due to geometrical constraints within the instrument.

Figure 1d shows the impedance evolution of a symmetric LilLi$_6$PS$_5$ClIn/InLi@NilLi$_6$PS$_5$ClLi-cell. The impedances of the stripping and plating electrodes should be identical in a symmetric cell before plating (0 h); however, there are small differences. The differences in absolute impedance of each half-cell (146 vs 196 Ω for the stripping and plating electrodes, respectively) are most likely caused by a different contact area due to a nonideal interface between the lithium electrodes and the solid electrolyte. Thus, pores were already present before starting the measurement, leading to current focusing at the interface during stripping.

The impedance during stripping and plating is influenced by changes in the interface morphology. If the time constant of the constriction signal is smaller than the time constants of transport processes, e.g., ionic transport within the bulk, grain boundaries or SEI, the respective impedance response is influenced by the geometric restriction.[34,35] Thus, the impedance during stripping and plating is influenced by changes in the interface morphology in addition to impedance growth due to SEI formation, which complicates data evaluation. For this reason, no fit is shown for the stripping/plating experiment in Figure 1d. By implementing a reference electrode, the influence of geometrical restrictions can be reduced as the studied impedance response is measured for a single half-cell.



https://doi.org/10.1021/acs.chemmater.3c00676
Chem. Mater. XXXX, XXX, XXX−XXX

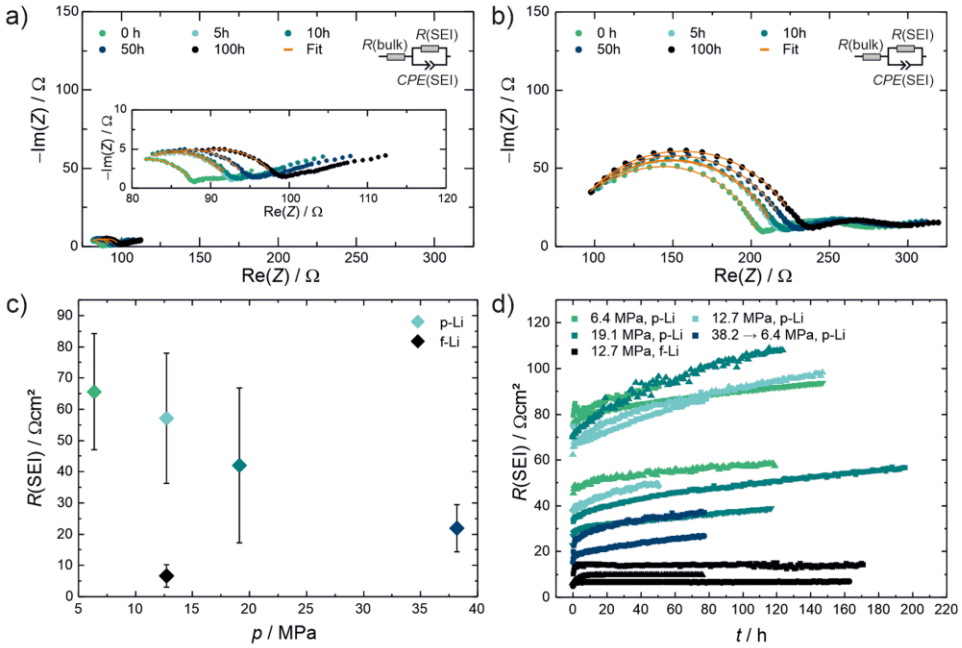


**Figure 2.** Nyquist plots of the impedance response of the WEs directly after measurement start, and after 5, 10, 50, and 100 h of contact at open circuit conditions using (a) fresh lithium metal and (b) passivated lithium foil. The data were fitted with the shown equivalent circuit. (c) Measured SEI resistances directly after measurement start as a function of the applied pressure. (d) Evolution of the SEI resistance $R$(SEI) for the cell measured at 6.4, 12.7, 19.1, and 38.2 MPa (f-Li is shown in black, p-Li in color).

The impedance of the stripping electrode increases during lithium dissolution. This is caused by growing pores at the interface, further decreasing the contact area between the lithium metal anode and the SE.[36] The overpotential at the stripping electrode slightly increases during the first 7 h of stripping (0.7 mAh $cm^{-2}$, see Figure 1e), as there is no severe contact loss yet because pores grow three-dimensionally due to a faster lithium diffusion along the pore surface.[26,36] For longer stripping times (1.5 mAh $cm^{-2}$), pore formation leads to contact loss, which increases the interface resistance and, thus, the overpotential.[26,36] A similar stripping capacity at contact loss was reported by Krauskopf et al. for Li|$Li_7La_3Zr_2O_{12}$ interfaces, showing that the contact loss is primarily due to the morphological instability of the LMA.[36]

At the plating electrode, the impedance decreases during 15 h of lithium deposition. This is caused by plating lithium into the pores between the solid electrolyte and the lithium metal anode, increasing the contact area. However, the SEI is simultaneously formed at the newly filled sites as lithium readily reacts with $Li_6PS_5Cl$, which increases the impedance. While both processes happen simultaneously, the area increase has a bigger influence, hence, the decrease in impedance overall. The change of the overpotential is minor during lithium plating. Altogether, the measured impedance response and overpotential evolution of the cell during unidirectional lithium plating shows that the used 3E setup is well suited to separate the impedances of both half-cells.

**Time-Dependent SEI Growth When Using Different Foils and Pressures.** The chemical decomposition of the Li|SE interface is studied at open circuit conditions without additional cycling that otherwise might change the constriction contribution of the interface. Thus, the influence of pores and the resulting geometrical constriction were kept to a minimum throughout the measurement. Since the cells are not cycled in the further course of the paper, the electrodes under investigation will be referred to below as the working electrode and no longer as the stripping electrode. The molar volume of the SEI compounds, however, is smaller than the molar volumes of the stoichiometric amounts of lithium and $Li_6PS_5Cl$, see Table S1. Thus, possible pore formation caused by the interface reaction cannot be prevented and may influence the impedance measurement, especially the obtained capacitances.

The kinetics of the interphase evolution between $Li_6PS_5Cl$ and lithium metal (without DC current) was studied using impedance spectroscopy. For this, symmetric Li|$Li_6PS_5Cl$|In/InLi@Ni|$Li_6PS_5Cl$|Li cells were assembled, and the impedance evolution was measured. For the first 2 h, cell impedance was measured every 15 min, for the next 10 h every 30 min, and thereafter, impedance was measured every hour to ensure that an appropriate number of data points is acquired. The corresponding Nyquist plots directly after measurement start (0 h) and after 5, 10, 50, and 100 h can be found in Figure 2a,b for exemplary cells built with fresh and passivated lithium metal anodes and a contact pressure of 12.7 MPa, respectively.

The element $R$(bulk) describes the transport process in the bulk. The impedance of the forming SEI is described using parallel $R$(SEI)−CPE(SEI) (constant phase element) elements. The transport of $Li^+$ ions through the passivation layer is described by the same $R$(SEI)−CPE(SEI) element due to apparently comparable $Li^+$ ion conductivities of its compounds ($Li_2CO_3$, LiOH, and $Li_2O$) and the SEI compounds ($Li_2S$, $Li_3P$, and LiCl).[37−40] Both bulk- and SEI-related elements are



https://doi.org/10.1021/acs.chemmater.3c00676
Chem. Mater. XXXX, XXX, XXX−XXX

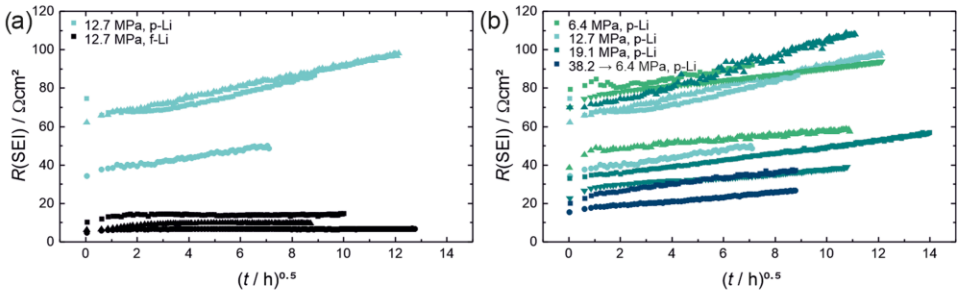


**Figure 3.** Temporal evolution of the SEI resistance $R$(SEI) plotted against the square root of time for cells (a) built with passivated (p-Li, blue) and fresh lithium foil (f-Li, black) applied at 12.7 MPa, and (b) built with p-Li but applied at 6.4, 12.7, 19.1, and 38.2 MPa.

connected in series. As the SEI evolution is studied in this work, only the high and middle frequency ranges were fitted.

For better legibility, the first resistance values after measurement start are shown in Figure 2c. The overall resistance decreases with increasing pressure as the higher pressure increases the contact area between solid electrolyte and lithium metal anode due to more plastic deformation.[36,41] Interestingly, the resistances of the p-Li cells are higher than those of the f-Li cells, even though the same cell parameters were used. This can also be seen in Figure 2d, which shows the temporal evolution of the SEI resistances for $Li_6PS_5Cl$|p-Li (shown in color) and $Li_6PS_5Cl$|f-Li (shown in black). The difference of the SEI resistances is clearly caused by the passivation layer on the commercial lithium foil as it has similar conductivities as the SEI,[37,38] and thus, adds to the Li|SE interphase resistance.

Comparing the absolute resistance values of similar cells shows that they strongly vary even when the cell parameters are the same. As this variation is seen both for f-Li and p-Li cells, respectively, it is most likely caused by variations in contact area due to nonideally planar interfaces as especially the lithium foil is not ideally flat before application.[36] Additionally, the interphase resistances for p-Li cells could be influenced by changes of the passivation layer due to storage of the p-Li foil. Otto et al. recently showed that the properties of the passivation layer are strongly influenced by the storage conditions and storage time.[15] Different layer compositions can cause different local lithium-ion conductivities, and a variation in the passivation layer thickness can change the degree of solid electrolyte penetrating through the passivation layer.

**Mechanistic Understanding of the Results.** As the growth of interphase resistances follows a parabolic rate law (caused by diffusion control),[8,14] the SEI resistances are plotted against the square root of time and show a linear evolution in that depiction, see Figure 3a,b. The resistance evolutions of p-Li and f-Li cells show a different time dependence. For f-Li cells (shown in black), a diffusion-controlled growth is observed up to approximately 9 h of contact time. Thereafter, the SEI resistance shows only minimal dependence on contact time. Thus, the interphase reaction is self-limiting when a fresh lithium foil is used and stops once a certain layer thickness is reached. This had also been observed with time-of-flight secondary-ion mass-spectrometry (ToF-SIMS) measurements of Li|$Li_6PS_5Cl$ interfaces that had been prepared by evaporating lithium metal on the SE.[10]

The long-term evolution of the SEI resistance for the passivated lithium metal anode (Figure 3b) has a square root time dependence for contact times of above 4 h. For contact times up to 4 h, there are deviations from diffusion-controlled growth. These might be caused by an interface-controlled reaction after bringing the solid electrolyte and the lithium metal into contact.[8,14] For long contact times, however, there is no deviation from the parabolic law, revealing that the diffusion-controlled growth is not self-limiting within the measured time frame for passivated LMAs.

The passivation layer apparently influences the growth kinetics. Several explanations are conceivable for this. This inhibition is caused by components with low lithium-ion conductivity, such as LiOH or $Li_2O$ slowing down the growth kinetics. If this is the case, a stable interphase should be reached eventually, even though it is beyond the duration of these measurements.

Another possible explanation is that the formed SEI microstructure is different for p-Li compared to f-Li and that this could influence the electronic percolation pathways. The Li−O compounds of the passivation layer have lower electronic bulk conductivities than the $Li_3P$ formed upon decomposition.[37−40] For this reason, the electronic conductivity is probably not increased by the higher proportion of Li−O components in p-Li interfaces. However, the ongoing reaction might suggest an increased electronic conductivity that is detrimental for cell performance.

For LIB, space charge accumulation at the LiF|$Li_2CO_3$ interface has been suggested to increase the $Li^+$-ion conductivity and decrease the electronic conductivity,[42−44] even though the bulk conductivities remain the same. Here, we speculate that a similar effect may occur at heterogeneous Li|SE interfaces formed during lithium plating in reservoir-free cells or during cycling. However, in the case observed here, the electrical conductivity would be increased by the space charge layer.

If the Li|SE interface is prepared by vapor deposition of lithium metal, a layered but laterally homogeneous microstructure is observed.[10] However, if Li is plated onto the surface, a more mosaic-like structure can be seen,[45] which is also known for LIBs.[46,47] The SEI of the f-cells will resemble the interface produced by evaporation, as the lithium and electrolyte are in direct contact with each other. However, for cells built with p-Li, the contact might be more mosaic-like due to the penetration of the passivation layer by the electrolyte. These pathways could allow continuous diffusion for cells built with a mosaic-like SEI, and thus, continuous SEI formation is observed. However, future work is needed to investigate this



https://doi.org/10.1021/acs.chemmater.3c00676
Chem. Mater. XXXX, XXX, XXX−XXX

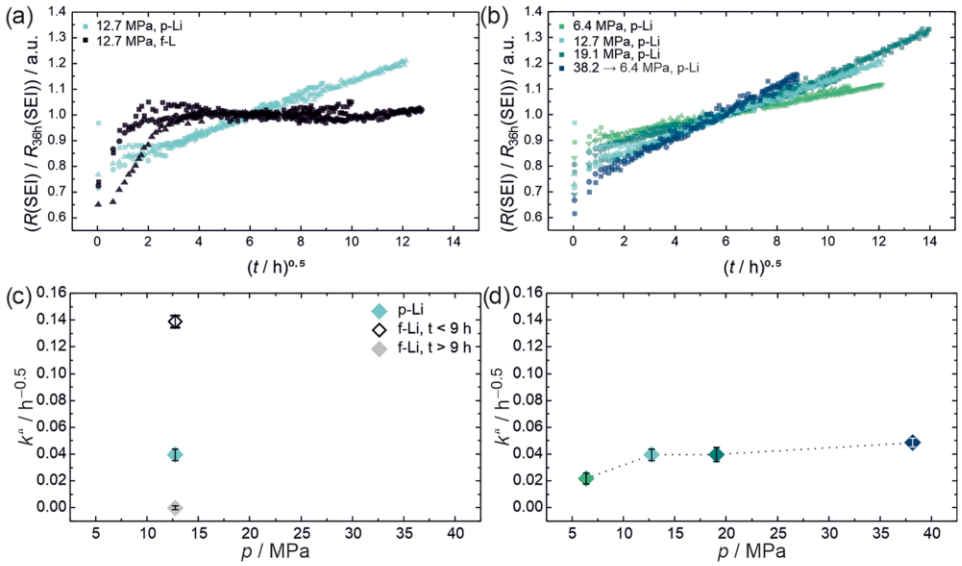


**Figure 4.** Temporal evolution of the SEI resistance normalized to the value of $R$(SEI) after 36 h and plotted against the square root of time for cells (a) built with p-Li and f-Li applied at 12.7 MPa, and (b) built with p-Li but applied at different pressures. Parabolic rate constants $k''$ of the normalized SEI resistances and plotted against the applied pressure for cells (c) built with p-Li and f-Li applied at 12.7 MPa, and (d) built with p-Li but applied at different pressures.

possibility more thoroughly, and we refrain from speculation at this point.

Wenzel et al. described the temporal resistance evolution using eq 2.[8,14] The resulting parabolic rate constants $k'$ of the f-Li and p-Li cells are determined by using Figure 3a,b and can be seen in Figure S2 as a function of contact pressure. All rate constants $k'$, both for f-Li and p-Li cells, show a strong variation that is caused by the variation of the resistance evolution of the different cells (Figure 2). Interestingly, cells with a higher initial resistance $R_0$(SEI) also have a higher parabolic rate constant $k'$ independent of the respective contact pressure, see Table S2. If the LilSE contact area decreases, $R_0$(SEI) increases as well as the effective pressure at the interface of the solid electrolyte and the lithium metal. As the surface roughness of the used SE pellets is about 60 nm with a maximal variation in height of 1.5 $\mu$m, the solid electrolyte will penetrate the passivation layer of the commercial lithium foil.[15,41] With higher pressure, more direct points of contact between solid electrolyte and pure lithium metal are formed, and thus, the growth rate is increased.

The SEI resistances of cells built with the same type of lithium foil show similar changes over time. Therefore, they were normalized to become independent of the contact area between the solid electrolyte and the lithium electrode, which determines the absolute resistance values, see Figure 4a,b. Thus, the scattering of values of cells with identical treatment becomes minor, allowing a comparison of the different temporal resistance evolutions.

Even though the normalized values are independent of the contact area, the slopes for the p-Li cells (Figure 4b) are influenced by the applied pressure. With increasing pressure, the slope of the temporal evolution increases. If a higher pressure is used during lithium application, more electrolyte can penetrate the passivation layer of the lithium foil.[15,41] Thus, more solid electrolyte comes into direct contact with lithium metal. With an increasing number of contact points between solid electrolyte and lithium metal, the SEI grows faster. Therefore, the slope is higher for higher cell pressures.

For normalization, the respective value after 36 h of contact time $R_{36\,h}$(SEI) was chosen instead of the initial value since there are still deviations from diffusion-controlled growth at the beginning of measurement. The parabolic rate constant $k''$ of the normalized resistances was determined with the following equation:

$$\frac{R(\mathrm{SEI})}{R_{36h}(\mathrm{SEI})} = k''\cdot t^{0.5} \tag{3}$$

$k''$ can be determined using Figure 4a,b and is plotted against its respective cell pressure in Figure 4c,d.

For f-Li cells, $k'' \approx 0.14\ \mathrm{h}^{-0.5}$ in the diffusion-controlled regime ($t < 9$ h) and $k'' < 1 \times 10^{-3}\ \mathrm{h}^{-0.5}$ for the self-limited regime ($t > 9$ h). So, even if $Li_6PS_5Cl$ reacts quickly with lithium metal, the reaction rate is significantly reduced once a certain layer thickness has formed. Thus, a first formation step in reservoir-free cells may form and stable interphase resistance with $R$(SEI) < 20 Ω. If lithium loss during first charging in reservoir-free cells needs to be reduced, depositing a thin lithium film on the solid electrolyte separator, e.g., by vapor deposition, could form a stable interphase. Alternatively, the application of lithium can be achieved by vapor deposition instead of a role-to-role process with a commercially available lithium foil, usually containing a passivated surface, to reduce its reactivity. In any case, the lithium loss due to SEI formation of sulfide-type separators needs to be taken into account when considering "anode-free" cell concepts.

The influence of pressure on the parabolic rate constant of the normalized SEI resistances $k''$ for p-Li cells can be identified easily. The parabolic rate constant increases from ~0.022 $\mathrm{h}^{-0.5}$ for a contact pressure of 6.4 MPa to ~0.048 $\mathrm{h}^{-0.5}$ for a contact pressure of 38.2 MPa (Figure 4d). As stated



https://doi.org/10.1021/acs.chemmater.3c00676
Chem. Mater. XXXX, XXX, XXX−XXX

above, the reason for this pressure dependence is the increasing number of contact points between the solid electrolyte and pure lithium, accelerating SEI growth, which is highest for the f-LilSE contact. The increase of the rate constants with pressure shows that an interlayer between the solid electrolyte and the lithium metal anode can decrease the interphase reaction. As long as it can inhibit LilSE contact, an artificial interlayer can inhibit SEI formation. However, the conventional passivation layer on lithium foils is not suitable, as the overall resistance is higher than for a lithium foil without a passivating layer.

## ■ CONCLUSIONS

In this work, we demonstrate that the SEI evolution of $Li_6PS_5Cl$ depends on the composition and layer thickness of the surface passivation film on the used lithium metal anode. If lithium with a freshly prepared surface is used, an SEI is quickly formed within the first 9 h of contact time. This interphase growth is self-limiting, showing that a stable interphase is formed after a formation step. On the other hand, cells built with passivated lithium foil show higher interface resistances compared to f-Li cells due to the passivation layer. In addition, the SEI evolution of cells built with passivated lithium foil is not self-limiting within the duration of the conducted experiments but continues to grow. The parabolic rate constants were determined for the resistance evolution as well as the normalized resistance evolution to derive the influence of the cell pressure. Increasing the cell pressure allows more solid electrolyte to penetrate the passivation layer, resulting in a higher number of contact points. As the contact area between lithium metal and solid electrolyte rises, the parabolic growth rate increases as well. We show that the inherent passivation layer of commercial lithium foils hinders proper lithium transfer and is detrimental to cell performance. Thus, reservoir-free cells, in which lithium metal is plated in situ, are more promising to obtain low and stable interface resistances in SSBs with an argyrodite-type solid electrolyte separator.

## ■ ASSOCIATED CONTENT

### Supporting Information

The Supporting Information is available free of charge at https://pubs.acs.org/doi/10.1021/acs.chemmater.3c00676.

SEM image of the reference electrode cross section prepared by FIB cutting; calculated molar volume changes for the reaction of $Li_6PS_5Cl$ with Li metal; parabolic rate constants $k'$ of the SEI resistances shown as figure and table (PDF)

## ■ AUTHOR INFORMATION


### Corresponding Author

**Jürgen Janek** − *Institute of Physical Chemistry, Justus-Liebig-University Giessen, D-35392 Giessen, Germany; Center for Materials Research (ZfM), Justus-Liebig-University Giessen, D-35392 Giessen, Germany;* orcid.org/0000-0002-9221-4756; Email: Juergen.Janek@phys.Chemie.uni-giessen.de

### Authors

**Luise M. Riegger** − *Institute of Physical Chemistry, Justus-Liebig-University Giessen, D-35392 Giessen, Germany; Center for Materials Research (ZfM), Justus-Liebig-University Giessen, D-35392 Giessen, Germany*

**Sophie Mittelsdorf** − *Institute of Physical Chemistry, Justus-Liebig-University Giessen, D-35392 Giessen, Germany; Center for Materials Research (ZfM), Justus-Liebig-University Giessen, D-35392 Giessen, Germany*

**Till Fuchs** − *Institute of Physical Chemistry, Justus-Liebig-University Giessen, D-35392 Giessen, Germany; Center for Materials Research (ZfM), Justus-Liebig-University Giessen, D-35392 Giessen, Germany*

**Raffael Rueß** − *Institute of Physical Chemistry, Justus-Liebig-University Giessen, D-35392 Giessen, Germany; Center for Materials Research (ZfM), Justus-Liebig-University Giessen, D-35392 Giessen, Germany*

**Felix H. Richter** − *Institute of Physical Chemistry, Justus-Liebig-University Giessen, D-35392 Giessen, Germany; Center for Materials Research (ZfM), Justus-Liebig-University Giessen, D-35392 Giessen, Germany;* orcid.org/0000-0002-6587-7757

Complete contact information is available at: https://pubs.acs.org/10.1021/acs.chemmater.3c00676


### Notes

The authors declare no competing financial interest.

## ■ ACKNOWLEDGMENTS

This work was partly funded by the German Federal Ministry of Education and Research (BMBF) within the project "FESTBATT," grant identifier 03XP0177A, 03XP0177D, and 03XP0430A, and within the project "InCa-2" (03XP0472A). The authors greatly appreciate helpful discussions with S. Burkhardt. The authors further thank Elisa Monte for her support for the preparation of the ToC image.

## ■ REFERENCES


(1) Bindra, A. Electric Vehicle Batteries Eye Solid-State Technology: Prototypes Promise Lower Cost, Faster Charging, and Greater Safety. *IEEE Power Electron. Mag.* **2020**, *7*, 16−19.

(2) Schmaltz, T.; Wicke, T.; Weymann, L.; Voß, P.; Neef, C.; Thielmann, A. *Solid-State Battery Roadmap 2035+* DOI: 10.24406/PUBLICA-68. (accessed 2022-11-25).

(3) Janek, J.; Zeier, W. G. Challenges in Speeding Up Solid-state Battery Development. *Nat. Energy* **2023**, *8*, 230−240.

(4) Janek, J.; Zeier, W. G. A Solid Future for Battery Development. *Nat. Energy* **2016**, *1*, 16141.

(5) Hatzell, K. B.; Chen, X. C.; Cobb, C. L.; Dasgupta, N. P.; Dixit, M. B.; Marbella, L. E.; McDowell, M. T.; Mukherjee, P. P.; Verma, A.; Viswanathan, V.; Westover, A. S.; Zeier, W. G. Challenges in Lithium Metal Anodes for Solid-State Batteries. *ACS Energy Lett.* **2020**, *5*, 922−934.

(6) Krauskopf, T.; Dippel, R.; Hartmann, H.; Peppler, K.; Mogwitz, B.; Richter, F. H.; Zeier, W. G.; Janek, J. Lithium-Metal Growth Kinetics on LLZO Garnet-Type Solid Electrolytes. *Joule* **2019**, *3*, 2030−2049.

(7) Wenzel, S.; Randau, S.; Leichtweiß, T.; Weber, D. A.; Sann, J.; Zeier, W. G.; Janek, J. Direct Observation of the Interfacial Instability of the Fast Ionic Conductor $Li_{10}GeP_2S_{12}$ at the Lithium Metal Anode. *Chem. Mater.* **2016**, *28*, 2400−2407.

(8) Wenzel, S.; Sedlmaier, S. J.; Dietrich, C.; Zeier, W. G.; Janek, J. Interfacial Reactivity and Interphase Growth of Argyrodite Solid Electrolytes at Lithium Metal Electrodes. *Solid State Ionics* **2018**, *318*, 102−112.

(9) Riegger, L. M.; Otto, S.-K.; Sadowski, M.; Jovanovic, S.; Kötz, O.; Harm, S.; Balzat, L. G.; Merz, S.; Burkhardt, S.; Richter, F. H.; Sann, J.; Eichel, R.-A.; Lotsch, B. V.; Granwehr, J.; Albe, K.; Janek, J. Instability of the $Li_7SiPS_8$ Solid Electrolyte at the Lithium Metal




https://doi.org/10.1021/acs.chemmater.3c00676
Chem. Mater. XXXX, XXX, XXX−XXX

Anode and Interphase Formation. *Chem. Mater.* **2022**, *34*, 3659−3669.
(10) Otto, S.-K.; Riegger, L. M.; Fuchs, T.; Kayser, S.; Schweitzer, P.; Burkhardt, S.; Henss, A.; Janek, J. In Situ Investigation of Lithium Metal−Solid Electrolyte Anode Interfaces with ToF-SIMS. *Adv. Mater. Interfaces* **2022**, *9*, No. 2102387.
(11) Gibson, J. S.; Narayanan, S.; Swallow, J. E. N.; Kumar-Thakur, P.; Pasta, M.; Lee, T.-L.; Weatherup, R. S. Gently Does It!: In Situ Preparation of Alkali Metal-solid Electrolyte Interfaces for Photoelectron Spectroscopy. *Faraday Discuss.* **2022**, *236*, 267−287.
(12) Riegger, L. M.; Schlem, R.; Sann, J.; Zeier, W. G.; Janek, J. Lithium-Metal Anode Instability of the Superionic Halide Solid Electrolytes and the Implications for Solid-State Batteries. *Angew. Chem., Int. Ed.* **2021**, *60*, 6718−6723.
(13) Wenzel, S.; Leichtweiss, T.; Krüger, D.; Sann, J.; Janek, J. Interphase Formation on Lithium Solid Electrolytes - An In Situ Approach to Study Interfacial Reactions by Photoelectron Spectroscopy. *Solid State Ionics* **2015**, *278*, 98−105.
(14) Wenzel, S. Thermodynamic and kinetic instability of inorganic solid electrolytes at lithium and sodium metal electrodes, PhD thesis; Justus-Liebig-University Giessen: Giessen, 2016.
(15) Otto, S.-K.; Fuchs, T.; Moryson, Y.; Lerch, C.; Mogwitz, B.; Sann, J.; Janek, J.; Henss, A. Storage of Lithium Metal: The Role of the Native Passivation Layer for the Anode Interface Resistance in Solid State Batteries. *ACS Appl. Energy Mater.* **2021**, *4*, 12798−12807.
(16) Otto, S.-K.; Moryson, Y.; Krauskopf, T.; Peppler, K.; Sann, J.; Janek, J.; Henss, A. In-Depth Characterization of Lithium-Metal Surfaces with XPS and ToF-SIMS: Toward Better Understanding of the Passivation Layer. *Chem. Mater.* **2021**, *33*, 859−867.
(17) Schmuch, R.; Wagner, R.; Hörpel, G.; Placke, T.; Winter, M. Performance and Cost of Materials for Lithium-based Rechargeable Automotive Batteries. *Nat. Energy* **2018**, *3*, 267−278.
(18) Acebedo, B.; Morant-Miñana, M. C.; Gonzalo, E.; Ruiz de Larramendi, I.; Villaverde, A.; Rikarte, J.; Fallarino, L. Current Status and Future Perspective on Lithium Metal Anode Production Methods. *Adv. Energy Mater.* **2023**, *13*, No. 2203744.
(19) Wietelmann, U. Oberflächenpassiviertes Lithiummetall und Verfahren zu dessen Herstellung. WO2011/073324 A1, 2011.
(20) Wietelmann, U.; Hartnig, C.; Emmel, U.; Nickel, V. Stabilisierte mit einer stickstoffhaltigen Schale beschichtete Lithiummetallabformungen und Verfahren zu deren Herstellung. WO2014/170429 A1, 2014.
(21) Costard, J.; Ender, M.; Weiss, M.; Ivers-Tiffée, E. Three-Electrode Setups for Lithium-Ion Batteries. *J. Electrochem. Soc.* **2017**, *164*, A80−A87.
(22) Jansen, A. N.; Dees, D. W.; Abraham, D. P.; Amine, K.; Henriksen, G. L. Low-temperature Study of Lithium-ion Cells Using a $Li_ySn$ Micro-reference Electrode. *J. Power Sources* **2007**, *174*, 373−379.
(23) Zhou, J.; Notten, P. H. L. Development of Reliable Lithium Microreference Electrodes for Long-Term *In Situ* Studies of Lithium-Based Battery Systems. *J. Electrochem. Soc.* **2004**, *151*, A2173.
(24) Dugas, R.; Dupraz, Y.; Quemin, E.; Koç, T.; Tarascon, J.-M. Engineered Three-Electrode Cells for Improving Solid State Batteries. *J. Electrochem. Soc.* **2021**, *168*, 090508.
(25) Ikezawa, A.; Fukunishi, G.; Okajima, T.; Kitamura, F.; Suzuki, K.; Hirayama, M.; Kanno, R.; Arai, H. Performance of $Li_4Ti_5O_{12}$-based Reference Electrode for the Electrochemical Analysis of All-solid-state Lithium-ion Batteries. *Electrochem. Commun.* **2020**, *116*, No. 106743.
(26) Wang, M. J.; Choudhury, R.; Sakamoto, J. Characterizing the Li-Solid-Electrolyte Interface Dynamics as a Function of Stack Pressure and Current Density. *Joule* **2019**, *3*, 2165−2178.
(27) Hertle, J.; Walther, F.; Mogwitz, B.; Schröder, S.; Wu, X.; Richter, F. H.; Janek, J. Miniaturization of Reference Electrodes for Solid-State Lithium-Ion Batteries. *J. Electrochem. Soc.* **2023**, *170*, 040519.
(28) Ender, M.; Illig, J.; Ivers-Tiffée, E. Three-Electrode Setups for Lithium-Ion Batteries. *J. Electrochem. Soc.* **2017**, *164*, A71−A79.
(29) Ender, M.; Weber, A.; Ellen, I.-T. Analysis of Three-Electrode Setups for AC-Impedance Measurements on Lithium-Ion Cells by FEM simulations. *J. Electrochem. Soc.* **2011**, *159*, A128−A136.
(30) Chechirlian, S.; Eichner, P.; Keddam, M.; Takenouti, H.; Mazille, H. A Specific Aspect of Impedance Measurements in Low Conductivity Media. Artefacts and Their Interpretations. *Electrochim. Acta* **1990**, *35*, 1125−1131.
(31) Fletcher, S. The Two-terminal Equivalent Network of a Three-terminal Electrochemical Cell. *Electrochem. Commun.* **2001**, *3*, 692−696.
(32) Sadkowski, A.; Diard, J.-P. On the Fletcher's Two-terminal Equivalent Network of a Three-terminal Electrochemical Cell. *Electrochim. Acta* **2010**, *55*, 1907−1911.
(33) Simon, F. J.; Blume, L.; Hanauer, M.; Sauter, U.; Janek, J. Development of a Wire Reference Electrode for Lithium All-Solid-State Batteries with Polymer Electrolyte: FEM Simulation and Experiment. *J. Electrochem. Soc.* **2018**, *165*, A1363−A1371.
(34) Eckhardt, J. K.; Fuchs, T.; Burkhardt, S.; Klar, P. J.; Janek, J.; Heiliger, C. 3D Impedance Modeling of Metal Anodes in Solid-State Batteries-Incompatibility of Pore Formation and Constriction Effect in Physical-Based 1D Circuit Models. *ACS Appl. Mater. Interfaces* **2022**, *14*, 42757−42769. Published Online: Sep. 8, 2022.
(35) Eckhardt, J. K.; Klar, P. J.; Janek, J.; Heiliger, C. Interplay of Dynamic Constriction and Interface Morphology between Reversible Metal Anode and Solid Electrolyte in Solid State Batteries. *ACS Appl. Mater. Interfaces* **2022**, *14*, 35545−35554. Published Online: Jul. 25, 2022.
(36) Krauskopf, T.; Hartmann, H.; Zeier, W. G.; Janek, J. Toward a Fundamental Understanding of the Lithium Metal Anode in Solid-State Batteries-An Electrochemo-Mechanical Study on the Garnet-Type Solid Electrolyte $Li_{6.25}Al_{0.25}La_3Zr_2O_{12}$. *ACS Appl. Mater. Interfaces* **2019**, *11*, 14463−14477.
(37) Biefeld, R. M.; Johnson, R. T. Ionic Conductivity of $Li_2O$ - Based Mixed Oxides and the Effects of Moisture and LiOH on Their Electrical and Structural Properties. *J. Electrochem. Soc.* **1979**, *126*, 1−6.
(38) Shi, S.; Qi, Y.; Li, H.; Hector, L. G. Defect Thermodynamics and Diffusion Mechanisms in $Li_2CO_3$ and Implications for the Solid Electrolyte Interphase in Li-Ion Batteries. *J. Phys. Chem. C* **2013**, *117*, 8579−8593.
(39) Nazri, G.*Preparation, Characterization and Conductivity of Li3N, Li3P and Li3As*, MRS Online Proceedings Library (OPL); Cambridge University Press, 1988; p 117 DOI: 10.1557/PROC-135-117.
(40) Lorger, S.; Usiskin, R. E.; Maier, J. Transport and Charge Carrier Chemistry in Lithium Sulfide. *Adv. Funct. Mater.* **2019**, *29*, No. 1807688.
(41) Singh, D. K.; Henss, A.; Mogwitz, B.; Gautam, A.; Horn, J.; Krauskopf, T.; Burkhardt, S.; Sann, J.; Richter, F. H.; Janek, J. $Li_6PS_5Cl$ Microstructure and Influence on Dendrite Growth in Solid-state Batteries with Lithium Metal Anode. *Cell Rep. Phys. Sci.* **2022**, *3*, No. 101043.
(42) Zhang, Q.; Pan, J.; Lu, P.; Liu, Z.; Verbrugge, M. W.; Sheldon, B. W.; Cheng, Y.-T.; Qi, Y.; Xiao, X. Synergetic Effects of Inorganic Components in Solid Electrolyte Interphase on High Cycle Efficiency of Lithium Ion Batteries. *Nano Lett.* **2016**, *16*, 2011−2016. Published Online: Feb. 24, 2016.
(43) Pan, J.; Zhang, Q.; Xiao, X.; Cheng, Y.-T.; Qi, Y. Design of Nanostructured Heterogeneous Solid Ionic Coatings through a Multiscale Defect Model. *ACS Appl. Mater. Interfaces* **2016**, *8*, 5687−5693. Published Online: Feb. 18, 2016.
(44) Wu, D.; He, J.; Liu, J.; Wu, M.; Qi, S.; Wang, H.; Huang, J.; Li, F.; Tang, D.; Ma, J. $Li_2CO_3$ / LiF-Rich Heterostructured Solid Electrolyte Interphase with Superior Lithiophilic and $Li^+$-Transferred Characteristics via Adjusting Electrolyte Additives. *Adv. Energy Mater.* **2022**, *12*, No. 2200337.
(45) Wood, K. N.; Steirer, K. X.; Hafner, S. E.; Ban, C.; Santhanagopalan, S.; Lee, S.-H.; Teeter, G. Operando X-ray Photoelectron Spectroscopy of Solid Electrolyte Interphase For-



https://doi.org/10.1021/acs.chemmater.3c00676
*Chem. Mater.* XXXX, XXX, XXX−XXX

mation and Evolution in $Li_2S$-$P_2S_5$ Solid-state Electrolytes. *Nat. Commun.* **2018**, *9*, No. 2490.
(46) Tan, J.; Matz, J.; Dong, P.; Shen, J.; Ye, M. A Growing Appreciation for the Role of LiF in the Solid Electrolyte Interphase. *Adv. Energy Mater.* **2021**, *11*, No. 2100046.
(47) Wu, H.; Jia, H.; Wang, C.; Zhang, J.-G.; Xu, W. Recent Progress in Understanding Solid Electrolyte Interphase on Lithium Metal Anodes. *Adv. Energy Mater.* **2021**, *11*, No. 2003092.



https://doi.org/10.1021/acs.chemmater.3c00676
*Chem. Mater.* XXXX, XXX, XXX−XXX

# 4 Conclusions

In this doctoral thesis, the interphase formation between lithium metal and several SEs is studied in detail. Both the chemical compositions as well as the kinetics of degradation reactions are investigated. First, two different MCI-forming types of SEs are studied: halide SEs, and LiSiPS as part of the LGPS family. In addition, the growth kinetics of the SEI-forming SE LPSCl with differently treated lithium metal anodes is investigated.

Investigation of the emerging class of halide SE revealed that the electrolytes decompose immediately upon contact with lithium. This is due to the reduction of the non-lithium cation $M^{3+}$, which is reduced by lithium metal. The formed metals induce partial electronic conductivity, causing the interphase to grow rapidly and continuously, which is detrimental to the cell impedance. Therefore, these electrolytes cannot be used as a separator electrolyte in contact with the LMA. Consequently, protective measures such as interlayers are required. One concept that has been investigated is an interlayer with LPSCl that forms a metastable SEI with lithium metal. It was found that the initial interfacial LIC|LPSCl impedance is negligible.

The second metalloid-containing SE studied in this work is LiSiPS. This SE is also unstable in contact with lithium metal. Electrochemical analyses showed that the interfacial resistance and the overpotential of the cell increase rapidly upon contact with lithium and during cycling, respectively. Both XPS and MAS-NMR measurements show that no elemental silicon or Li-Si alloy is formed during decomposition. However, it is speculated that possibly detected phosphidosilicates induce the partial electronic conductivity to enable MCI formation. In other words, although the source of the partial electronic conductivity is not clear yet, electrochemical analyses and ToF-SIMS measurements confirm the continuous interphase formation. DFT calculations and AIMD simulations support the experimental data.

The studies on the Li|LiSiPS system clearly show that it is essential to combine chemical and electrochemical analysis methods to obtain a complete picture of the decomposition reaction and kinetics. Without one method or the other, information critical to understanding the reaction would be missing. However, this information is additionally important for finding solutions to the instability.

In summary, SE containing metal or metalloid ions are promising candidates for commercial applications due to their high ionic conductivities. However, they are inherently unstable to lithium metal as metals or metalloids form after reduction of the corresponding ions. This results in the formation of a mixed conducting interphase with electronically conducting paths that either lead to short circuits or rapidly increasing interfacial resistances, both having a negative effect on the overall resistance of the cell. The continuous and detrimental growth of the MCI necessitates protective measures to prevent parasitic side reactions that degrade cell performance. These protective measures should consist of interphases that are highly $Li^+$ ion conducting but electronically insulating and have negligible interfacial impedances with both the LMA and the respective solid electrolyte.

In addition to the MCI-forming SEs, the interphase evolution of the Li|LPSCl interface was also investigated. To enable the study of a single interphase, a three-electrode cell setup was developed. A cycling experiment proved that this setup is well suited to separate the impedance response of the electrodes. Using this setup, it was found that the composition of the lithium surface affects the temporal evolution of the interphase. If freshly prepared lithium is used, the development of the interphase is fast and self-limiting. Thus, a stable interphase is formed after a formation step. In

contrast, a commercial lithium foil with a passivation layer shows higher interface resistances and a continuous interphase growth throughout the experiment.

Additionally, it was found that when passivated lithium is used, the development of the interphase is affected by the variation of the cell pressure. The parabolic rate constants of the normalized resistances were determined and plotted against the cell pressure. This showed that the growth kinetics increase with pressure. The reason for this is the amount of SE that can penetrate the passivation layer with increasing pressure. The higher the pressure, the more SE comes into direct contact with the bare lithium and reacts, thus, increasing the parabolic rate constant.

These results indicate that a clean Li|LPSCl interface forms a stable SEI after an initial formation step. However, the presence of poorly ion-conducting compounds, such as $Li_2O$ or carbonates, at the interface leads to inhibited lithium migration, to generally higher interface resistances, and continuous SEI growth. Therefore, using passivated lithium metal foils for SSB cell assembly should be reconsidered. Using freshly deposited lithium metal or reservoir-free cell designs might be more advantageous for cell impedance and long-term cycling as the lithium migration is less inhibited by the additional compounds. However, further investigations are required to confirm this hypothesis.

Overall, this doctoral thesis contributes to the understanding of the anodic stability of SEs and their decomposition reactions. This knowledge is crucial for the application of lithium metal as an anode material in SSBs with various SEs. In addition, this work highlights the influence of the lithium metal's fabrication history on the interphase growth kinetics, emphasizing the importance of addressing this factor in future designs.

# 5 Outlook

For future work, several aspects are still unclear and need further investigation. These open questions are presented briefly.

*Investigating protective concepts*

As most of the SEs with very high ionic conductivities are unstable against lithium metal, protective measures are needed to shield the electrolyte from the low potential of the lithium metal. As a first protective concept, an interlayer of LPSCl between LIC and LMA was investigated in Publication 1 and found to have a negligible interfacial resistance. However, follow-up work by Rosenbach et al. revealed side reactions at the triple phase boundary between the cathode active material, LIC as the cathode electrolyte and LPSCl as the separator electrolyte.[35] Thus, careful evaluation of the stabilities of the respective material combinations in full cells is necessary.

As an alternative to interlayers of SEI-forming solid electrolytes, protective concepts such as artificial SEIs should be investigated. Here, a thin layer of material is deposited between the LMA and SE to form an artificial SEI upon lithiation and prevent the solid electrolyte separator from decomposition. These artificial SEIs must prevent dendrite formation, have high ionic conductivity, be electronically insulating, and stable with respect to both the anode and the SE separator.

*Conductivity measurements of formed interphase products*

Sound knowledge of the absolute ionic and electronic conductivities and their relative differences could help to elucidate possible conduction pathways of the formed interphases and advance the development of protective concepts. The partial conductivities of the formed interphases have a major impact on the temporal stability, i.e., whether growth is self-limited or continuous, and the cell performance, i.e., lithium migration. Therefore, their influence is frequently observed, but the cause, especially of the electronic conductivity, is not yet fully understood.

Therefore, studying the bulk properties of the individual interphase compounds or their mixture would contribute to a better understanding of these interphases. So far, only rudimentary and contradictory information is available on the ionic conductivities of the interphase-forming decomposition products. For most of them, there is also no information on electronic conductivity since they conduct so poorly that to carry out the conductivity measurement is very difficult. To complicate matters, the formed interphases are usually mixtures of different, often amorphous compounds, which form very thin and sometimes layered structures. This changes the interphase properties or results in superposition with other measured signals.

In addition, surface effects between different compounds have not yet been studied but could have a significant impact. By studying mixtures that simulate SEI bulk properties, e.g., with impedance or Wagner-Hebb measurements, these effects could be studied in detail, which could help explain experimental data that are not yet understood. However, it is important to keep in mind that there may be differences between bulk and thin film properties. These studies could help in the creation of stable interfaces or the implementation of beneficial artificial interphases.

*Structural investigation of formed interphases*

The results of Publication 3 of this thesis show that the growth kinetics differ depending on the used lithium foil. Unfortunately, the reason for this could not be clarified, but possible causes could only be speculated on. A possible reason for this observation could be a different SEI morphology and microstructure, which allows electronic partial conductivities, e.g., due to surface effects such as space charge layers. However, the interphase structure is not yet well known or understood as these interphases are often thin, amorphous, and sensitive to beam damage. Nevertheless, investigations on the morphology and microstructure are imperative.

Studies using cryo-TEM, or CT could help to elucidate the microstructural composition of the formed interphases. In combination with the partial conductivities, conduction pathways could be found and the reason for the macroscopically observed, differing SEI growth could be explained. This would support the development of fabricated interlayers that are beneficial for cell performance.

*Interphase evolution in full cells*

So far, the temporal growth kinetics of interphases have mostly been studied in symmetric cells. However, the cathode in full cells could influence the growth kinetics due to effects such as cross-talk, thus affecting the resistance evolution and cell performance. Therefore, further studies are needed to understand the interphase formation in full cells. By implementing three-electrode setups, the influence of both electrodes on the measurement can be well separated.

*Influence of the manufacturing conditions*

As the cell fabrication usually differs between academic and industrial investigations, this influence should be considered and studied further to enable more rapid introduction of commercial SSBs. For example, the transition from an Ar-filled glovebox to a dry room could change the surface of the SEs due to oxidation or hydrolysis. This could influence the interphase formation and properties. However, depending on the formed products, the oxidized surface could be used to stabilize the interfaces towards the electrodes. Large-scale industrial facilities would also make it more feasible to use fresh, non-passivated lithium for cell production. This would significantly improve the cell performance of SSBs.

Finding strategies to minimize production impacts or use them to benefit cell performance while facilitating handling conditions play a significant role in the commercialization of SSBs. In addition, transferring SSBs from lab-scale cell production to industrial scale and commercial use of initial pilot cells would support the development of SSBs as more challenges can be identified and addressed. This would accelerate the widespread commercial use of SSBs.

# 6 References

(1) Azam, S.; Meisner, Q.; Aiken, C. P.; Song, W.; Liu, Q.; Yoo, D.-J.; Eldesoky, A.; Zhang, Z.; Dahn, J. R. Performance of a Novel In-Situ Converted Additive for High Voltage Li-ion Pouch Cells. *J. Electrochem. Soc.* **2022**, *169* (10), 100552. DOI: 10.1149/1945-7111/ac9c36.

(2) Wu, H.; Jia, H.; Wang, C.; Zhang, J.-G.; Xu, W. Recent Progress in Understanding Solid Electrolyte Interphase on Lithium Metal Anodes. *Adv. Energy Mater.* **2021**, *11* (5), 2003092. DOI: 10.1002/aenm.202003092.

(3) Brandt, K. Historical development of secondary lithium batteries. *Solid State Ion.* **1994**, *69* (3-4), 173–183. DOI: 10.1016/0167-2738(94)90408-1.

(4) Lin, D.; Liu, Y.; Cui, Y. Reviving the lithium metal anode for high-energy batteries. *Nat. Nanotechnol.* **2017**, *12* (3), 194–206. DOI: 10.1038/nnano.2017.16.

(5) Zhai, P.; Liu, L.; Gu, X.; Wang, T.; Gong, Y. Interface Engineering for Lithium Metal Anodes in Liquid Electrolyte. *Adv. Energy Mater.* **2020**, *10* (34), 2001257. DOI: 10.1002/aenm.202001257.

(6) Peled, E. The Electrochemical Behavior of Alkali and Alkaline Earth Metals in Nonaqueous Battery Systems—The Solid Electrolyte Interphase Model. *J. Electrochem. Soc.* **1979**, *126* (12), 2047–2051. DOI: 10.1149/1.2128859.

(7) Banerjee, A.; Wang, X.; Fang, C.; Wu, E. A.; Meng, Y. S. Interfaces and Interphases in All-Solid-State Batteries with Inorganic Solid Electrolytes. *Chem. Rev.* **2020**, *120* (14), 6878–6933. DOI: 10.1021/acs.chemrev.0c00101. Published Online: Jun. 30, 2020.

(8) McDowell, M. T.; Cortes, F. J. Q.; Thenuwara, A. C.; Lewis, J. A. Toward High-Capacity Battery Anode Materials: Chemistry and Mechanics Intertwined. *Chem. Mater.* **2020**, *32* (20), 8755–8771. DOI: 10.1021/acs.chemmater.0c02981.

(9) Drvarič Talian, S.; Bobnar, J.; Sinigoj, A. R.; Humar, I.; Gaberšček, M. Transmission Line Model for Description of the Impedance Response of Li Electrodes with Dendritic Growth. *J. Phys. Chem. C* **2019**, *123* (46), 27997–28007. DOI: 10.1021/acs.jpcc.9b05887.

(10) Janek, J.; Zeier, W. G. Challenges in speeding up solid-state battery development. *Nat. Energy* **2023**, *8*, 230–240. DOI: 10.1038/s41560-023-01208-9.

(11) Weiss, M.; Simon, F. J.; Busche, M. R.; Nakamura, T.; Schröder, D.; Richter, F. H.; Janek, J. From Liquid- to Solid-State Batteries: Ion Transfer Kinetics of Heteroionic Interfaces. *Electrochem. Energ. Rev.* **2020**, *3* (2), 221–238. DOI: 10.1007/s41918-020-00062-7.

(12) Narayanan, S.; Ulissi, U.; Gibson, J. S.; Chart, Y. A.; Weatherup, R. S.; Pasta, M. Effect of current density on the solid electrolyte interphase formation at the lithium|$Li_6PS_5Cl$ interface. *Nat. Commun.* **2022**, *13* (1), 7237. DOI: 10.1038/s41467-022-34855-9. Published Online: Nov. 24, 2022.

(13) Janek, J.; Zeier, W. G. A solid future for battery development. *Nat. Energy* **2016**, *1* (9), 16141. DOI: 10.1038/nenergy.2016.141.

(14) Krauskopf, T.; Richter, F. H.; Zeier, W. G.; Janek, J. Physicochemical Concepts of the Lithium Metal Anode in Solid-State Batteries. *Chem. Rev.* **2020**, *120* (15), 7745–7794. DOI: 10.1021/acs.chemrev.0c00431. Published Online: Jul. 27, 2020.

(15) Krauskopf, T.; Hartmann, H.; Zeier, W. G.; Janek, J. Toward a Fundamental Understanding of the Lithium Metal Anode in Solid-State Batteries-An Electrochemo-Mechanical Study on the Garnet-Type Solid Electrolyte $Li_{6.25}Al_{0.25}La_3Zr_2O_{12}$. *ACS Appl. Mater. Interfaces* **2019**, *11* (15), 14463–14477. DOI: 10.1021/acsami.9b02537.

(16) Singh, D. K.; Fuchs, T.; Krempaszky, C.; Schweitzer, P.; Lerch, C.; Richter, F. H.; Janek, J. Origin of the lithium metal anode instability in solid-state batteries during discharge. *Matter* **2023**, *6* (5), 1463–1483. DOI: 10.1016/j.matt.2023.02.008.

(17) Krauskopf, T.; Dippel, R.; Hartmann, H.; Peppler, K.; Mogwitz, B.; Richter, F. H.; Zeier, W. G.; Janek, J. Lithium-Metal Growth Kinetics on LLZO Garnet-Type Solid Electrolytes. *Joule* **2019**, *3* (8), 2030–2049. DOI: 10.1016/j.joule.2019.06.013.

(18) Hartmann, P.; Leichtweiss, T.; Busche, M. R.; Schneider, M.; Reich, M.; Sann, J.; Adelhelm, P.; Janek, J. Degradation of NASICON-Type Materials in Contact with Lithium Metal: Formation of Mixed Conducting Interphases (MCI) on Solid Electrolytes. *J. Phys. Chem. C* **2013**, *117* (41), 21064–21074. DOI: 10.1021/jp4051275.
(19) Wenzel, S.; Randau, S.; Leichtweiß, T.; Weber, D. A.; Sann, J.; Zeier, W. G.; Janek, J. Direct Observation of the Interfacial Instability of the Fast Ionic Conductor $Li_{10}GeP_2S_{12}$ at the Lithium Metal Anode. *Chem. Mater.* **2016**, *28* (7), 2400–2407. DOI: 10.1021/acs.chemmater.6b00610.
(20) Wenzel, S.; Sedlmaier, S. J.; Dietrich, C.; Zeier, W. G.; Janek, J. Interfacial reactivity and interphase growth of argyrodite solid electrolytes at lithium metal electrodes. *Solid State Ion.* **2018**, *318*, 102–112. DOI: 10.1016/j.ssi.2017.07.005.
(21) Riegger, L. M.; Otto, S.-K.; Sadowski, M.; Jovanovic, S.; Kötz, O.; Harm, S.; Balzat, L. G.; Merz, S.; Burkhardt, S.; Richter, F. H.; Sann, J.; Eichel, R.-A.; Lotsch, B. V.; Granwehr, J.; Albe, K.; Janek, J. Instability of the $Li_7SiPS_8$ Solid Electrolyte at the Lithium Metal Anode and Interphase Formation. *Chem. Mater.* **2022**, *34* (8), 3659–3669. DOI: 10.1021/acs.chemmater.1c04302.
(22) Riegger, L. M.; Schlem, R.; Sann, J.; Zeier, W. G.; Janek, J. Lithium-Metal Anode Instability of the Superionic Halide Solid Electrolytes and the Implications for Solid-State Batteries. *Angew. Chem. Int. Ed.* **2021**, *60* (12), 6718–6723. DOI: 10.1002/anie.202015238. Published Online: Feb. 1, 2021.
(23) Wenzel, S.; Leichtweiss, T.; Krüger, D.; Sann, J.; Janek, J. Interphase formation on lithium solid electrolytes - An in situ approach to study interfacial reactions by photoelectron spectroscopy. *Solid State Ion.* **2015**, *278*, 98–105. DOI: 10.1016/j.ssi.2015.06.001.
(24) Davis, A. L.; Kazyak, E.; Liao, D. W.; Wood, K. N.; Dasgupta, N. P. Operando Analysis of Interphase Dynamics in Anode-Free Solid-State Batteries with Sulfide Electrolytes. *J. Electrochem. Soc.* **2021**, *168* (7), 70557. DOI: 10.1149/1945-7111/ac163d.
(25) Riegger, L. M.; Mittelsdorf, S.; Fuchs, T.; Rueß, R.; Richter, F. H.; Janek, J. Evolution of the Interphase between Argyrodite-Based Solid Electrolytes and the Lithium Metal Anode─The Kinetics of Solid Electrolyte Interphase Growth. *Chem. Mater.* **2023**, *35* (13), 5091–5099. DOI: 10.1021/acs.chemmater.3c00676.
(26) Otto, S.-K.; Riegger, L. M.; Fuchs, T.; Kayser, S.; Schweitzer, P.; Burkhardt, S.; Henss, A.; Janek, J. In Situ Investigation of Lithium Metal–Solid Electrolyte Anode Interfaces with ToF-SIMS. *Adv Mater. Interfaces* **2022**, *9* (13), 2102387. DOI: 10.1002/admi.202102387.
(27) Kamaya, N.; Homma, K.; Yamakawa, Y.; Hirayama, M.; Kanno, R.; Yonemura, M.; Kamiyama, T.; Kato, Y.; Hama, S.; Kawamoto, K.; Mitsui, A. A lithium superionic conductor. *Nat. Mater.* **2011**, *10* (9), 682–686. DOI: 10.1038/nmat3066.
(28) Ohno, S.; Banik, A.; Dewald, G. F.; Kraft, M. A.; Krauskopf, T.; Minafra, N.; Till, P.; Weiss, M.; Zeier, W. G. Materials design of ionic conductors for solid state batteries. *Prog. Energy* **2020**, *2* (2), 22001. DOI: 10.1088/2516-1083/ab73dd.
(29) Minnmann, P.; Quillman, L.; Burkhardt, S.; Richter, F. H.; Janek, J. Editors' Choice—Quantifying the Impact of Charge Transport Bottlenecks in Composite Cathodes of All-Solid-State Batteries. *J. Electrochem. Soc.* **2021**, *168* (4), 40537. DOI: 10.1149/1945-7111/abf8d7.
(30) Wang, C.; Liang, J.; Kim, J. T.; Sun, X. Prospects of halide-based all-solid-state batteries: From material design to practical application. *Sci. Adv.* **2022**, *8* (36), eadc9516. DOI: 10.1126/sciadv.adc9516. Published Online: Sep. 7, 2022.
(31) Asano, T.; Sakai, A.; Ouchi, S.; Sakaida, M.; Miyazaki, A.; Hasegawa, S. Solid Halide Electrolytes with High Lithium-Ion Conductivity for Application in 4 V Class Bulk-Type All-Solid-State Batteries. *Advanced materials (Deerfield Beach, Fla.)* **2018**, *30* (44), e1803075. DOI: 10.1002/adma.201803075.
(32) Schlem, R.; Muy, S.; Prinz, N.; Banik, A.; Shao-Horn, Y.; Zobel, M.; Zeier, W. G. Mechanochemical Synthesis: A Tool to Tune Cation Site Disorder and Ionic Transport Properties of

$Li_3MCl_6$ (M = Y, Er) Superionic Conductors. *Adv. Energy Mater.* **2020**, *10* (6), 1903719. DOI: 10.1002/aenm.201903719.

(33) Park, K.-H.; Kaup, K.; Assoud, A.; Zhang, Q.; Wu, X.; Nazar, L. F. High-Voltage Superionic Halide Solid Electrolytes for All-Solid-State Li-Ion Batteries. *ACS Energy Lett.* **2020** (5), 533–539. DOI: 10.1021/acsenergylett.9b02599.

(34) Wang, S.; Bai, Q.; Nolan, A. M.; Liu, Y.; Gong, S.; Sun, Q.; Mo, Y. Lithium Chlorides and Bromides as Promising Solid-State Chemistries for Fast Ion Conductors with Good Electrochemical Stability. *Angew. Chem. Int. Ed.* **2019**, *58* (24), 8039–8043. DOI: 10.1002/anie.201901938.

(35) Rosenbach, C.; Walther, F.; Ruhl, J.; Hartmann, M.; Hendriks, T. A.; Ohno, S.; Janek, J.; Zeier, W. G. Visualizing the Chemical Incompatibility of Halide and Sulfide-Based Electrolytes in Solid-State Batteries. *Adv. Energy Mater.* **2023**, *13* (6), 2203673. DOI: 10.1002/aenm.202203673.

(36) Umeshbabu, E.; Maddukuri, S.; Hu, Y.; Fichtner, M.; Munnangi, A. R. Influence of Chloride Ion Substitution on Lithium-Ion Conductivity and Electrochemical Stability in a Dual-Halogen Solid-State Electrolyte. *ACS Appl. Mater. Interfaces* **2022**, *14* (22), 25448–25456. DOI: 10.1021/acsami.2c04160. Published Online: May. 27, 2022.

(37) Harm, S.; Hatz, A.-K.; Moudrakovski, I.; Eger, R.; Kuhn, A.; Hoch, C.; Lotsch, B. V. Lesson Learned from NMR: Characterization and Ionic Conductivity of LGPS-like $Li_7SiPS_8$. *Chem. Mater.* **2019**, *31* (4), 1280–1288. DOI: 10.1021/acs.chemmater.8b04051.

(38) Calaminus, R.; Harm, S.; Fabini, D. H.; Balzat, L. G.; Hatz, A.-K.; Duppel, V.; Moudrakovski, I.; Lotsch, B. V. Enhancing Ionic Conductivity by in Situ Formation of $Li_7SiPS_8$ /Argyrodite Hybrid Solid Electrolytes. *Chem. Mater.* **2022**, *34* (17), 7666–7677. DOI: 10.1021/acs.chemmater.2c00346.

(39) Chen, F.; Cheng, S.; Liu, J.-B.; Li, S.; Ouyang, W.; Liu, B. Insights into the Electrochemical Stability and Lithium Conductivity of $Li_4MS_4$ (M = Si, Ge, and Sn). *ACS Appl. Mater. Interfaces* **2021**, *13* (19), 22438–22447. DOI: 10.1021/acsami.1c03227.

(40) Zhu, Y.; He, X.; Mo, Y. Strategies Based on Nitride Materials Chemistry to Stabilize Li Metal Anode. *Adv. Sci.* **2017**, *4* (8), 1600517. DOI: 10.1002/advs.201600517.

(41) Gautam, A.; Sadowski, M.; Ghidiu, M.; Minafra, N.; Senyshyn, A.; Albe, K.; Zeier, W. G. Engineering the Site-Disorder and Lithium Distribution in the Lithium Superionic Argyrodite $Li_6PS_5Br$. *Adv. Energy Mater.* **2021**, *11* (5), 2003369. DOI: 10.1002/aenm.202003369.

(42) Rayavarapu, P. R.; Sharma, N.; Peterson, V. K.; Adams, S. Variation in structure and Li+-ion migration in argyrodite-type $Li_6PS_5X$ (X = Cl, Br, I) solid electrolytes. *J Solid State Electrochem.* **2012**, *16* (5), 1807–1813. DOI: 10.1007/s10008-011-1572-8.

(43) Minafra, N.; Culver, S. P.; Krauskopf, T.; Senyshyn, A.; Zeier, W. G. Effect of Si substitution on the structural and transport properties of superionic Li-argyrodites. *J. Mater. Chem. A* **2018**, *6* (2), 645–651. DOI: 10.1039/C7TA08581H.

(44) Ohno, S.; Helm, B.; Fuchs, T.; Dewald, G.; Kraft, M. A.; Culver, S. P.; Senyshyn, A.; Zeier, W. G. Further Evidence for Energy Landscape Flattening in the Superionic Argyrodites $Li_{6+x}P_{1-x}M_xS_5I$ (M = Si, Ge, Sn). *Chem. Mater.* **2019**, *31* (13), 4936–4944. DOI: 10.1021/acs.chemmater.9b01857.

(45) Gautam, A.; Ghidiu, M.; Suard, E.; Kraft, M. A.; Zeier, W. G. On the Lithium Distribution in Halide Superionic Argyrodites by Halide Incorporation in $Li_{7-x}PS_{6-x}Cl_x$. *ACS Appl. Energy Mater.* **2021**, *4* (7), 7309–7315. DOI: 10.1021/acsaem.1c01417.

(46) Adeli, P.; Bazak, J. D.; Park, K. H.; Kochetkov, I.; Huq, A.; Goward, G. R.; Nazar, L. F. Boosting Solid-State Diffusivity and Conductivity in Lithium Superionic Argyrodites by Halide Substitution. *Angew. Chem. Int. Ed.* **2019**, *58* (26), 8681–8686. DOI: 10.1002/anie.201814222. Published Online: May. 24, 2019.

(47) Batzer, M.; Heck, C.; Michalowski, P.; Kwade, A. Current Status of Formulations and Scalable Processes for Producing Sulfidic Solid-State Batteries. *Batteries Supercaps* **2022**, *5* (12). DOI: 10.1002/batt.202200328.

(48) Heubner, C.; Maletti, S.; Auer, H.; Hüttl, J.; Voigt, K.; Lohrberg, O.; Nikolowski, K.; Partsch, M.; Michaelis, A. From Lithium-Metal toward Anode-Free Solid-State Batteries: Current Developments, Issues, and Challenges. *Adv. Funct. Mater.* **2021**, *31* (51), 2106608. DOI: 10.1002/adfm.202106608.
(49) Lee, Y.-G.; Fujiki, S.; Jung, C.; Suzuki, N.; Yashiro, N.; Omoda, R.; Ko, D.-S.; Shiratsuchi, T.; Sugimoto, T.; Ryu, S.; Ku, J. H.; Watanabe, T.; Park, Y.; Aihara, Y.; Im, D.; Han, I. T. High-energy long-cycling all-solid-state lithium metal batteries enabled by silver–carbon composite anodes. *Nat. Energy* **2020**, *5* (4), 299–308. DOI: 10.1038/s41560-020-0575-z.
(50) Lewis, J. A.; Cavallaro, K. A.; Liu, Y.; McDowell, M. T. The promise of alloy anodes for solid-state batteries. *Joule* **2022**, *6* (7), 1418–1430. DOI: 10.1016/j.joule.2022.05.016.
(51) Tan, D. H. S.; Chen, Y.-T.; Yang, H.; Bao, W.; Sreenarayanan, B.; Doux, J.-M.; Li, W.; Lu, B.; Ham, S.-Y.; Sayahpour, B.; Scharf, J.; Wu, E. A.; Deysher, G.; Han, H. E.; Hah, H. J.; Jeong, H.; Lee, J. B.; Chen, Z.; Meng, Y. S. Carbon-free high-loading silicon anodes enabled by sulfide solid electrolytes. *Science* **2021**, *373* (6562), 1494–1499. DOI: 10.1126/science.abg7217. Published Online: Sep. 23, 2021.
(52) Li, D.; Liu, H.; Liang, Y.; Wang, C.; Fan, L.-Z. Challenges and Developments of High Energy Density Anode Materials in Sulfide-Based Solid-State Batteries. *ChemElectroChem* **2022**, *9* (24). DOI: 10.1002/celc.202200923.
(53) Obrovac, M. N.; Chevrier, V. L. Alloy negative electrodes for Li-ion batteries. *Chem. Rev.* **2014**, *114* (23), 11444–11502. DOI: 10.1021/cr500207g. Published Online: Nov. 17, 2014.
(54) Jeppson, D. W.; Ballif, J. L.; Yuan, W. W.; Chou, B. E. *Lithium literature review: lithium's properties and interactions*.
(55) Schmuch, R.; Wagner, R.; Hörpel, G.; Placke, T.; Winter, M. Performance and cost of materials for lithium-based rechargeable automotive batteries. *Nat. Energy* **2018**, *3* (4), 267–278. DOI: 10.1038/s41560-018-0107-2.
(56) Wietelmann, U.; Steinbild, M. Lithium and Lithium Compounds. In *Ullmann's encyclopedia of industrial chemistry*, 6., completely rev. ed.; Wiley-VCH, 2003; pp 1–38. DOI: 10.1002/14356007.a15_393.pub2.
(57) Otto, S.-K.; Moryson, Y.; Krauskopf, T.; Peppler, K.; Sann, J.; Janek, J.; Henss, A. In-Depth Characterization of Lithium-Metal Surfaces with XPS and ToF-SIMS: Toward Better Understanding of the Passivation Layer. *Chem. Mater.* **2021**, *33* (33), 859–867. DOI: 10.1021/acs.chemmater.0c03518.
(58) Krauskopf, T.; Mogwitz, B.; Rosenbach, C.; Zeier, W. G.; Janek, J. Diffusion Limitation of Lithium Metal and Li–Mg Alloy Anodes on LLZO Type Solid Electrolytes as a Function of Temperature and Pressure. *Adv. Energy Mater.* **2019**, *9* (44), 1902568. DOI: 10.1002/aenm.201902568.
(59) Wang, M. J.; Choudhury, R.; Sakamoto, J. Characterizing the Li-Solid-Electrolyte Interface Dynamics as a Function of Stack Pressure and Current Density. *Joule* **2019**, *3* (9), 2165–2178. DOI: 10.1016/j.joule.2019.06.017.
(60) Doux, J.-M.; Nguyen, H.; Tan, D. H. S.; Banerjee, A.; Wang, X.; Wu, E. A.; Jo, C.; Yang, H.; Meng, Y. S. Stack Pressure Considerations for Room-Temperature All-Solid-State Lithium Metal Batteries. *Adv. Energy Mater.* **2020**, *10* (1), 1903253. DOI: 10.1002/aenm.201903253.
(61) Singh, D. K.; Fuchs, T.; Krempaszky, C.; Mogwitz, B.; Burkhardt, S.; Richter, F. H.; Janek, J. Overcoming Anode Instability in Solid-State Batteries through Control of the Lithium Metal Microstructure. *Adv. Funct. Mater.* **2023**, *33* (1), 2211067. DOI: 10.1002/adfm.202211067.
(62) Siniscalchi, M.; Liu, J.; Gibson, J. S.; Turrell, S. J.; Aspinall, J.; Weatherup, R. S.; Pasta, M.; Speller, S. C.; Grovenor, C. R. M. On the Relative Importance of Li Bulk Diffusivity and Interface Morphology in Determining the Stripped Capacity of Metallic Anodes in Solid-State Batteries. *ACS Energy Lett.* **2022**, *7* (10), 3593–3599. DOI: 10.1021/acsenergylett.2c01793. Published Online: Sep. 27, 2022.

(63) Hitz, G. T.; McOwen, D. W.; Zhang, L.; Ma, Z.; Fu, Z.; Wen, Y.; Gong, Y.; Dai, J.; Hamann, T. R.; Hu, L.; Wachsman, E. D. High-rate lithium cycling in a scalable trilayer Li-garnet-electrolyte architecture. *Mater. Today* **2019**, *22*, 50–57. DOI: 10.1016/j.mattod.2018.04.004.
(64) Fuchs, T.; Haslam, C. G.; Moy, A. C.; Lerch, C.; Krauskopf, T.; Sakamoto, J.; Richter, F. H.; Janek, J. Increasing the Pressure-Free Stripping Capacity of the Lithium Metal Anode in Solid-State-Batteries by Carbon Nanotubes. *Adv. Energy Mater.* **2022**, *12* (26), 2201125. DOI: 10.1002/aenm.202201125.
(65) Wang, C.; Gong, Y.; Liu, B.; Fu, K.; Yao, Y.; Hitz, E.; Li, Y.; Dai, J.; Xu, S.; Luo, W.; Wachsman, E. D.; Hu, L. Conformal, Nanoscale ZnO Surface Modification of Garnet-Based Solid-State Electrolyte for Lithium Metal Anodes. *Nano Lett.* **2017**, *17* (1), 565–571. DOI: 10.1021/acs.nanolett.6b04695. Published Online: Dec. 16, 2016.
(66) McOwen, D. W.; Xu, S.; Gong, Y.; Wen, Y.; Godbey, G. L.; Gritton, J. E.; Hamann, T. R.; Dai, J.; Hitz, G. T.; Hu, L.; Wachsman, E. D. 3D-Printing Electrolytes for Solid-State Batteries. *Adv. Mater.* **2018**, *30* (18), e1707132. DOI: 10.1002/adma.201707132. Published Online: Mar. 25, 2018.
(67) Fuchs, T. Morphological Challenges at the Interface of Lithium Metal and Electrolytes in Garnet-type Solid-State Batteries. PhD thesis, Justus-Liebig-Universität Gießen, Gießen, 2022.
(68) Hatzell, K. B.; Chen, X. C.; Cobb, C. L.; Dasgupta, N. P.; Dixit, M. B.; Marbella, L. E.; McDowell, M. T.; Mukherjee, P. P.; Verma, A.; Viswanathan, V.; Westover, A. S.; Zeier, W. G. Challenges in Lithium Metal Anodes for Solid-State Batteries. *ACS Energy Lett.* **2020**, *5* (3), 922–934. DOI: 10.1021/acsenergylett.9b02668.
(69) Harry, K. J.; Hallinan, D. T.; Parkinson, D. Y.; MacDowell, A. A.; Balsara, N. P. Detection of subsurface structures underneath dendrites formed on cycled lithium metal electrodes. *Nat. Mater.* **2014**, *13* (1), 69–73. DOI: 10.1038/nmat3793. Published Online: Nov. 24, 2013.
(70) Maslyn, J. A.; Frenck, L.; Loo, W. S.; Parkinson, D. Y.; Balsara, N. P. Extended Cycling through Rigid Block Copolymer Electrolytes Enabled by Reducing Impurities in Lithium Metal Electrodes. *ACS Appl. Energy Mater.* **2019**, *2* (11), 8197–8206. DOI: 10.1021/acsaem.9b01685.
(71) Singh, D. K.; Henss, A.; Mogwitz, B.; Gautam, A.; Horn, J.; Krauskopf, T.; Burkhardt, S.; Sann, J.; Richter, F. H.; Janek, J. $Li_6PS_5Cl$ microstructure and influence on dendrite growth in solid-state batteries with lithium metal anode. *Cell Rep. Phys. Sci.* **2022**, *3* (9), 101043. DOI: 10.1016/j.xcrp.2022.101043.
(72) Lu, Y.; Zhao, C.-Z.; Yuan, H.; Cheng, X.-B.; Huang, J.-Q.; Zhang, Q. Critical Current Density in Solid-State Lithium Metal Batteries: Mechanism, Influences, and Strategies. *Adv. Funct. Mater.* **2021**, *31* (18), 2009925. DOI: 10.1002/adfm.202009925.
(73) Tang, Y.; Zhang, L.; Chen, J.; Sun, H.; Yang, T.; Liu, Q.; Huang, Q.; Zhu, T.; Huang, J. Electro-chemo-mechanics of lithium in solid state lithium metal batteries. *Energy Environ. Sci.* **2021**, *14* (2), 602–642. DOI: 10.1039/D0EE02525A.
(74) Acebedo, B.; Morant-Miñana, M. C.; Gonzalo, E.; Ruiz de Larramendi, I.; Villaverde, A.; Rikarte, J.; Fallarino, L. Current Status and Future Perspective on Lithium Metal Anode Production Methods. *Adv. Energy Mater.* **2023**, 2203744. DOI: 10.1002/aenm.202203744.
(75) Otto, S.-K.; Fuchs, T.; Moryson, Y.; Lerch, C.; Mogwitz, B.; Sann, J.; Janek, J.; Henss, A. Storage of Lithium Metal: The Role of the Native Passivation Layer for the Anode Interface Resistance in Solid State Batteries. *ACS Appl. Energy Mater.* **2021**, *4* (11), 12798–12807. DOI: 10.1021/acsaem.1c02481.
(76) Wietelmann, U. Oberflächenpassiviertes Lithiummetall und Verfahren zu dessen Herstellung. DE20101063233 20101216.
(77) Wietelmann, U.; Hartnig, C.; Emmel, U.; Nickel, V. Stabilisierte mit einer stickstoffhaltigen Schale beschichtete Lithiummetallabformungen und Verfahren zu deren Herstellung. DE201410207396 20140417.

(78) Ji, X.; Hou, S.; Wang, P.; He, X.; Piao, N.; Chen, J.; Fan, X.; Wang, C. Solid-State Electrolyte Design for Lithium Dendrite Suppression. *Adv. Mater.* **2020**, *32* (46), e2002741. DOI: 10.1002/adma.202002741.
(79) Su, J.; Pasta, M.; Ning, Z.; Gao, X.; Bruce, P. G.; Grovenor, C. R. M. Interfacial modification between argyrodite-type solid-state electrolytes and Li metal anodes using LiPON interlayers. *Energy Environ. Sci.* **2022**, *15* (9), 3805–3814. DOI: 10.1039/D2EE01390H.
(80) Gold, V. *The IUPAC Compendium of Chemical Terminology*; International Union of Pure and Applied Chemistry (IUPAC), 2019. DOI: 10.1351/goldbook.
(81) Ong, S. P.; Mo, Y.; Richards, W. D.; Miara, L.; Lee, H. S.; Ceder, G. Phase stability, electrochemical stability and ionic conductivity of the $Li_{10\pm1}MP_2X_{12}$ (M = Ge, Si, Sn, Al or P, and X = O, S or Se) family of superionic conductors. *Energy Environ. Sci.* **2013**, *6* (1), 148–156. DOI: 10.1039/C2EE23355J.
(82) Zhu, Y.; He, X.; Mo, Y. Origin of Outstanding Stability in the Lithium Solid Electrolyte Materials: Insights from Thermodynamic Analyses Based on First-Principles Calculations. *ACS Appl. Mater. Interfaces* **2015**, *7* (42), 23685–23693. DOI: 10.1021/acsami.5b07517.
(83) Zhu, Y.; He, X.; Mo, Y. First principles study on electrochemical and chemical stability of solid electrolyte–electrode interfaces in all-solid-state Li-ion batteries. *J. Mater. Chem. A* **2016**, *4* (9), 3253–3266. DOI: 10.1039/C5TA08574H.
(84) Schwietert, T. K.; Arszelewska, V. A.; Wang, C.; Yu, C.; Vasileiadis, A.; Klerk, N. J. J. de; Hageman, J.; Hupfer, T.; Kerkamm, I.; Xu, Y.; van der Maas, E.; Kelder, E. M.; Ganapathy, S.; Wagemaker, M. Clarifying the relationship between redox activity and electrochemical stability in solid electrolytes. *Nat. Mater.* **2020**, *19* (4), 428–435. DOI: 10.1038/s41563-019-0576-0.
(85) Ohno, S.; Rosenbach, C.; Dewald, G. F.; Janek, J.; Zeier, W. G. Linking Solid Electrolyte Degradation to Charge Carrier Transport in the Thiophosphate-Based Composite Cathode toward Solid-State Lithium-Sulfur Batteries. *Adv. Funct. Mater.* **2021**, *31* (18), 2010620. DOI: 10.1002/adfm.202010620.
(86) Lorger, S.; Usiskin, R. E.; Maier, J. Transport and Charge Carrier Chemistry in Lithium Sulfide. *Adv. Funct. Mater.* **2019**, *29* (6), 1807688. DOI: 10.1002/adfm.201807688.
(87) Nazri, G. Preparation, Characterization and Conductivity of $Li_3N$, $Li_3P$ and $Li_3As$. *MRS Proc.* **1988**, *135*, 117–130. DOI: 10.1557/PROC-135-117.
(88) Hofstetter, K.; Samson, A. J.; Narayanan, S.; Thangadurai, V. Present understanding of the stability of Li-stuffed garnets with moisture, carbon dioxide, and metallic lithium. *J. Power Sources* **2018**, *390*, 297–312. DOI: 10.1016/j.jpowsour.2018.04.016.
(89) Ma, C.; Cheng, Y.; Yin, K.; Luo, J.; Sharafi, A.; Sakamoto, J.; Li, J.; More, K. L.; Dudney, N. J.; Chi, M. Interfacial Stability of Li Metal-Solid Electrolyte Elucidated via in Situ Electron Microscopy. *Nano letters* **2016**, *16* (11), 7030–7036. DOI: 10.1021/acs.nanolett.6b03223. Published Online: Oct. 6, 2016.
(90) Wenzel, S. Thermodynamic and kinetic instability of inorganic solid electrolytes at lithium and sodium metal electrodes. PhD thesis, Justus-Liebig-University Giessen, Giessen, 2016.
(91) Bron, P.; Roling, B.; Dehnen, S. Impedance characterization reveals mixed conducting interphases between sulfidic superionic conductors and lithium metal electrodes. *J. Power Sources* **2017**, *352*, 127–134. DOI: 10.1016/j.jpowsour.2017.03.103.
(92) López, I.; Morey, J.; Ledeuil, J. B.; Madec, L.; Martinez, H. A critical discussion on the analysis of buried interfaces in Li solid-state batteries. Ex situ and in situ / operando studies. *J. Mater. Chem. A* **2021**, *9* (45), 25341–25368. DOI: 10.1039/D1TA04532F.
(93) Wood, K. N.; Steirer, K. X.; Hafner, S. E.; Ban, C.; Santhanagopalan, S.; Lee, S.-H.; Teeter, G. Operando X-ray photoelectron spectroscopy of solid electrolyte interphase formation and evolution in $Li_2S$-$P_2S_5$ solid-state electrolytes. *Nat. Commun.* **2018**, *9* (1), 2490. DOI: 10.1038/s41467-018-04762-z.

(94) Narayanan, S.; Gibson, J. S.; Aspinall, J.; Weatherup, R. S.; Pasta, M. In situ and operando characterisation of Li metal – Solid electrolyte interfaces. *Curr. Opin. Solid State and Mater. Sci.* **2022**, *26* (2), 100978. DOI: 10.1016/j.cossms.2021.100978.
(95) Boebinger, M. G.; Lewis, J. A.; Sandoval, S. E.; McDowell, M. T. Understanding Transformations in Battery Materials Using in Situ and Operando Experiments: Progress and Outlook. *ACS Energy Lett.* **2020**, *5* (1), 335–345. DOI: 10.1021/acsenergylett.9b02514.
(96) Lewis, J. A.; Cortes, F. J. Q.; Boebinger, M. G.; Tippens, J.; Marchese, T. S.; Kondekar, N.; Liu, X.; Chi, M.; McDowell, M. T. Interphase Morphology between a Solid-State Electrolyte and Lithium Controls Cell Failure. *ACS Energy Lett.* **2019**, *4* (2), 591–599. DOI: 10.1021/acsenergylett.9b00093.
(97) Dixit, M. B.; Singh, N.; Horwath, J. P.; Shevchenko, P. D.; Jones, M.; Stach, E. A.; Arthur, T. S.; Hatzell, K. B. In Situ Investigation of Chemomechanical Effects in Thiophosphate Solid Electrolytes. *Matter* **2020**, *3* (6), 2138–2159. DOI: 10.1016/j.matt.2020.09.018.
(98) Tippens, J.; Miers, J. C.; Afshar, A.; Lewis, J. A.; Cortes, F. J. Q.; Qiao, H.; Marchese, T. S.; Di Leo, C. V.; Saldana, C.; McDowell, M. T. Visualizing Chemomechanical Degradation of a Solid-State Battery Electrolyte. *ACS Energy Lett.* **2019**, *4* (6), 1475–1483. DOI: 10.1021/acsenergylett.9b00816.
(99) Lewis, J. A.; Cortes, F. J. Q.; Liu, Y.; Miers, J. C.; Verma, A.; Vishnugopi, B. S.; Tippens, J.; Prakash, D.; Marchese, T. S.; Han, S. Y.; Lee, C.; Shetty, P. P.; Lee, H.-W.; Shevchenko, P.; Carlo, F. de; Saldana, C.; Mukherjee, P. P.; McDowell, M. T. Linking void and interphase evolution to electrochemistry in solid-state batteries using operando X-ray tomography. *Nat. Mater.* **2021**, *20* (4), 503–510. DOI: 10.1038/s41563-020-00903-2. Published Online: Jan. 28, 2021.
(100) Miao, N.; Hai, B.; Wang, S.; Ni, J.; Li, X.; Wei, H.; Zhang, K.; Wang, X.; Huang, W. An in-situ X-ray computed tomography imaging apparatus with stack pressures for rechargeable batteries. *Scr. Mater.* **2023**, *229*, 115381. DOI: 10.1016/j.scriptamat.2023.115381.
(101) Kasemchainan, J.; Zekoll, S.; Spencer Jolly, D.; Ning, Z.; Hartley, G. O.; Marrow, J.; Bruce, P. G. Critical stripping current leads to dendrite formation on plating in lithium anode solid electrolyte cells. *Nat. Mater.* **2019.** DOI: 10.1038/s41563-019-0438-9.
(102) Kim, S. H.; Kim, K.; Choi, H.; Im, D.; Heo, S.; Choi, H. S. In situ observation of lithium metal plating in a sulfur-based solid electrolyte for all-solid-state batteries. *J. Mater. Chem. A* **2019**, *7* (22), 13650–13657. DOI: 10.1039/C9TA02614B.
(103) Vickerman, J. C.; Gilmore, I. S. *Surface analysis - The principal techniques*, 2nd edition; J. Wiley e-book, 2009. DOI: 10.1002/9780470721582.
(104) Watts, J. F.; Wolstenholme, J. *An introduction to surface analysis by XPS and AES*, second edition; Wiley, 2020. DOI: 10.1002/9781119417651.
(105) Baer, D. R.; Artyushkova, K.; Cohen, H.; Easton, C. D.; Engelhard, M.; Gengenbach, T. R.; Greczynski, G.; Mack, P.; Morgan, D. J.; Roberts, A. XPS guide: Charge neutralization and binding energy referencing for insulating samples. *J. Vac. Sci. Technol. A* **2020**, *38* (3), 31204. DOI: 10.1116/6.0000057.
(106) Pertsin, A. J.; Pashunin, Y. Differential charging in XPS studies of polymer/metal interfaces. *Appl. Surf. Sci.* **1990**, *44* (3), 171–178. DOI: 10.1016/0169-4332(90)90047-4.
(107) Yu, X.-R.; Hantsche, H. Vertical differential charging in monochromatized small spot X-ray photoelectron spectroscopy. *Surf. Interface Anal.* **1993**, *20* (7), 555–558. DOI: 10.1002/sia.740200702.
(108) Baer, D. R.; Engelhard, M. H.; Gaspar, D. J.; Lea, A. S.; Windisch, C. F. Use and limitations of electron flood gun control of surface potential during XPS: two non-homogeneous sample types. *Surf. Interface Anal.* **2002**, *33* (10-11), 781–790. DOI: 10.1002/sia.1454.
(109) Walther, F.; Randau, S.; Schneider, Y.; Sann, J.; Rohnke, M.; Richter, F. H.; Zeier, W. G.; Janek, J. Influence of Carbon Additives on the Decomposition Pathways in Cathodes of Lithium Thiophosphate-Based All-Solid-State Batteries. *Chem. Mater.* **2020**, *32* (14), 6123–6136. DOI: 10.1021/acs.chemmater.0c01825.

(110) Gibson, J. S.; Narayanan, S.; Swallow, J. E. N.; Kumar-Thakur, P.; Pasta, M.; Lee, T.-L.; Weatherup, R. S. Gently does it!: in situ preparation of alkali metal-solid electrolyte interfaces for photoelectron spectroscopy. *Faraday Discuss.* **2022**, *236* (0), 267–287. DOI: 10.1039/d1fd00118c. Published Online: Aug. 25, 2022.
(111) Liu, Z.; Borodin, A.; Li, G.; Liu, X.; Li, Y.; Endres, F. X-ray Photoelectron Spectroscopy Probing of the Interphase between Solid-State Sulfide Electrolytes and a Lithium Anode. *J. Phys. Chem. C* **2020**, *124* (1), 300–308. DOI: 10.1021/acs.jpcc.9b06384.
(112) Wenzel, S.; Weber, D. A.; Leichtweiss, T.; Busche, M. R.; Sann, J.; Janek, J. Interphase formation and degradation of charge transfer kinetics between a lithium metal anode and highly crystalline $Li_7P_3S_{11}$ solid electrolyte. *Solid State Ion.* **2016**, *286*, 24–33. DOI: 10.1016/j.ssi.2015.11.034.
(113) Connell, J. G.; Fuchs, T.; Hartmann, H.; Krauskopf, T.; Zhu, Y.; Sann, J.; Garcia-Mendez, R.; Sakamoto, J.; Tepavcevic, S.; Janek, J. Kinetic versus Thermodynamic Stability of LLZO in Contact with Lithium Metal. *Chem. Mater.* **2020**, *32* (23), 10207–10215. DOI: 10.1021/acs.chemmater.0c03869.
(114) Liu, Z.; Li, G.; Borodin, A.; Liu, X.; Li, Y.; Endres, F. In situ X-ray photoelectron spectroscopy investigation of the solid electrolyte interphase in a $Li/Li_{6.4}Ga_{0.2}La_3Zr_2O_{12}/LiFePO_4$ all-solid-state battery. *J. Solid State Electrochem.* **2019**, *23* (7), 2107–2117. DOI: 10.1007/s10008-019-04296-4.
(115) Franke, E.; Neumann, H.; Zeuner, M.; Frank, W.; Bigl, F. Particle energy and angle distributions in ion beam sputtering. *Surf. Coat. Technol.* **1997**, *97* (1-3), 90–96. DOI: 10.1016/S0257-8972(97)00304-6.
(116) Wasa, K.; Kanno, I.; Kotera, H., Eds. *Handbook of sputter deposition technology*:*Fundamentals and applications for functional thin films, nanomaterials, and MEMS*, 2nd ed.; Elsevier, 2012.
(117) Bundesmann, C.; Neumann, H. Tutorial: The systematics of ion beam sputtering for deposition of thin films with tailored properties. *J. Appl. Phys.* **2018**, *124* (23), 231102. DOI: 10.1063/1.5054046.
(118) Kalanov, D.; Anders, A.; Bundesmann, C. Ion beam sputtering of silicon: Energy distributions of sputtered and scattered ions. *J. Vac. Sci. Technol. A* **2019**, *37* (5), 51507. DOI: 10.1116/1.5114973.
(119) Quérel, E.; Williams, N. J.; Seymour, I. D.; Skinner, S. J.; Aguadero, A. Operando Characterization and Theoretical Modeling of Metal|Electrolyte Interphase Growth Kinetics in Solid-State Batteries. Part I: Experiments. *Chem. Mater.* **2023**, *35* (3), 853–862. DOI: 10.1021/acs.chemmater.2c03130. Published Online: Jan. 20, 2023.
(120) Orazem, M. E.; Tribollet, B. *Electrochemical Impedance Spectroscopy*; John Wiley & Sons, Incorporated, 2017.
(121) Vadhva, P.; Hu, J.; Johnson, M. J.; Stocker, R.; Braglia, M.; Brett, D. J. L.; Rettie, A. J. E. Electrochemical Impedance Spectroscopy for All-Solid-State Batteries: Theory, Methods and Future Outlook. *ChemElectroChem* **2021**, *8* (11), 1930–1947. DOI: 10.1002/celc.202100108.
(122) Ohno, S.; Bernges, T.; Buchheim, J.; Duchardt, M.; Hatz, A.-K.; Kraft, M. A.; Kwak, H.; Santhosha, A. L.; Liu, Z.; Minafra, N.; Tsuji, F.; Sakuda, A.; Schlem, R.; Xiong, S.; Zhang, Z.; Adelhelm, P.; Chen, H.; Hayashi, A.; Jung, Y. S.; Lotsch, B. V.; Roling, B.; Vargas-Barbosa, N. M.; Zeier, W. G. How Certain Are the Reported Ionic Conductivities of Thiophosphate-Based Solid Electrolytes? An Interlaboratory Study. *ACS Energy Lett.* **2020**, *5* (3), 910–915. DOI: 10.1021/acsenergylett.9b02764.
(123) Tenhaeff, W. E.; Rangasamy, E.; Wang, Y.; Sokolov, A. P.; Wolfenstine, J.; Sakamoto, J.; Dudney, N. J. Resolving the Grain Boundary and Lattice Impedance of Hot-Pressed $Li_7La_3Zr_2O_{12}$ Garnet Electrolytes. *ChemElectroChem* **2014**, *1* (2), 375–378. DOI: 10.1002/celc.201300022.

(124) Braun, P.; Uhlmann, C.; Weber, A.; Störmer, H.; Gerthsen, D.; Ivers-Tiffée, E. Separation of the bulk and grain boundary contributions to the total conductivity of solid lithium-ion conducting electrolytes. *J Electroceram* **2017**, *38* (2-4), 157–167. DOI: 10.1007/s10832-016-0061-y.
(125) Milan, E.; Pasta, M. The role of grain boundaries in solid-state Li-metal batteries. *Mater. Futures* **2023**, *2* (1), 13501. DOI: 10.1088/2752-5724/aca703.
(126) Hertle, J.; Walther, F.; Mogwitz, B.; Schröder, S.; Wu, X.; Richter, F. H.; Janek, J. Miniaturization of Reference Electrodes for Solid-State Lithium-Ion Batteries. *J. Electrochem. Soc.* **2023**, *170* (4), 40519. DOI: 10.1149/1945-7111/accb6f.
(127) Costard, J.; Ender, M.; Weiss, M.; Ivers-Tiffée, E. Three-Electrode Setups for Lithium-Ion Batteries. *J. Electrochem. Soc.* **2017**, *164* (2), A80-A87. DOI: 10.1149/2.0241702jes.
(128) Ender, M.; Illig, J.; Ivers-Tiffée, E. Three-Electrode Setups for Lithium-Ion Batteries. *J. Electrochem. Soc.* **2017**, *164* (2), A71-A79. DOI: 10.1149/2.0231702jes.
(129) Simon, F. J.; Blume, L.; Hanauer, M.; Sauter, U.; Janek, J. Development of a Wire Reference Electrode for Lithium All-Solid-State Batteries with Polymer Electrolyte: FEM Simulation and Experiment. *J. Electrochem. Soc.* **2018**, *165* (7), A1363-A1371. DOI: 10.1149/2.0671807jes.
(130) Buschmann, H.; Berendts, S.; Mogwitz, B.; Janek, J. Lithium metal electrode kinetics and ionic conductivity of the solid lithium ion conductors "$Li_7La_3Zr_2O_{12}$" and $Li_{7-x}La_3Zr_{2-x}Ta_xO_{12}$ with garnet-type structure. *J. Power Sources* **2012**, *206*, 236–244. DOI: 10.1016/j.jpowsour.2012.01.094.
(131) Ender, M.; Weber, A.; Ellen, I.-T. Analysis of Three-Electrode Setups for AC-Impedance Measurements on Lithium-Ion Cells by FEM simulations. *J. Electrochem. Soc.* **2011**, *159* (2), A128-A136. DOI: 10.1149/2.100202jes.
(132) Ikezawa, A.; Fukunishi, G.; Okajima, T.; Kitamura, F.; Suzuki, K.; Hirayama, M.; Kanno, R.; Arai, H. Performance of $Li_4Ti_5O_{12}$-based reference electrode for the electrochemical analysis of all-solid-state lithium-ion batteries. *Electrochem. Commun.* **2020**, *116*, 106743. DOI: 10.1016/j.elecom.2020.106743.

# 7 Appendix

## 7.1 Supporting Information

### *7.1.1* Publication 1


Supporting Information

**Lithium-Metal Anode Instability of the Superionic Halide Solid Electrolytes and the Implications for Solid-State Batteries**

*Luise M. Riegger, Roman Schlem, Joachim Sann, Wolfgang G. Zeier,* and Jürgen Janek**

anie_202015238_sm_miscellaneous_information.pdf

WILEY-VCH

SUPPORTING INFORMATION

## Table of Contents



## Experimental Procedures

**Synthesis:** The syntheses of $Li_3InCl_6$ (LIC) and $Li_3YCl_6$ (LYC) were carried out in an argon inert-gas atmosphere. Stoichiometric amounts of LiCl, $InCl_3$ and $YCl_3$ (slight excess, see Schlem *et al.*[1]) were used as received. Both compounds were prepared using a mechanochemical approach in a planetary ball mill. LIC was prepared for a total of 99 cycles and LYC for a total of 198 cycles, with one cycle consisting of a 10 min milling step, followed by a 10 min rest step. Additionally, while LIC was used as prepared, LYC was subsequently annealed to ensure the full formation of the desired final phase, as it has been discussed previously that the final phase only forms partially during milling. The exact annealing procedure can be found in reference.[1]

**X-Ray diffraction:** The phase purity of the synthesized compounds was evaluated using X-ray diffraction techniques using an Empyrean powder diffractometer (PANalytical) with Cu-$K_\alpha$ radiation ($\lambda_1$= 1.54051Å, $\lambda_2$=1.54433 Å) in Bragg-Brentano geometry. Small amounts of the respective compound were placed on a (911)-oriented silicon disc and sealed with Kapton foil under Argon atmosphere to prevent decomposition during the measurement. The data collection was carried out using a step size 0.033° of and an exposure time of 150 s.

**XPS setup and data analysis:** The XPS measurements were performed with a PHI 5000 Versaprobe Scanning ESCA Microprobe (Physical Electronics) with monochromatized Al $K_\alpha$ X-ray source (beam diameter 200 µm, X-ray power of 50 W). The detail spectra were measured with a step time of 50 ms, a step size of 0.2 eV and an analyzer pass energy of 23.5 eV. During the measurement, the pressure was in the range of $10^{-7}$ to $10^{-6}$ Pa and the sample surface was charge neutralized with slow electrons and argon ions. The samples were prepared in a glovebox (MBraun, $p(O_2)$ < 0.1ppm, $p(H_2O)$ < 0.1ppm) and a transfer shuttle was used to transport the samples from the glovebox to the analysis chamber. Lithium metal foil from Rockwood Lithium was cleaned mechanically by scraping and used as a target. An argon ion current of 4 $\mu$A and an acceleration voltage of 4 kV was used for sputtering. The measuring setup was already described by Wenzel *et al.*.[2] Data analysis was performed with the help of CasaXPS software and the charge correction was done using the C1s signal at 284.8 eV.
Indium foil with a purity of 99,999 % was purchased from ChemPUR GmbH. LiCl (99,9 % purity), $YCl_3$ (99,999 % purity) were bought from Alpha Aesar and $InCl_3$ (99.999 % purity) was bought from Sigma Aldrich.

**Impedance measurement:** For measuring the stability of $Li_3InCl_6$ and $Li_3YCl_6$ against lithium metal, a symmetrical cell was assembled with a radius of 1 cm. For this, 60 mg of $Li_3XCl_6$ (X=In, Y) were pressed at 3 tons for 30 s to obtain a pellet and Lithium foil (Honjo Metal Co., Ltd.) with a diameter of 9 mm was contacted with both pellet sides. The conductivity of $Li_3YCl_6$ was 9.5E-5 $Scm^{-1}$.[1] During the measurement, a constant pressure of 12,7 MPa was applied. The impedance measurement was carried out at 25 °C with a SP300 impedance analyzer (BioLogic) at frequencies from 7 MHz to 500 mHz with an amplitude of 5 mV.
A Li|$Li_6PS_5Cl$|$Li_3InCl_6$|$Li_6PS_5Cl$|Li symmetric cell isostatically pressed at 360 MPa was used for measuring the transference resistance between $Li_6PS_5Cl$ and $Li_3InCl_6$. The cell had a radius of 1 cm and lithium metal was used for contacting. The impedance measurement was carried out with an Alpha-A high performance modular measurement System (Novocontrol Technologies) between 25 °C and -100 °C with a frequency range of 0.01 Hz to 1 MHz and an amplitude of 10 mV.

## Results and Discussion

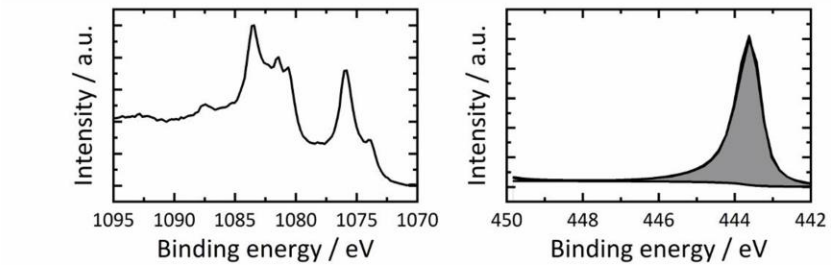


**Figure S 1.** X-ray photoelectron In-3d and Auger In-MNN spectra of pure indium metal used as a reference for the interpretation of the $Li_3InCl_6$ spectra.

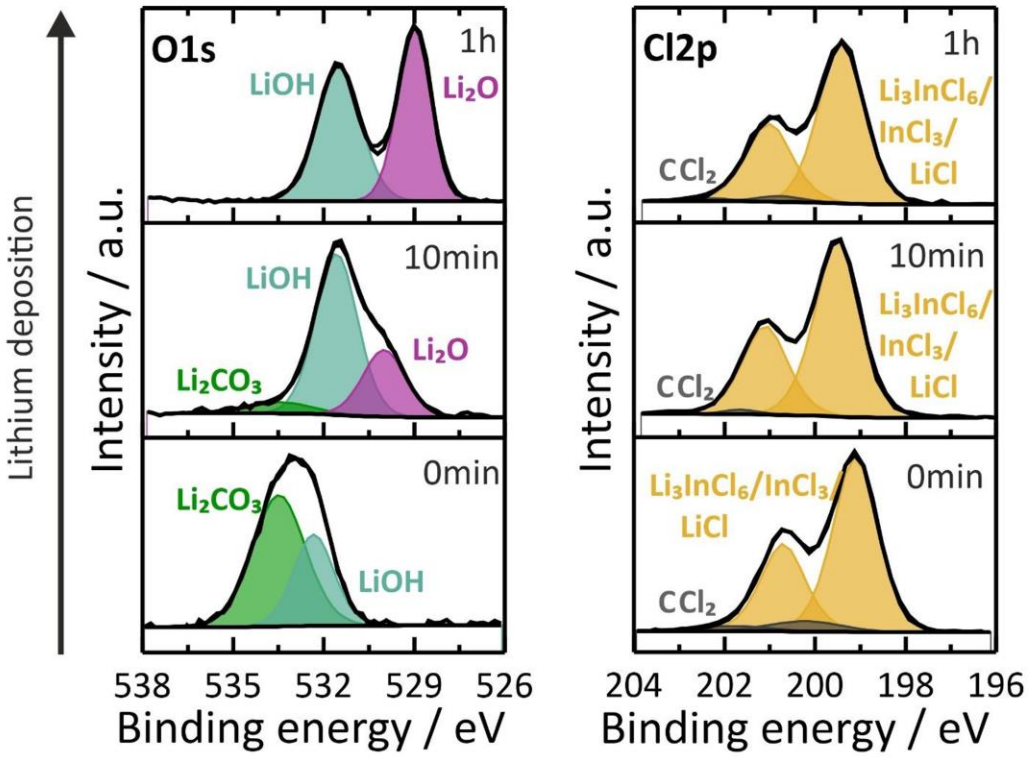


**Figure S 2.** X-ray photoelectron O-1s and Cl-2p spectra of a pristine $Li_3InCl_6$ sample and after 10 min and 1 h of lithium deposition, respectively. The $Li_3InCl_6$ decomposes in contact with lithium metal. Part of the lithium reacts with remaining oxygen in the UHV chamber to $Li_2O$. The Cl-2p spectra shift towards higher binding energies during the one-hour lithium deposition indicating that transient intermediates such as $InCl_3$, $InCl_2$ and InCl form during the reduction of $In^{3+}$ to $In^0$. However, an exact assignment of the intermediate states is not possible. The final product of the complete reaction between lithium and $Li_3InCl_6$ cannot be seen in this experiment, as the total duration of the experiment would not be feasible.

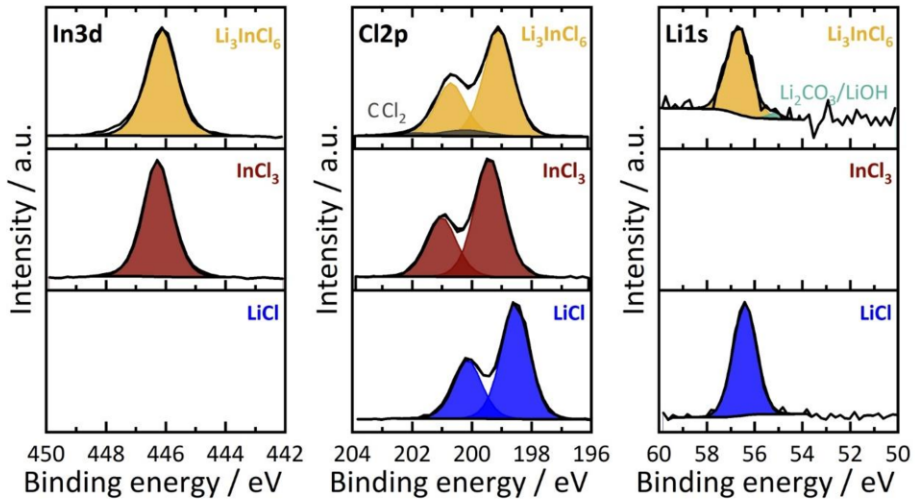


**Figure S 3.** X-ray photoelectron In-3d, Cl-2p and Li-1s reference spectra of $Li_3InCl_6$, $InCl_3$ and LiCl. The $Li_3InCl_6$ shows decontamination with $Li_2CO_3$/LiOH in the Li-1s spectrum and with $CCl_2$ in the Cl-2p spectrum due to the preparation process or surface contaminations.

**Table S 1.** Fitting parameters of the XP spectra In-3d, Cl-2p and Li-1s for $Li_3InCl_6$, $InCl_3$ and LiCl shown in Figure S 3.

| | **In3d** | | | **Cl2p** | | | **Li1s** | | |
|---|---|---|---|---|---|---|---|---|---|
| | $Li_3InCl_6$ | $InCl_3$ | LiCl | $Li_3InCl_6$ | $InCl_3$ | LiCl | $Li_3InCl_6$ | $InCl_3$ | LiCl |
| **Position / eV** | 446.1 | 446.3 | / | 199.2 | 199.4 | 198.5 | 56.6 | / | 56.4 |
| **FWHM / eV** | 1.2 | 1.1 | / | 1.3 | 1.2 | 1.1 | 1.2 | / | 1.1 |

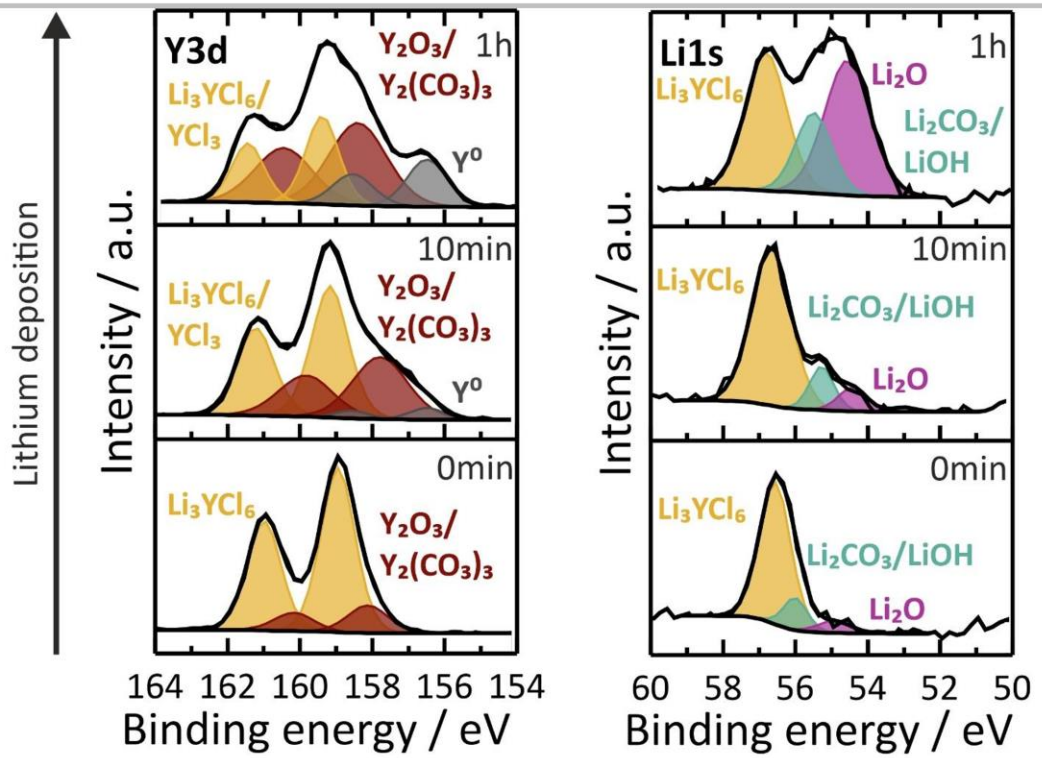


**Figure S 4.** X-ray photoelectron Y3-d and Li-1s spectra of a pristine $Li_3YCl_6$ sample and after 10 min and 1 h of lithium metal deposition, respectively. The $Li_3YCl_6$ decomposes in contact with lithium metal to metallic yttrium, which readily reacts with neighbouring species to $Y_2O_3$ or $Y_2(CO_3)_3$. The signal of pristine $Li_3YCl_6$ decreases indicating the coverage of the solid electrolyte and a growing interphase. Part of the lithium reacts with remaining oxygen in the UHV chamber to $Li_2O$.

**Table S 2.** Fitting parameters for the XP spectra Y-3d and Li-1s for the pristine sample and after 10 min and 1 h of lithium deposition shown in Figure S4.

| | Y3d | | | Li1s | | |
|---|---|---|---|---|---|---|
| | $Li_3YCl_6$ / $YCl_3$ | $Y_2O_3$ / $Y_2(CO_3)_3$ | $Y^0$ | $Li_3YCl_6$ | $Li_2CO_3$ / LiOH | $Li_2O$ |
| | | | **pristine** | | | |
| **Position / eV** | 159.0 | 158.1 | / | 56.6 | 56.0 | 54.9 |
| **FWHM / eV** | 1.1 | 1.3 | / | 1.0 | 0.8 | 1.1 |
| | | | **10 min** | | | |
| **Position / eV** | 159.2 | 157.8 | 156.5 | 56.7 | 55.3 | 54.4 |
| **FWHM / eV** | 1.2 | 1.8 | 1.1 | 1.3 | 0.8 | 0.9 |
| | | | **1 h** | | | |
| **Position / eV** | 159.4 | 158.3 | 156.5 | 56.8 | 55.5 | 54.6 |
| **FWHM / eV** | 1.1 | 1.8 | 1.3 | 1.3 | 1.3 | 1.4 |

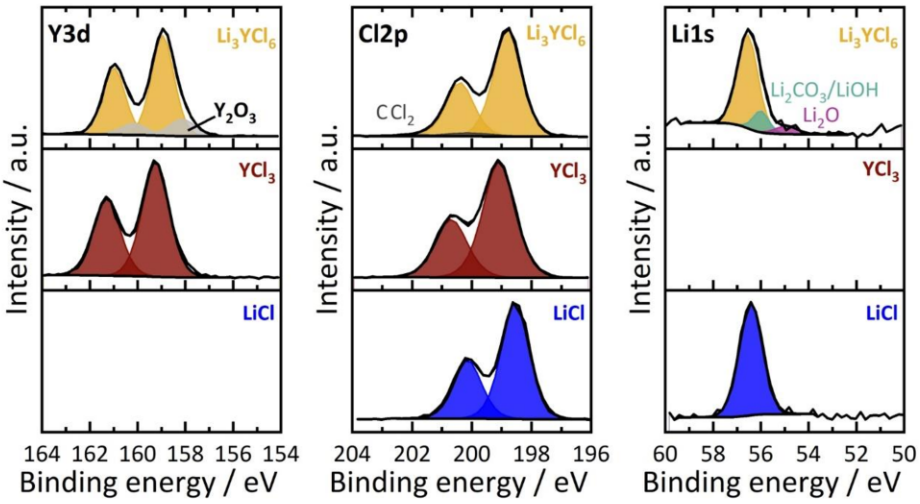


**Figure S 5.** X-ray photoelectron Y-3d, Cl-2p and Li-1s reference spectra of $Li_3YCl_6$, $YCl_3$ and LiCl. The $Li_3YCl_6$ shows decontamination with $Y_2O_3$ (Y-3d spectrum), $Li_2CO_3$/LiOH and $Li_2O$ (Li-1s spectrum) and with $CCl_2$ (Cl-2p spectrum) due to the preparation process or surface decontaminations.

**Table S 3.** Fitting parameters of the XP spectra Y-3d, Cl-2p and Li-1s for $Li_3YCl_6$, $InCl_3$ and LiCl shown in Figure S 5.

| | Y3d | | | Cl2p | | | Li1s | | |
|---|---|---|---|---|---|---|---|---|---|
| | $Li_3YCl_6$ | $YCl_3$ | LiCl | $Li_3YCl_6$ | $YCl_3$ | LiCl | $Li_3YCl_6$ | $YCl_3$ | LiCl |
| **Position / eV** | 159.0. | 159.2 | / | 198.8 | 199.1 | 198.5 | 56.6 | / | 56.4 |
| **FWHM / eV** | 1.1 | 1.3 | / | 1.1 | 1.3 | 1.1 | 1.0 | / | 1.1 |

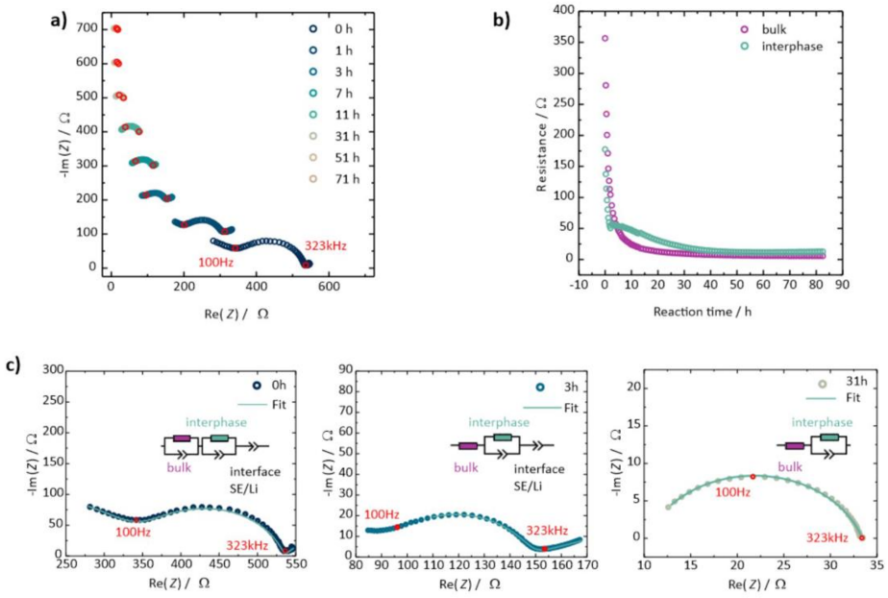


**Figure S 6.** a) Temporal evolution of the impedance response of a symmetric Li|$Li_3YCl_6$|Li cell stacked without rescaling and shifted by 100 Ω for each spectrum. b) Temporal evolution of the resistances of the different processes as a function of 15 minutes intervals at the beginning, to study the initial reaction in detail, while further data points were collected after 30 min and later after each hour. c) The collected time-resolved spectra were fitted for the first three hours of measurement with an equivalent circuit consisting of two in series connected constant phase elements that are each in parallel with a resistor followed by a constant phase element connected in series. After three hours of measurement the contribution of the volume could not be resolved, therefore the first resistor/constant phase element was replaced by a resistor. After twenty hours of measurement, the contribution of the interface between lithium and solid electrolyte disappears. Therefore, an equivalent circuit consisting of a resistor and a series-connected constant phase element connected in parallel with a resistor was used.

## References

[1] R. Schlem, S. Muy, N. Prinz, A. Banik, Y. Shao‐Horn, M. Zobel, W. G. Zeier, *Adv. Energy Mater.* **2020**, *10*, 1903719.
[2] S. Wenzel, T. Leichtweiss, D. Krüger, J. Sann, J. Janek, *Solid State Ionics* **2015**, *278*, 98.

## Author Contributions

L. Riegger:
data curation and data analysis of XPS measurements (lead)
data curation and data analysis of temporal evolution of the impedance response of Li|$Li_3InCl_6$|Li and Li|$Li_3YCl_6$|Li cells (lead)
writer of original draft (lead)

R. Schlem:
material synthesis (lead)
data curation and data analysis of transfer resistances of $Li_6PS_5Cl$|$Li_3InCl_6$|$Li_6PS_5Cl$ (lead)
data analysis of temporal evolution of the impedance response of Li|$Li_3InCl_6$|Li and Li|$Li_3YCl_6$|Li cells (supporting)
writer of original draft (supporting)

Dr. J. Sann:
validation of data analysis of XPS measurements (lead)

Prof. W. G. Zeier:
validation of data analysis of the impedance measurements (lead)
project administration (equal)

Prof. J. Janek:
validation of data analysis of the impedance measurements (supporting)

WILEY-VCH

SUPPORTING INFORMATION

Editing manuscript text (supporting)
project administration (equal)
funding acquisition (lead)

### *7.1.2* Publication 2

# Supporting Information –

# Instability of $Li_7SiPS_8$ Solid Electrolyte at the Lithium Metal Anode and Interphase Formation

*Luise M. Riegger[1,2], Svenja-K. Otto[1,2], Marcel Sadowski[3], Sven Jovanovic[4], Olaf Kötz[1,2], Sascha Harm[6,7], Lucas G. Balzat[6,7], Steffen Merz[4], Simon Burkhardt[1,2], Felix H. Richter[1,2], Joachim Sann[1,2], Rüdiger-A. Eichel[4,5], Bettina V. Lotsch[6,7], Josef Granwehr[4], Karsten Albe[3] and Jürgen Janek[1,2*]*

[1] Institute of Physical Chemistry, Justus-Liebig-University Giessen, Heinrich-Buff-Ring 17, D-35392 Giessen, Germany.

[2] Center for Materials Research (ZfM), Justus-Liebig-University Giessen, Heinrich-Buff-Ring 16, D-35392 Giessen, Germany.

[3] Institute of Materials Science, Technical University of Darmstadt, Otto-Berndt-Str. 3, D-64287 Darmstadt, Germany.

[4] Forschungszentrum Jülich GmbH, IEK-9: Fundamental Electrochemistry, Ostring O10, D-52425 Jülich, Germany.

[5] Institute of Physical Chemistry, RWTH Aachen University, Landoltweg 2, D-52056 Aachen, Germany

[6] Max Planck Institute for Solid State Research, Heisenbergstr. 1, D-70569 Stuttgart, Germany.

[7] Department of Chemistry, Ludwig-Maximilians-Universität München, Butenandtstr. 5-13, D-81377 München, Germany.

**This PDF File includes:**

**Figure S13:** Side view of the ordered interface formed during a 60 ps simulations at 500 K and slices of the layers.

**Figure S14:** Electronic density of states (eDOS) of the interface model with an ordered and an amorphous interface as well as possible reaction products.

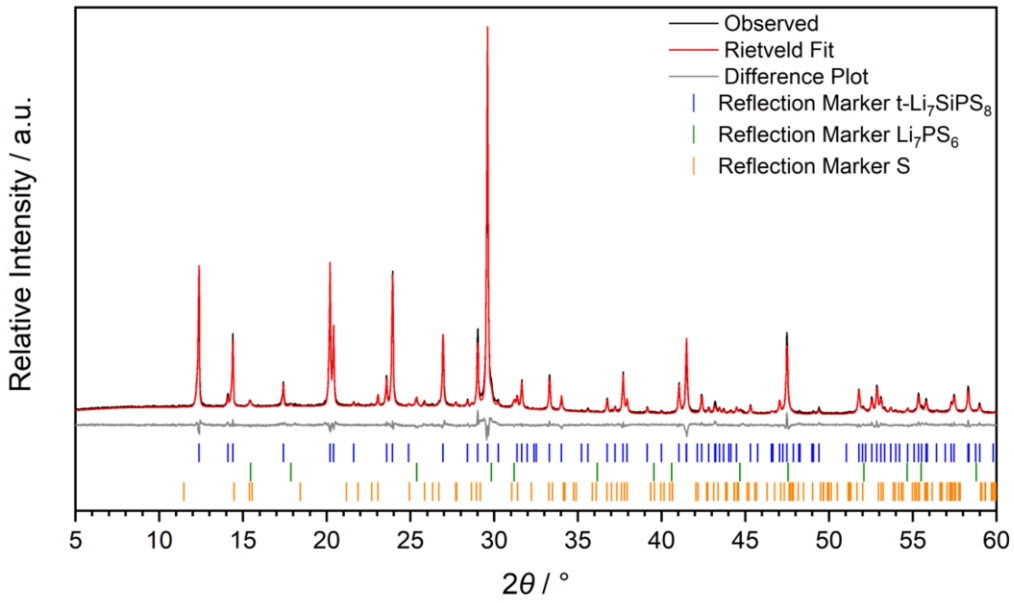


**Figure S1.** Rietveld refinement plot for the t-$Li_7SiPS_8$ used for the stripping/plating as well as the temporal impedance evolution experiments. Shown are the observed XRD data (black), the Rietveld fit (red), the difference plot (grey), and the reflection markers obtained from the t-$Li_7SiPS_8$ (blue), $Li_7PS_6$ (green), and S (orange) models. The crystallographic data of the t-$Li_7SiPS_8$, $Li_7PS_6$, and S models used for the Rietveld refinement can be found in references 1–3.[1–3]

**Table S1.** Crystallographic data from the Rietveld refinement of t-$Li_7SiPS_8$ used for the stripping/plating as well as the temporal impedance evolution experiments. Small side fractions of $Li_7PS_6$ and S are present. Standard deviations are given in parentheses.

| | | |
|---|---|---|
| Phase / wt% | t-$Li_7SiPS_8$ | 94.3(2) |
| Space group | | $P4_2/nmc$ (No. 137) |
| Lattice parameters | $a$ | 8.7005(1) |
| | $c$ | 12.5630(2) |
| Volume [Å$^3$] | | 951.01(3) |
| $R_{Bragg}$ | | 1.97 % |
| Phase / wt% | $Li_7PS_6$ | 3.6(1) |
| Space group | | $F\bar{4}3m$ (No. 216) |
| Lattice parameters | $a$ | 9.9278(7) |
| Volume [Å$^3$] | | 978.4(2) |
| $R_{Bragg}$ | | 4.32 % |
| Phase / wt% | S | 2.1(1) |
| Space group | | $Fddd$ (No. 70) |
| Lattice parameters | $a$ | 10.473(1) |
| | $b$ | 12.870(4) |
| | $c$ | 24.486(7) |
| Volume [Å$^3$] | | 3300(1) |
| $R_{Bragg}$ | | 1.81 % |
| Diffractometer | | STOE STADI P, $CuK_{\alpha 1}$ radiation, Debeye–Scherrer geometry |
| Refined $2\theta$ region [°] | | 5.00–60.68 |
| $R_p$ | | 4.06 % |
| $R_{wp}$ | | 5.50 % |
| $R_{exp}$ | | 3.25 % |
| GooF | | 1.693 |
| No. of refined parameters | | 55 |
| No. of bckgrnd. parameters | | 14 |

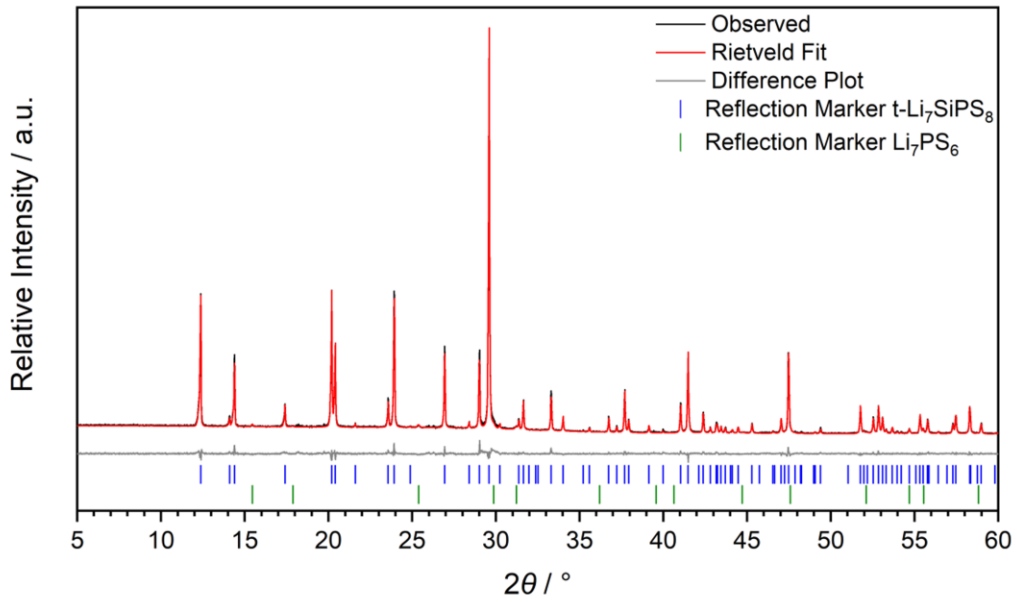


**Figure S2.** Rietveld refinement plot for the t-$Li_7SiPS_8$ used for XPS, TOF-SIMS, and NMR analysis. Shown are the observed XRD data (black), the Rietveld fit (red), the difference plot (grey), and the reflection markers obtained from the t-$Li_7SiPS_8$ (blue), and $Li_7PS_6$ (green) models. The crystallographic data of the t-$Li_7SiPS_8$, and $Li_7PS_6$ models used for the Rietveld refinement can be found in references 1 and 2.[1,2]

**Table S2.** Crystallographic data from the Rietveld refinement of t-$Li_7SiPS_8$ used for XPS, TOF-SIMS and NMR analysis. A small side fraction of $Li_7PS_6$ is present. Standard deviations are given in parentheses.

| | | |
|---|---|---|
| Phase/ wt% | t-$Li_7SiPS_8$ | 98.5(1) |
| Space group | | $P4_2/nmc$ (No. 137) |
| Lattice parameters | $a$ | 8.7017 (1) |
| | $c$ | 12.564(1) |
| Volume [Å$^3$] | | 951.38(2) |
| $R_{Bragg}$ | | 1.79 % |
| Phase / wt% | $Li_7PS_6$ | 1.5(1) |
| Space group | | $F\bar{4}3m$ (No. 216) |
| Lattice parameters | $a$ | 9.920(1) |
| Volume [Å$^3$] | | 976.3(4) |
| $R_{Bragg}$ | | 6.23 % |
| Diffractometer | | STOE STADI P, $CuK_{\alpha 1}$ radiation, Debeye–Scherrer geometry |
| Refined $2\theta$ region [°] | | 5.00–60.68 |
| $R_p$ | | 3.69 % |
| $R_{wp}$ | | 4.96 % |
| $R_{exp}$ | | 3.33 % |
| GooF | | 1.490 |
| No. of refined parameters | | 43 |
| No. of bckgrnd. parameters | | 14 |

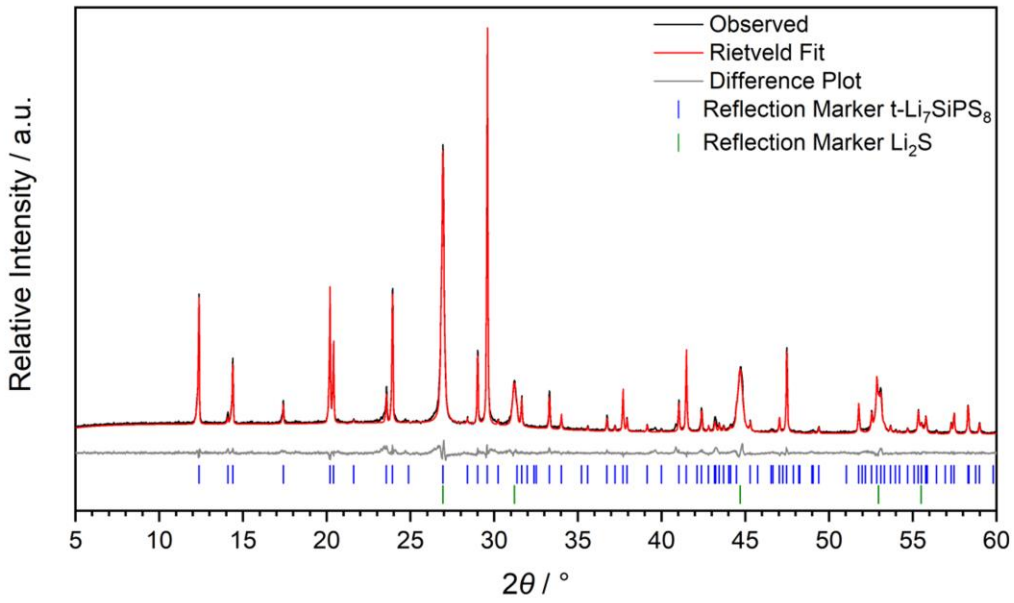


**Figure S3.** Rietveld refinement plot for the t-$Li_7SiPS_8$ after the reaction with liquid lithium. Shown are the observed XRD data (black), the Rietveld fit (red), the difference plot (grey), and the reflection markers obtained from the t-$Li_7SiPS_8$ (blue), and $Li_2S$ (green) models. The crystallographic data of the t-$Li_7SiPS_8$, and $Li_2S$ models used for the Rietveld refinement can be found in references 1 and 4.[1,4]

**Table S3.** Crystallographic data from the Rietveld refinement of t-$Li_7SiPS_8$ after the reaction with liquid lithium. Standard deviations are given in parentheses.

| | | |
|---|---|---|
| Phase / wt% | t-$Li_7SiPS_8$ | 55.0(3) |
| Space group | | $P4_2/nmc$ (No. 137) |
| Lattice parameters | $a$ | 8.70183(9) |
| | $c$ | 12.564(2) |
| Volume [Å$^3$] | | 951.42(2) |
| $R_{Bragg}$ | | 2.16 % |
| Phase / wt% | $Li_2S$ | 45.0(3) |
| Space group | | $Fm\bar{3}m$ (No. 225) |
| Lattice parameters | $a$ | 5.7312(1) |
| Volume [Å$^3$] | | 188.25(1) |
| $R_{Bragg}$ | | 0.41 % |
| Diffractometer | | STOE STADI P, $CuK_{\alpha 1}$ radiation, Debeye–Scherrer geometry |
| Refined 2$\theta$ region [°] | | 5.00–60.68 |
| $R_p$ | | 4.31 % |
| $R_{wp}$ | | 5.88 % |
| $R_{exp}$ | | 3.31 % |
| GooF | | 1.772 |
| No. of refined parameters | | 50 |
| No. of bckgrnd. parameters | | 15 |

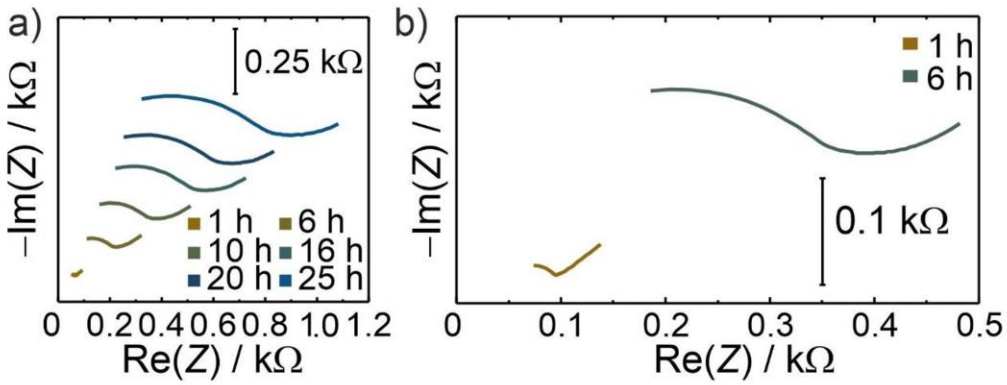


**Figure S4.** Close-up of the stacked Nyquist plots of Fig. 1b) and Fig. d). For a) the first 25 h of alternating stripping and plating with a current density of 0.1 mA $cm^{-2}$ and b) the first 6 h of alternating stripping and plating with a current density of 1 mA $cm^{-2}$.

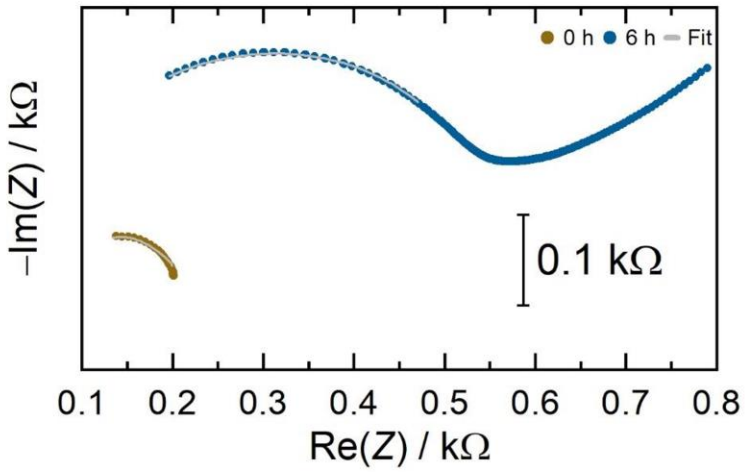


**Figure S5.** Close-up of the stacked Nyquist plots of Fig. 2.

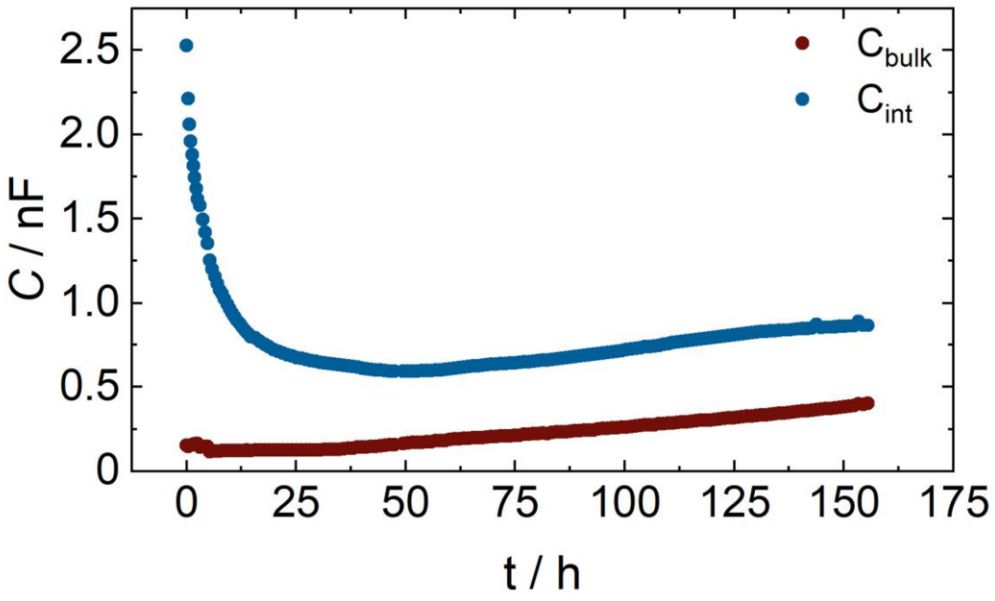


**Figure S6**. Capacitances of the bulk $C_{bulk}$ and the interphase $C_{int}$ of the fit shown in Fig. 2.

**Table S4.** Calculation of the change of the SE bulk resistance $R_{bulk}$. This calculation is based on the assumption that 3 µm of lithium reacted at each electrode side in the ToF-SIMS measurement during three weeks. The resulting −0.764 Ω are negligible compared to the bulk resistance of 96.77 Ω.

| | |
|---|---|
| $\sigma(Li_7SiPS_8)$ / mS·cm$^{-1}$ | 1 |
| $A$ / cm² | 0.785 |
| $\Delta d$ / µm | −6 |
| $\Delta R = \left(\frac{\Delta d}{\sigma \cdot A}\right)$ / Ω | −0.764 |

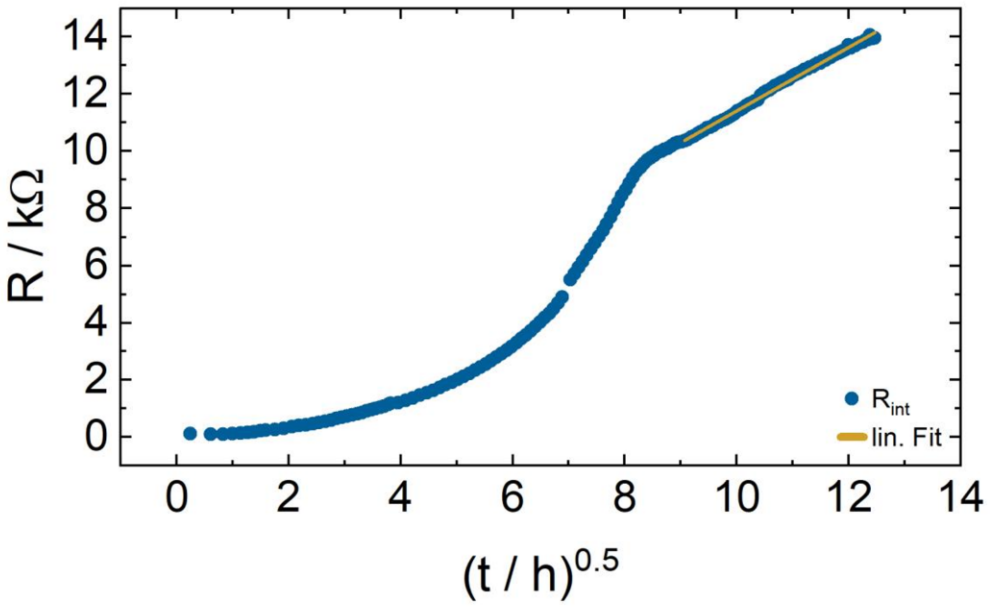


**Figure S7**. $R_{int}$ shown in Figure 2 plotted *vs*. square root of time to determine the parabolic growth rate.

**Table S5.** Fit parameters of the linear Fit shown in Figure S3.

| | Lin. Fit |
|---|---|
| Equation | $(R_{int} / \Omega) = a + b \cdot (t / h)^{0.5}$ |
| Intersection with the *y*-axis (*a*) | 314.26 |
| Slope (*b*) | 1109.71 |
| Pearson *R* | 0.998 |

**Table S6.** Calculated detection limits for phosphorus in a matrix of the decomposition products sulfur (S), silicon (Si), lithium (Li), and oxygen (O) using the equation described by Shard.[5] Here, the parameters $D$, $B$, $\beta$, $\alpha$, $s_i$, $s(P)$, and $A_i$, represent the detection limit, the standard deviation of the measured background intensity, the step size, the detection limit scaling factor, the relative sensitivity factors of each element and of phosphorus as well as the area under the signal of each element, respectively.

| | pristine | 15 min Li deposition | 2 h Li deposition |
|---|---|---|---|
| Equation | $D = \frac{B}{B + (\beta^{0.5} \cdot s(\mathrm{P})/\alpha) \cdot \sum(A_i/s_i)}$ | | |
| Detection limit scaling factor $\alpha$ / $eV^{0.5}$ | 9 | | |
| step size $\beta$ / eV | 0.20 | | |
| Standard deviation of the measured background intensity $B$ / counts | 0.00143 | 0.00143 | 0.00477 |
| Relative sensitivity factor $s$(P) | 0.604625 | | |
| Area $A$ (S) / counts | 262.2 | 250.48 | 223.49 |
| Relative sensitivity factor $s$(S) | 0.819531 | | |
| Area $A$ (Si) / counts | 19.41 | 12.98 | 9.97 |
| Relative sensitivity factor $s$(Si) | 0.42872 | | |
| Area $A$ (Li) / counts | 7.47 | 9.06 | 10.07 |
| Relative sensitivity factor $s$(Li) | 0.028 | | |
| Area $A$ (O) / counts | 78.15 | 51.89 | 32.84 |
| Relative sensitivity factor $s$(O) | 0.733 | | |
| Detection limit $D$ / at-% | 0.04 | 0.04 | 0.05 |

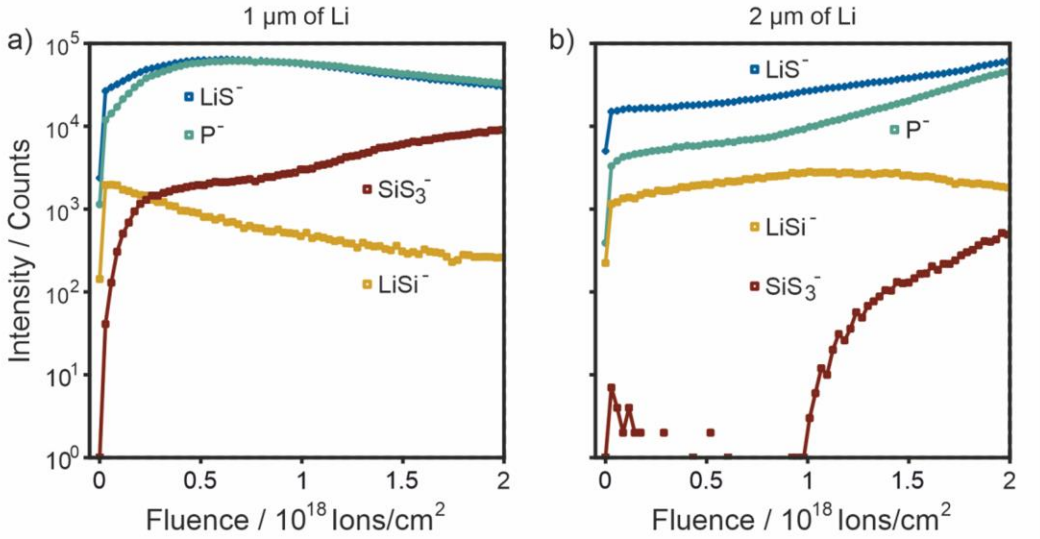


**Figure S8.** ToF-SIMS depth profile of t-$Li_7SiPS_8$ with a) 1 µm and b) 2 µm of deposited Li. Measurements were started directly after lithium deposition.

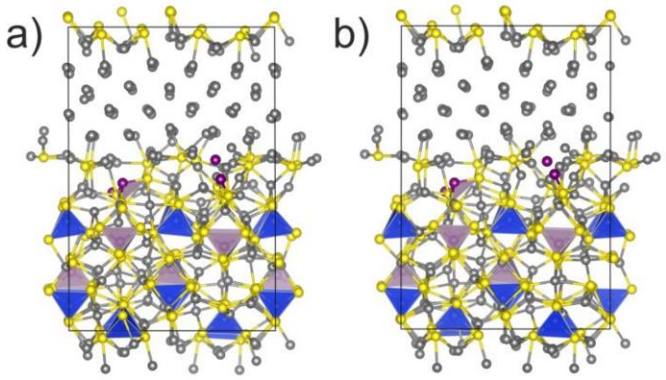


**Figure S9.** Two t-$Li_7SiPS_8$ | Li interface models, statically optimized using DFT calculations. Compared to the structure shown in a), the structure in b) was prepared with slightly increased slab separation distance at the $PS_4^{3-}$-rich interface. Still, the resulting structure after the optimization seems to be independent of the initial slab separation distance. The color coding is the same as in the main text. Li (gray), Si (blue), P (purple), S (yellow).

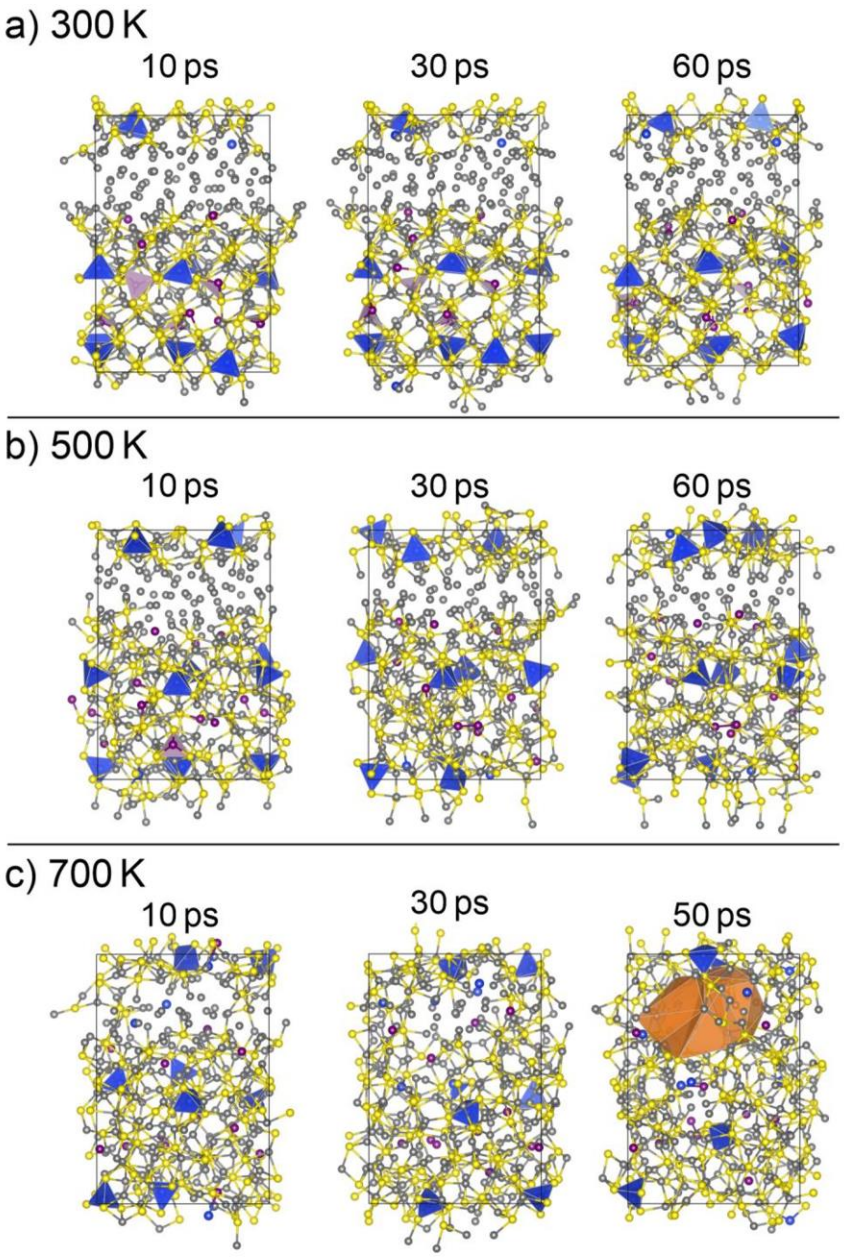


**Figure S10**. Models of amorphous interfaces obtained from AIMD simulations at different temperatures and times. The color coding is the same as in the main manuscript. Li (gray), Si (blue), P (purple), S (yellow).

**Table S7**. Volume change for the reaction of t-$Li_7SiPS_8$ with Li metal assumed to form $Li_2S$, $Li_3P$ and $Li_4SiS_4$. The amount of the precursor corresponds to the actual numbers used for the explicit interface modeling via DFT. The table lists the ideal bulk volume $V$, normalized per formula unit, and the expected total volumes $V_{tot}$ for the starting materials and assumed products.

| | Precursor | | → | Products | | | |
|---|---|---|---|---|---|---|---|
| | 12 $Li_7SiPS_8$ | 150 Li | → | 48 $Li_2S$ | 12 $Li_3P$ | 12 $Li_4SiS_4$ | 54 Li |
| $V$ [Å$^3$ / formula unit] | 323.50 | 20.04 | → | 46.33 | 58.22 | 166.56 | 20.04 |
| $V_{tot}$ [Å$^3$] | 6888.00 | | → | 6003.36 | | | |

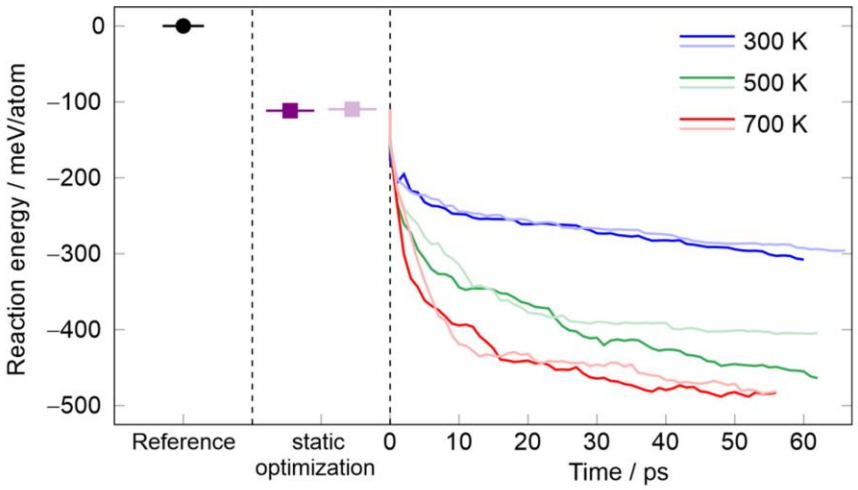


**Figure S11.** Reaction energies at different stages of the calculations. The sum of the individual t-$Li_7SiS_8$ and lithium metal slabs served as reference energy. The deep green line belongs to the interface model where the formation of an ordered interphase has been observed. The remaining structures led to amorphous interphases.

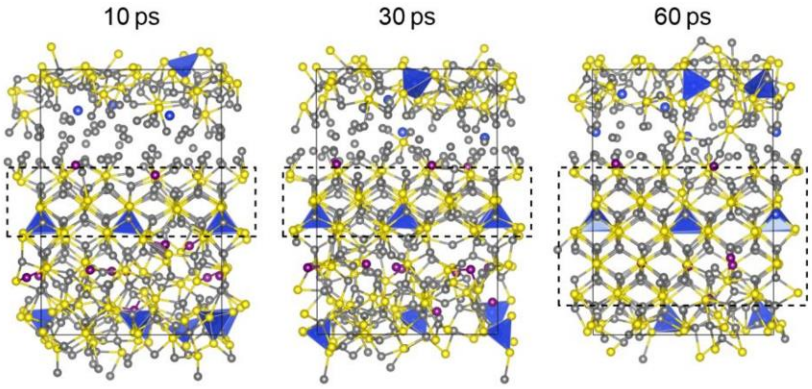


**Figure S12.** The ordered interphase at different time steps. The color coding is the same as in the main manuscript. Li (gray), Si (blue), P (purple), S (yellow).

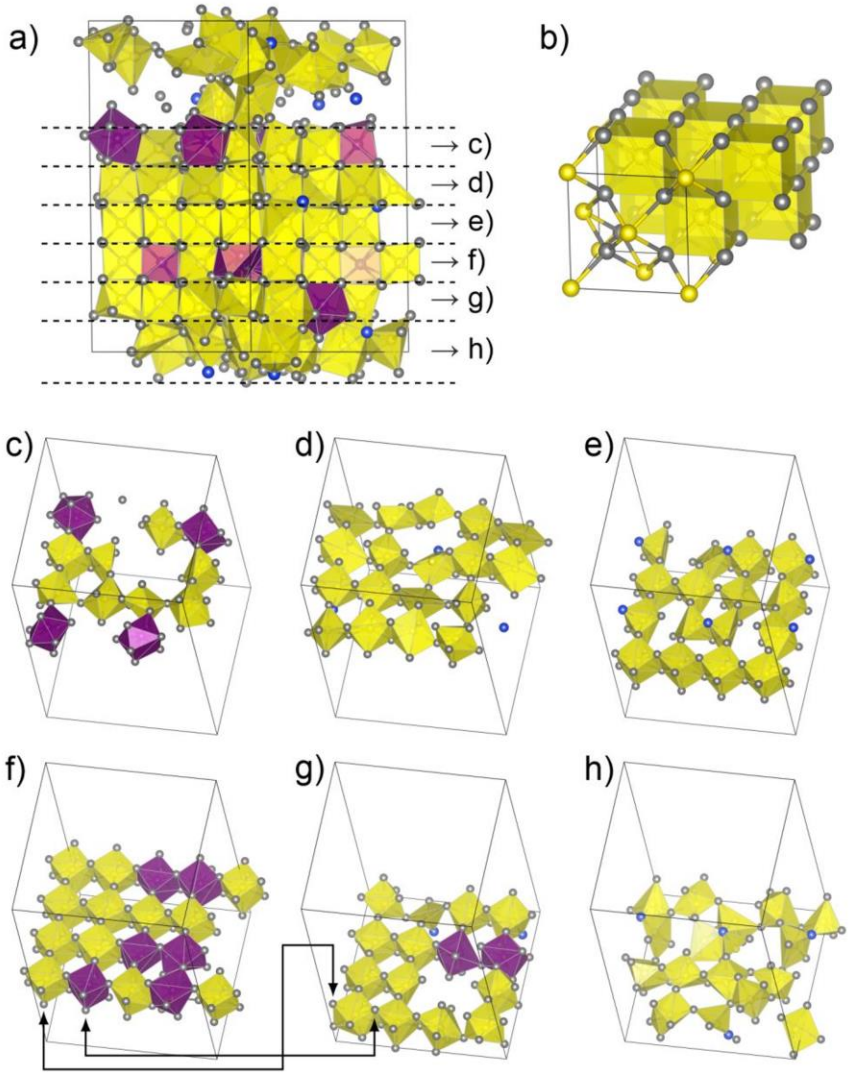


**Figure S13.** a) Side view of the ordered interface, mostly consisting of $Li_2S$, that formed during a 60 ps simulation at 500 K. b) Structural model of bulk $Li_2S$ with its regular $SLi_8$ coordination polyhedra. c)-h) Slices of the layers that are indicated in part a) of the figure. Arrows in f) and g) are a guide to the eyes to indicate the connection between the two slices. Color coding: Li (gray), Si (blue), P (purple), S (yellow), $SLi_x$ coordination polyhedra (yellow), $PLi_x$ coordination polyhedra (purple). Note that $SiS_4^{4-}$ and $SiS_3^{2-}$ units are also embedded in the ordered $Li_2S$ interface, but cannot be visualized simultaneously with the remaining coordination polyhedra.

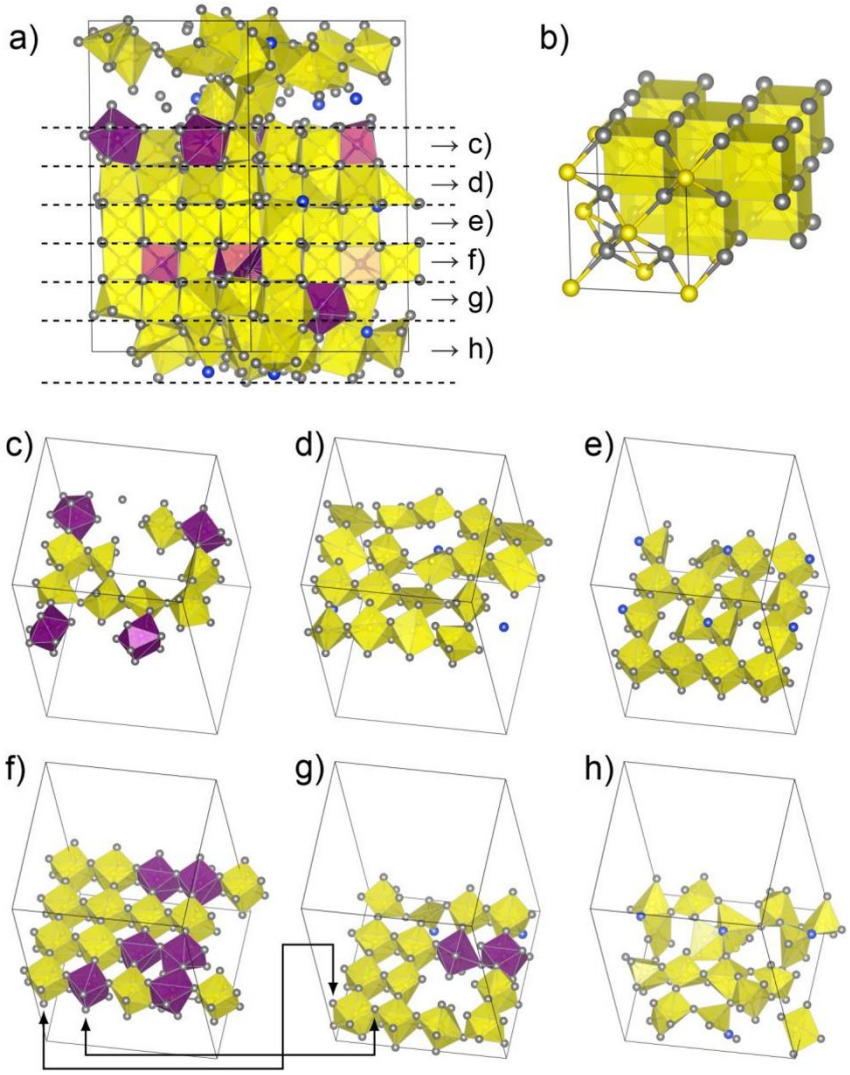


**Figure S13.** a) Side view of the ordered interface, mostly consisting of $Li_2S$, that formed during a 60 ps simulation at 500 K. b) Structural model of bulk $Li_2S$ with its regular $SLi_8$ coordination polyhedra. c)-h) Slices of the layers that are indicated in part a) of the figure. Arrows in f) and g) are a guide to the eyes to indicate the connection between the two slices. Color coding: Li (gray), Si (blue), P (purple), S (yellow), $SLi_x$ coordination polyhedra (yellow), $PLi_x$ coordination polyhedra (purple). Note that $SiS_4^{4-}$ and $SiS_3^{2-}$ units are also embedded in the ordered $Li_2S$ interface, but cannot be visualized simultaneously with the remaining coordination polyhedra.

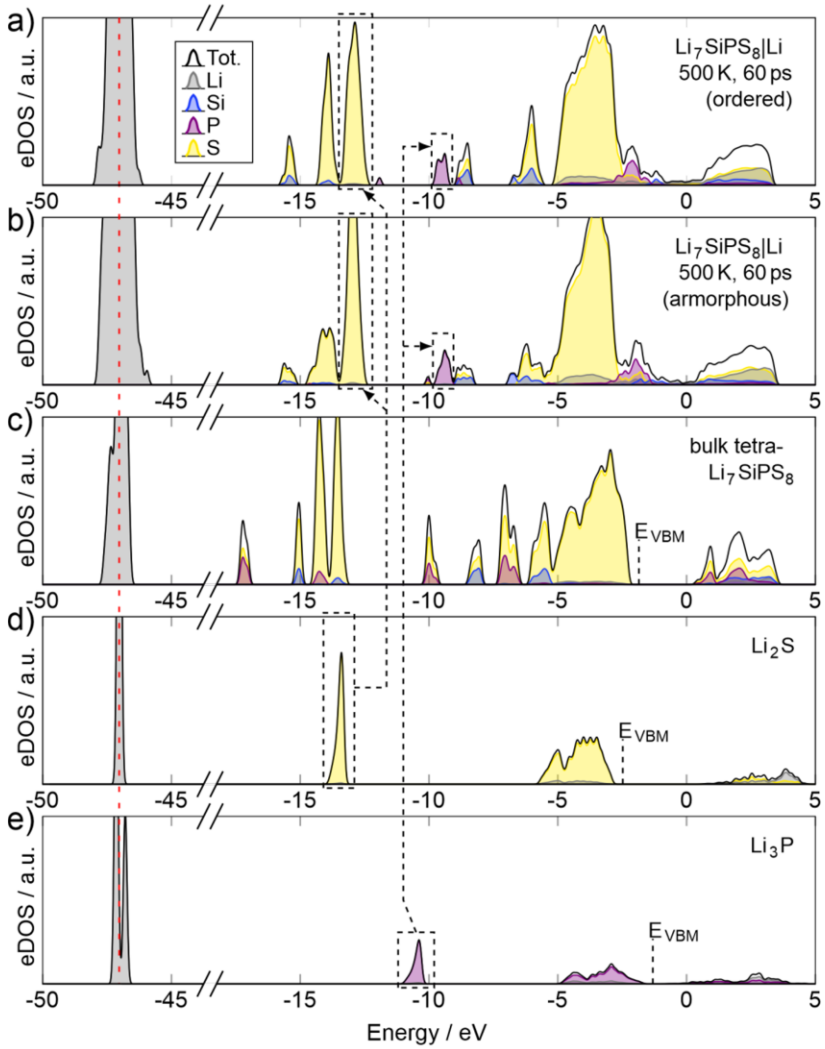


**Figure S14.** Electronic density of states (eDOS) of a) the interface model with an ordered interface, b) an exemplary interface model with amorphous interphase, c) bulk t-$Li_7SiPS_8$, d) $Li_2S$, and e) $Li_3P$. Conventionally, eDOS are shifted such that the valence band maximum (VBM) is located at an energy of zero. This is the case for a) and b). For a better comparison, the eDOS of c), d) and e) have been shifted such that the Li(1s) core levels coincide with the ones of the interface model (red dashed line). Selected features that are found in the interface models as well as in the binary compounds have been marked as a guide to the eye. The metallic character observed in a) and b) is attributed to the thin remaining Li metal layer in the interface models.

REFERENCES

(1) Harm, S.; Hatz, A.-K.; Moudrakovski, I.; Eger, R.; Kuhn, A.; Hoch, C.; Lotsch, B. V. Lesson Learned from NMR: Characterization and Ionic Conductivity of LGPS-like $Li_7SiPS_8$. *Chem. Mater.* **2019**, *31* (4), 1280–1288. DOI: 10.1021/acs.chemmater.8b04051.

(2) Kong, S. T.; Gün, O.; Koch, B.; Deiseroth, H. J.; Eckert, H.; Reiner, C. Structural characterisation of the Li argyrodites $Li_7PS_6$ and $Li_7PSe_6$ and their solid solutions: quantification of site preferences by MAS-NMR spectroscopy. *Chem. Eur. J* **2010**, *16* (17), 5138–5147. DOI: 10.1002/chem.200903023.

(3) Abrahams, S. C. The crystal and molecular structure of orthorhombic sulfur. *Acta Cryst.* **1955**, *8* (11), 661–671. DOI: 10.1107/S0365110X55002089.

(4) Zintl, E.; Harder, A.; Dauth, B. Gitterstruktur der Oxyde, Sulfide, Selenide und Telluride des Lithiums, Natriums und Kaliums. *Z. Elektrochem. angew. phys. Chem.* **1934**, *40* (8), 588–593. DOI: 10.1002/bbpc.19340400811.

(5) Shard, A. G. Detection limits in XPS for more than 6000 binary systems using Al and Mg Kα X-rays. *Surf. Interface Anal.* **2014**, *46* (3), 175–185. DOI: 10.1002/sia.5406.

### *7.1.3* Publication 3

# Supporting Information – Evolution of the Interphase between Argyrodite-based Solid Electrolytes and the Lithium Metal Anode – The Kinetics of Solid Electrolyte Interphase Growth

*Luise M. Riegger[1,2], Sophie Mittelsdorf[1,2], Till Fuchs[1,2], Raffael Rueß,[1,2] Felix H. Richter[1,2], Jürgen Janek[1,2*]*

[1] Institute of Physical Chemistry, Justus-Liebig-University Giessen, Heinrich-Buff-Ring 17, D-35392 Giessen, Germany.

[2] Center for Materials Research (ZfM), Justus-Liebig-University Giessen, Heinrich-Buff-Ring 16, D-35392 Giessen, Germany.

**This PDF File includes:**

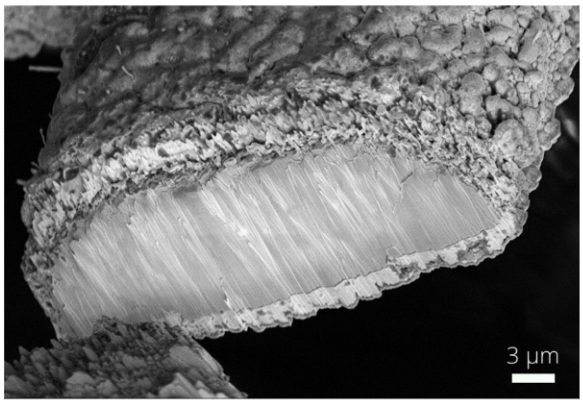


***Figure S1.*** Cross-section of the reference mesh showing a nickel core that is homogeneously covered with $InLi_x$ ($0 < x \leq 0.5$) on all sides. Due to the lower ion beam energy of the FIB-SEM preparation, artefacts can be avoided and the coating can be observed as prepared by vapor deposition. Opposed to the cross-section shown in this figure, the sample that was prepared by using the ion beam milling (see Figure 1b) has redeposition spots of nickel on the side facing away from the ion beam.

***Table S1.*** Change of the molar volume $V_{m,\,tot}$ for the reaction of $Li_6PS_5Cl$ with Li metal forming $Li_2S$, $Li_3P$ and LiCl. For each material the table lists the cell volumes $V_{cell}$ according to the respective cif file obtained by ICSD, the number of formula units $Z$ and the molar volume $V_m$, and $N_A$ as Avogadro´s constant.

| | Precursor | | → | Products | | |
|---|---|---|---|---|---|---|
| | $Li_6PS_5Cl$ | 8 Li | → | 5 $Li_2S$ | $Li_3P$ | LiCl |
| ICSD | 259205 | 44367 | | 196932 | 642223 | 52235 |
| $V_{cell}$ / Å$^3$ | 958.99 | 43.25 | | 187.35 | 120.08 | 136.27 |
| $Z$ | 4 | 2 | | 4 | 2 | 4 |
| $V_m = \frac{V_{cell} \cdot N_A}{Z}$ | | | | | | |
| $V_m$ / cm$^3$·mol$^{-1}$ | 144.38 | 13.02 | | 28.21 | 36.16 | 20.52 |
| $V_{m,\,tot}$ / cm$^3$·mol$^{-1}$ | 248.56 | | → | 197.70 | | |

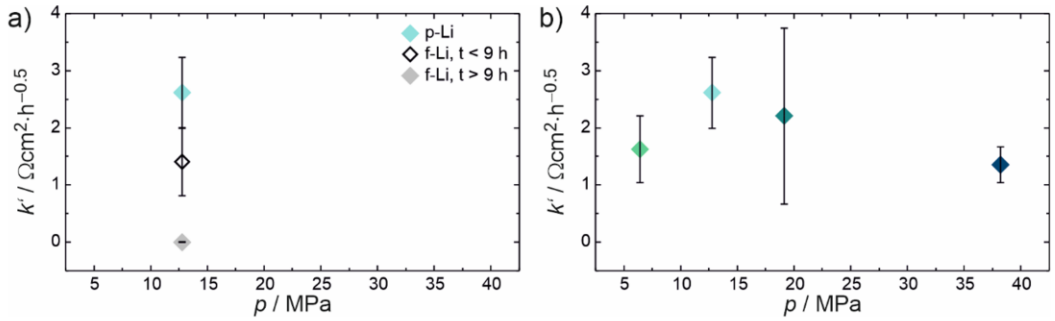


***Figure S2.*** a) Parabolic rate constants $k'$ of the SEI resistances seen in Figure 3a and plotted against the applied pressure for cells built with p-Li and f-Li applied at 12.7 MPa. For the cells built with f-Li, two parabolic rate constants are determined, one for the regime with a square root time dependency (shown with a black frame) and one for the stable interphase regime after 9 h of contact time (shown in grey). b) Parabolic rate constants $k'$ of the SEI resistances seen in Figure 3b and plotted against the applied pressure for cells built with p-Li but applied at different pressures. Since there were only a few minutes between cell construction and the start of the measurement, it is not necessary to take the time delay into account when fitting the data.

***Table S2.*** Initial values of the SEI resistance $R_0$(SEI) and the respective parabolic growth rates $k'$ of f-Li and p-Li cells at different pressures $p$.

| | $p$ / MPa | $R_0$(SEI) / Ωcm² | $k'$ / Ωcm²·h$^{-0.5}$ |
|---|---|---|---|
| f-Li | 12.7 | 3.23 | 0.88 ± 0.10 |
| | | 6.29 | 1.28 ± 0.06 |
| | | 10.39 | 2.06 ± 0.22 |
| p-Li | 6.4 | 45.33 | 1.09 ± 0.02 |
| | | 69.95 | 1.54 ± 0.01 |
| | | 81.61 | 2.25 ± 0.06 |
| | 12.7 | 34.17 | 1.93 ± 0.04 |
| | | 62.16 | 2.79 ± 0.02 |
| | | 74.88 | 3.14 ± 0.04 |
| | 19.1 | 22.85 | 0.98 ± 0.01 |
| | | 33.20 | 1.71 ± 0.01 |
| | | 70.09 | 3.94 ± 0.05 |
| | 38.2 | 15.46 | 1.14 ± 0.01 |
| | | 20.20 | 1.58 ± 0.03 |

## 7.2 Scientific Contributions

### *7.2.1* List of Publications

2023 B. Aktekin, **L. M. Riegger**, S.-K. Otto, T. Fuchs, A. Henss, J. Janek (**2023**). *SEI growth on Lithium metal anodes in solid-state batteries quantified with coulometric titration time analysis*. Nat. Commun. 14(6949).

Z. Zhang, K. A. Mazzio, **L. M. Riegger**, W. Brehm, J. Janek, J. Sann, P. Adelhelm (**2023**). *Copper Thiophosphate ($Cu_3PS_4$) as an Electrode Material for Lithium Solid-state Batteries with Lithium Thiophosphate ($\beta$-$Li_3PS_4$) Electrolyte*. Energy technol. 11(10).

K. Wissel, **L. M. Riegger**, C. Schneider, A. Waidha, T. Famprikis, Y. Ikeda, B. Grabowski, R. Dinnebier, B. V. Lotsch, J. Janek, W. Ensinger, O. Clemens (**2023**). *Dissolution and Recrystallization Behavior of $Li_3PS_4$ in Different Organic Solvents with a Focus on N-Methylformamide*. ACS Appl. Energy Mat. 6(15).

**L. M. Riegger**, S. Mittelsdorf, T. Fuchs, R. Rueß, F. H. Richter, J. Janek (**2023**) *Evolution of the Interphase between Argyrodite-based Solid Electrolytes and the Lithium Metal Anode – The Kinetics of Solid Electrolyte Interphases Growth*. Chemistry of Materials 35(13).

2022 Z. Wei, R. Maile, **L. M. Riegger**, M. Rohnke, K. Müller-Buschbaum, J. Janek (**2022**). *Ionic Liquid-Incorporated Metal-Organic Framework with High Magnesium Ion Conductivity for Quasi-Solid-State Magnesium Batteries*. Batteries & Supercaps 5(12).

**L. M. Riegger**, S.K. Otto, M. Sadowski, S. Jovanovic, O. Kötz, S. Harm, L. G. Balzat, S. Merz, S. Burkhardt, F. H. Richter, J. Sann, R.-A. Eichel, B. V. Lotsch, J. Granwehr, K. Albe, J. Janek (**2022**). *Instability of the $Li_7SiPS_8$ Solid Electrolyte at the Lithium Metal Anode and Interphase Formation*. Chem. Mater. 34(8).

S.K. Otto, **L. M. Riegger**, T. Fuchs, S. Kayser, P. Schweitzer, S. Burkhardt, A. Henss, J. Janek (**2022**). *In Situ Investigation of Lithium Metal-Solid Electrolyte Anode Interfaces with ToF-SIMS*. Adv. Mater. Interfaces 9(13).

J. S. Schulze, R. D. Brand, J. G. C. Hering, **L. M. Riegger**, P. R. Schreiner, B. M. Smarsly (**2022**). *DMAP Immobilized on Porous Silica Particles and Monoliths for the Esterification of Phenylethanol in Continuous Flow*. ChemCatChem 14(8).

2021 J. Ruhl, **L. M. Riegger**, M. Ghidiu, W.G. Zeier, (**2021**). *Impact of Solvent Treatment of the Superionic Argyrodite $Li_6PS_5Cl$ on Solid-State Battery Performance*. Adv. Energy Sustainability Res. 2(2).

**L. M. Riegger**, R. Schlem, J. Sann, W. G. Zeier, J. Janek, (**2021**). *Lithium-Metal Anode Instability of the Superionic Halide Solid Electrolytes and the Implications for Solid-State Batteries*. Angew. Chem. Int. Ed. 60(12).

2020 Y. Horowitz, C. Schmidt, D.H. Yoon, **L. M. Riegger**, L. Katzenmeier, G. M. Bosch, M. Noked, Y. Ein-Eli, J. Janek, W. G. Zeier, C. E. Diesendruck, D. Golodnitsky,

(**2020**). *Between Liquid and All Solid: A Prospect on Electrolyte Future in Lithium-Ion Batteries for Electric Vehicles*. Energy Technol. 8(11).

### *7.2.2* List of Conference Contributions

2022 Oral Presentation: **241st ECS Meeting**, Vancouver, Canada (05/2022): *Analysis of the Interphase Formation of Thiophosphate Solid Electrolytes and the Lithium Metal Anode in Solid-State Batteries.*

Online Oral Presentation: **Online Symposium "Lithium Metal Anodes and their Application in Batteries"** (02/2022): *Instability of $Li_7SiPS_8$ Solid Electrolyte at the Lithium Metal Anode and Interphase Formation.*

2021 Online Oral Presentation: **2021 MRS Fall Meeting**, online Conference (12/2021): *Analysis of the Interphase Formation between Metal Ion Containing Solid Electrolytes and the Lithium Metal Anode in Solid-State Batteries.*

Online Oral Presentation: **Solid-state Batteries 4.0 – from Fundamentals to Application**, online Conference (06/2021): *Lithium Metal Anode Instability of the Superionic Halide Solid Electrolyte and the Implications for Solid-State Batteries.*

2019 Oral Presentation: **German Israeli Battery School**, Berlin, Germany (05/2019): *Characterization of the Solid Electrolyte Interphase-Stability in Lithium Ion Batteries using X-ray Photoelectron Spectroscopy.*

## 8 Acknowledgements

First of all, I want to thank Prof. Jürgen Janek for giving me opportunity to pursue my PhD in his research group. I am grateful for his support and his insights, which have been very helpful to my work. In addition, his commitment to fostering excellent research conditions has provided me with an environment in which I could develop and grow.

I thank Joachim Sann for his mentoring, support, and ideas on XPS measurements. Our discussions, both on-topic and off-topic, have helped me in my professional and personal development.

I would like to express my appreciation to Felix H. Richter for his supervision and support. His feedback on my writing and presentations helped me a lot to improve.

Furthermore, I would like to thank Priv.-Doz. Dr. Matthias Elm for being the 2nd reviewer of this dissertation as well as Priv.-Doz. Dr. Angelika Polity and Prof. Bettina Lotsch for being part of the examination committee of my doctoral defense.

I am also grateful for the support and curiosity of Dr. Simon Burkhardt regarding my research. Our discussions have helped me to overcome challenges and grow both personally and professionally.

I thank my cooperation and project partners, particularly those from the "FestBatt – Cluster of Competence for Solid-state Batteries" project, for the fruitful exchange and our valuable discussions. Special thanks go to Dr. Justine Ruhl, Lucas Balzat, Dr. Marcel Sadowski, Dr. Sascha Harm, Prof. Bettina V. Lotsch and Prof. Wolfgang G. Zeier.

In addition, I want to thank my colleagues and friends in the Janek group. I greatly appreciate the support I have received from Dr. Svenja Otto, Dr. Burak Aktekin, Dr. Felix Walther, Jonas Hertle, Philip Minnmann, Dr. Till Fuchs, Christoph Alt and Juri Becker. Their scientific and personal support made my time as a PhD student memorable. I also thank my office colleagues Bastian Krauskopf, Kilian Vettori and Steffen Schröder for interesting and fun discussions during our coffee breaks.

I would also like to thank Nina Herrmann, Sophie Mittelsdorf, Fatima Pezic and Olaf Kötz for their assistance in the lab. Without their help, many of the necessary cell preparations would not have been possible.

Last but not least, I am deeply grateful to my family and friends for their continuous support, help and understanding throughout my PhD journey. Their unwavering encouragement has been invaluable to my success. Thank You!